

# Environmental Science Nano

Accepted Manuscript

This article can be cited before page numbers have been issued, to do this please use: I. Gregorovic, N. Lotfian, R. Khajavian, S. Maity, M. Mirzaei, S. S. Mal, M. Aureliano and A. Rompel, *Environ. Sci.: Nano*, 2026, DOI: 10.1039/D5EN00964B.



This is an Accepted Manuscript, which has been through the Royal Society of Chemistry peer review process and has been accepted for publication.

Accepted Manuscripts are published online shortly after acceptance, before technical editing, formatting and proof reading. Using this free service, authors can make their results available to the community, in citable form, before we publish the edited article. We will replace this Accepted Manuscript with the edited and formatted Advance Article as soon as it is available.

You can find more information about Accepted Manuscripts in the [Information for Authors](#).

Please note that technical editing may introduce minor changes to the text and/or graphics, which may alter content. The journal's standard [Terms & Conditions](#) and the [Ethical guidelines](#) still apply. In no event shall the Royal Society of Chemistry be held responsible for any errors or omissions in this Accepted Manuscript or any consequences arising from the use of any information it contains.

1  
2  
3 This comprehensive review covers remediation, sensing, and energy storage, inspiring sustainable  
4 polyoxometalate innovations.  
5

6 Polyoxometalates (POMs) are metal-oxide complexes with exceptional redox tunability,  
7 pseudocapacitive charge storage, and great structural versatility, making them ideal nanomaterials  
8 for environmental remediation. This review analyses the POM-based technologies for detection  
9 and treatment of air/water pollutants, surpassing conventional technologies that require harsh  
10 conditions for hard-to-remove contaminants such as refractory sulfur compounds.  
11

12 Global pollution includes refractory sulfur compounds from fossil fuels, toxic gases in air, and  
13 heavy metals, dyes, and emerging contaminants in water, driving acid rain, smog, antibiotic  
14 resistance and ecosystem toxicity. POMs provide efficient oxidative desulfurization,  
15 photocatalytic dye/heavy metal removal, and multipollutant adsorption in POM-based hybrid  
16 materials. POM structures enable visible-light mineralization in low-input environments with less  
17 energy; benefits include scalable low-toxicity remediation, while metal leaching risks under  
18 extreme pH are mitigated by heterogenization.  
19  
20  
21  
22  
23  
24  
25  
26  
27  
28  
29  
30  
31  
32  
33  
34  
35  
36  
37  
38  
39  
40  
41  
42  
43  
44  
45  
46  
47  
48  
49  
50  
51  
52  
53  
54  
55  
56  
57  
58  
59  
60

## ARTICLE

# Polyoxometalates in Environmental Remediation and Energy Storage

Ingrid Gregorovic<sup>a,b</sup>, Nahid Lotfian<sup>c</sup>, Ruhollah Khajavian<sup>c</sup>, Sukanya Maity<sup>d,e</sup>, Masoud Mirzaei<sup>c\*</sup>, Sib Sankar Mal<sup>e\*</sup>, Manuel Aureliano<sup>f,g\*</sup> and Annette Rompel<sup>a,b\*</sup>Received 00th January 20xx,  
Accepted 00th January 20xx

DOI: 10.1039/x0xx00000x

Over recent decades, while environmental awareness and pollution control efforts have yielded localized improvements, ongoing industrial growth, rapid global population expansion, and escalating energy demands continue to drive significant global environmental pollution challenges. Polyoxometalates, a remarkable class of metal-oxide complexes, have recently emerged as promising compounds in the development of multifunctional materials for environmental pollutant removal, energy conversion and storage, and sensing. This review critically examines current research on their use for the removal of common toxic gases – such as H<sub>2</sub>S, NO<sub>x</sub>, and volatile organic compounds (VOCs) – from polluted air, as well as the elimination of various organic dyes, heavy metals, and pharmaceutical contaminants from wastewater. POMs have also gained recognition as adaptable redox-active materials suitable for next-generation energy storage systems. Their high electron-transfer capacity, structural flexibility, and remarkable chemical stability make them ideal candidates for various applications. POMs can facilitate multi-electron redox processes, allowing for their application in batteries, supercapacitors, and hybrid devices, which results in improved energy density and cycling performance. Recent developments in POM-based composites and electrode designs are further discussed for innovative, sustainable, and scalable energy storage solutions. Additionally, their tunable electrical and magnetic properties make them effective sensors for detecting various environmental pollutants.

## 1 Introduction

In recent times, rapid industrial and technological development has caused a significant increase in energy demand and environmental pollution (EP).<sup>1,2-3</sup> The Encyclopaedia Britannica defines environmental pollution as the addition of any substance (solid, liquid, or gas) or any form of energy (such as heat, sound, or radioactivity) to the environment at a rate faster than it can be removed from the environment or stored in a harmless form. It further categorizes environmental pollution based on the affected medium into air, water, and land pollution.<sup>4</sup> Increasing attention has been paid to the development of new methods for the removal of potential environmental pollutants<sup>1-3</sup> during industrial processes and

clean energy production.<sup>5</sup> Although industrial development has brought many positive aspects to everyday life (e.g. new technology, better food safety and supply, medicines, etc.), it has also increased consumption and pollution of natural resources (water, soil and air)<sup>3,6</sup>, which has become both an environmental problem and a health threat for the entire human population.<sup>7</sup>

The global shortage of clean water and the pollution of water resources pose critical health, economic<sup>8</sup>, and environmental challenges.<sup>9-11</sup> Especially in many underdeveloped and currently developing parts of the world, sewage wastewater and wastewater from different factories are discharged directly into the environment, causing catastrophic water pollution (Section 2; **Figure 1**) with hard-to-remove toxic chemicals – inorganic pollutants (Section 2.2) such as heavy metals (Section 2.2.1) and organic pollutants<sup>12</sup> (Section 2.3) such as organic dyes<sup>13</sup> and solvents.<sup>14</sup>

The most prominent classes of health emerging pollutants (EPs)<sup>15-17</sup> (Section 3; **Figure 1**) are pharmaceuticals<sup>18</sup> (Section 3.1), pesticides and herbicides<sup>19</sup> (Section 3.2), cosmetics<sup>20,21</sup>, industrial and household products<sup>22</sup>, metals<sup>13</sup> (Section 2.2), dyes<sup>13</sup> and aromatic hydrocarbons (Section 2.3.2).<sup>23</sup> The presence of EPs in wastewater has been associated with the development of bacterial resistance<sup>20,24</sup>, and mutagenicity and toxicity in aquatic organisms<sup>21,25</sup> and humans.<sup>22,25</sup>

Pesticides and herbicides (for their removal, see Section 3.2) are an inevitable part of the modern agricultural industry and food production.<sup>26</sup> However, in addition to ensuring yields and

<sup>a</sup> Universität Wien, Fakultät für Chemie, Institut für Biophysikalische Chemie, Josef-Holaubek-Platz 2, 1090 Wien, Austria. E-mail: annette.rompel@univie.ac.at

<sup>b</sup> Vienna Doctoral School in Chemistry (DoSChem), Universität Wien, Währinger Straße 42, 1090 Vienna (Austria)

<sup>c</sup> Department of Chemistry, Faculty of Science, Ferdowsi University of Mashhad, Mashhad 9177948974, Iran. E-mail: mirzaesh@um.ac.ir

<sup>d</sup> Department of Physics, Chemistry and Biology (IFM), Linköping University, 58183 Linköping, Sweden

<sup>e</sup> Department of Chemistry, National Institute of Technology Karnataka, Surathkal, Mangalore-575025, India. E-mail: malss@nitk.edu.in

<sup>f</sup> Faculdade de Ciências e Tecnologia (FCT), Campus de Gambelas, Universidade do Algarve, 8005-139 Faro, Portugal

<sup>g</sup> Centro de Ciências do Mar do Algarve (CCMAR/CIMAR LA), Campus de Gambelas, Universidade do Algarve, 8005-139 Faro, Portugal. E-mail: maalves@ualg.pt

Supplementary Information available: [details of any supplementary information available should be included here]. See DOI: 10.1039/x0xx00000x

protecting crops from pests, the widespread use of these chemicals also affects soil enzymes and microorganisms<sup>26</sup> crucial for many essential biological processes, such as N<sub>2</sub>-fixation in plants by rhizobacteria.<sup>27</sup> The excessive use of pesticides also impacts wildlife, with a scientific focus on bees, birds, fish and small mammals.<sup>28-30</sup> Human health is also affected by pesticide residues in the environment and food<sup>31</sup> causing various health problems, such as cancer,<sup>32,33</sup> endocrine disruption,<sup>34</sup> obesity,<sup>35,36</sup> reproductive health issues, and birth defects.<sup>37</sup> Therefore, many Western countries (e.g. EU, USA) have introduced stricter controls and limitations<sup>38</sup> on the use and allowable levels of pesticide residues in food, water and soil.<sup>31</sup>

Fossil fuels continue to be one of the primary energy sources in today's world.<sup>39</sup> Their combustion (Section 4.1) produces various toxic refractory sulfur-containing compounds (dibenzothiophenes, DBTs)<sup>40,41</sup> and gases (hydrogen sulfide<sup>42</sup> (Section 4.2.1), nitrogen oxides (Section 4.2.2), and sulfur oxides (Section 4.2.2)<sup>43</sup>, which cause different severe environmental issues such as global warming,<sup>40</sup> smog<sup>44</sup> and acid rains.<sup>45</sup> Toxic gases generated from traffic and flue gases from the industry have made poor air quality an important factor in causing respiratory<sup>46-48</sup> and cardiovascular health<sup>49</sup> issues in urban areas.<sup>50</sup> Air purification (Section 4; **Figure 1**) using adsorption processes<sup>51</sup> (Section 4.2) and desulfurization of fossil fuels<sup>52</sup> (Section 4.1) is currently a logical approach to decreasing air pollution.

Global environmental pollution has escalated to crisis levels, driven significantly by fossil fuel combustion that releases refractory sulfur compounds such as dibenzothiophenes (DBTs), toxic gases including H<sub>2</sub>S, NO<sub>x</sub>, and SO<sub>2</sub>, and emerging contaminants resistant to conventional treatment methods. These pollutants contribute directly to the formation of acid rain, smog, and severe health crises that impact billions worldwide.<sup>52,53-59</sup> Conventional technologies like hydrodesulfurization (HDS) are ineffective against sterically hindered DBTs and require extreme conditions (300-400 °C, 30-100 bar H<sub>2</sub>), while amine scrubbing and selective catalytic reduction (SCR) systems<sup>60</sup> face limitations in capacity, cost-efficiency, and simultaneous multi-pollutant management for air purification.<sup>53,61</sup> Water faces persistent heavy metals, dyes, pharmaceuticals, and microplastics that evade standard filtration and oxidation.<sup>15,16,17,20,22,24,25</sup> POMs offer a powerful, direct solution to these multifaceted challenges via mild-condition oxidative desulfurization achieving over 99% removal of refractory sulfur, versatile multi-pollutant adsorption and catalysis, and photocatalytic mineralization.<sup>62,63</sup> Their uniquely tunable redox properties and acidity provide sustainable remediation options precisely where traditional technologies are insufficient.<sup>53,62</sup>

The first step in combating pollution is building a good system to monitor and detect various harmful compounds present in the environment. In this regard, various materials have been extensively researched and designed to develop new chemical<sup>64</sup>, electrochemical<sup>65</sup>, and biosensors<sup>66</sup> (Section 5; **Figure 1**) for environmental monitoring. For example, metal or

metal oxide nanoparticles are widely used to develop various electrochemical sensors.<sup>67-69</sup>

DOI: 10.1039/D5EN00964B

New efficient technologies for energy conversion and storage need to be developed (Section 6; **Figure 1**) because renewable energy sources such as wind, hydroelectric, and solar power alone cannot meet the world's current energy demands.<sup>70</sup> In addition, the growing popularity and use of various portable electronic devices in everyday life have led to intensive research and development of new efficient battery technologies such as lithium-ion<sup>71</sup>, sodium-ion<sup>72</sup>, and redox-flow batteries.<sup>73</sup> Rechargeable Li-ion batteries and supercapacitors have been commercially utilized due to their ability to hold high energy with power density for various applications (e.g., electric vehicles, power tools, or portable/wearable electronic devices).<sup>74-76</sup>

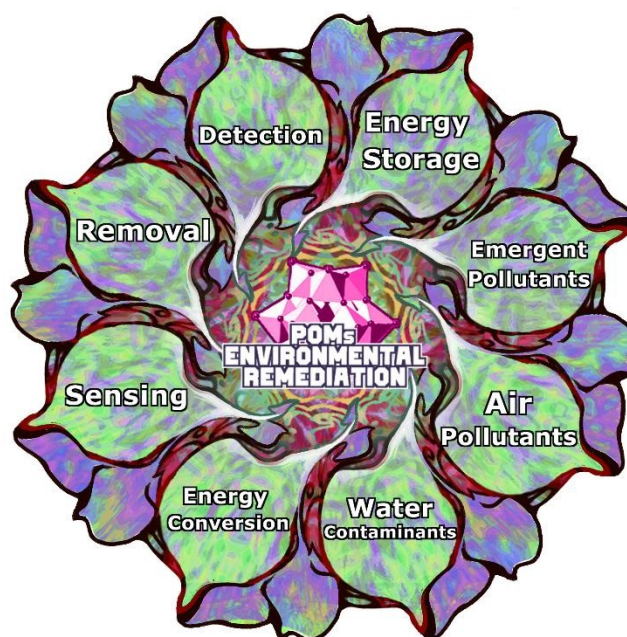


**Figure 1.** Schematic illustration of the main roles of polyoxometalates (POMs) in environmental remediation and energy storage. The central part emphasizes POM-based environmental remediation, while the surrounding segments show key applications, including pollutants detection, removal, sensing, treatment of (health) emerging pollutants, air pollutants and water contaminants, energy storage, energy conversion, and signalling.

### 1.1 Polyoxometalates

Polyoxometalates (POMs)<sup>77</sup> are a class of transition metal-oxide clusters, usually containing Mo or W ions in their highest oxidation states. They exhibit exciting and unique physical and chemical properties, such as controllable shape and size<sup>77</sup>, oxygen-enriched surfaces, photoactivity<sup>78</sup>, molecular conductivity<sup>79</sup>, excellent chemical stability, and redox properties<sup>80</sup>. These properties have led to their increasing use in diverse fields, including catalysis<sup>81,82</sup>, magnetism<sup>83</sup>, medicine<sup>84,85</sup>, biotechnology<sup>86</sup>, protein crystallography<sup>87-89</sup>, and material science<sup>90</sup>.

POMs are typically synthesized via controlled acidification and condensation of simple metal oxoanions such as Mo<sup>VI</sup>O<sub>4</sub><sup>2-</sup>, W<sup>VI</sup>O<sub>4</sub><sup>2-</sup>, or V<sup>VO</sup>O<sub>4</sub><sup>3-</sup>, which allows the precise formation of diverse structural archetypes, including some of the most common POM archetypes like Keggin (**Figure 1.F**), Wells-Dawson (**Figure 1.H**), and Anderson-Evans (**Figure**



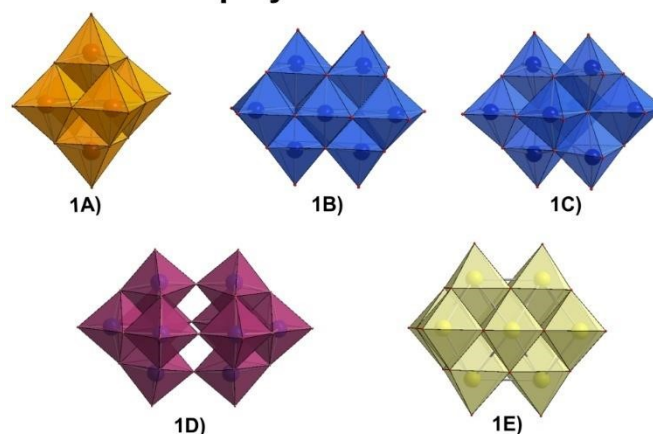
1.1.)<sup>76,77,91,92,93</sup> Their functionality in pollutant removal is often enhanced by immobilization or hybridization<sup>94</sup>, where POMs are incorporated into different solid supports like metal-organic frameworks (MOFs)<sup>95–105</sup>, porous silica<sup>106,107</sup>, graphene oxide (GO)<sup>108,109</sup>, or polymeric supports<sup>94,110,111</sup>, improving POM stability and catalytic efficiency.<sup>94,101,112</sup> Ion exchange with organic or inorganic cations<sup>113,114,115</sup>, surface modifications<sup>94</sup>, or doping with lanthanide ions<sup>116</sup> further tailor their physicochemical properties. Such synthetic versatility enables customization of POM-based materials to optimize catalytic, adsorptive, and photocatalytic performance in environmental remediation.<sup>94,101,117</sup> The structural characteristics of polyoxometalates can be divided into two main general subgroups, isopolyoxometalates and heteropolyoxometalates.<sup>76,77</sup> The isopolyoxometalates, with the general formula  $[M_xO_y]^{n-}$  (where M = Mo, W or V; **Figure 2.A–D**), contain only addenda metals and oxygen atoms in their structure, such as Lindqvist<sup>118,119</sup> ( $[M_6O_{19}]^{2-}$ ; **Figure 2.A**), heptamolybdate<sup>120,121</sup> ( $[Mo^VI_7O_{24}]^{6-}$ ; **Figure 2.B**), octamolybdate<sup>122,123</sup> ( $[Mo^VI_8O_{26}]^{4-}$ ; **Figure 2.C**), decatungstate<sup>124,125</sup> ( $[W^VI_{10}O_{32}]^{4-}$ ; **Figure 2.D**) and decavanadate<sup>126,127</sup> ( $[V^VI_{10}O_{28}]^{6-}$ ; **Figure 2.E**). Heteropolyoxo species have the general formula  $[X_zM_xO_y]^{n-}$  (X = heteroion, M = Mo, W or V,  $z < x$ , y = number of oxygen atoms in the POM structure, n = overall anion charge), where different heteroions X are present alongside addenda ions M and oxygen atoms. This composition allows them to form a variety of structural types, including common ones such as Keggin<sup>128,129</sup> ( $[XM_{12}O_{40}]^{n-}$ ; **Figure 2.F**), lacunary Keggin<sup>130</sup> ( $[XM_{11}O_{39}]^{n-}$ ; **Figure 2.G**), Wells-Dawson<sup>131,132</sup> ( $[X_2M_{18}O_{62}]^{n-}$ ; **Figure 2.H**), Anderson-Evans<sup>133,134</sup> ( $[XM_6O_{24}]^{n-}$ ; **Figure 2.I**), Preyssler<sup>135</sup> ( $[MP_5M_{30}O_{110}]^{(15-n)-}$ ; **Figure 2.J**), Strandberg<sup>136,137</sup> ( $[X_2Mo^VI_5O_{23}]^{n-}$ , (X = P<sup>V</sup>, S<sup>VI</sup>, As<sup>V</sup>, Se<sup>VI</sup>); **Figure 2.K**), Weakley<sup>138,139</sup> ( $[M^{III}(M^VI_5O_{18})_2]^{n-}$ ; **Figure 2.L**), among others. Moreover, if the POM solution is reduced, a unique class of giant molybdenum blue and molybdenum brown-type structures ( $\{Mo_{154}\}$  and  $\{Mo_{132}\}$ ) are formed.<sup>140</sup> For more detailed information on POMs structures and general synthetic procedures, the reader is referred to the reviews in reference 91, 92, 93, 141, and 142.

Pure POMs exhibit different solution behaviors across the wide pH range; some, like Wells-Dawson-type structures, maintain their structural integrity, while others, such as Keggin-type POMs, undergo monolacunarization under acidic conditions relevant to environmental remediation.<sup>143–145</sup> Their high solubility in aqueous media presents significant challenges for their use in applications, including leaching during wastewater treatment and difficulties in catalyst recovery.<sup>113</sup> While pure POMs often dissolve in aqueous media<sup>113</sup>, strategic heterogenization approaches<sup>94</sup>, such as immobilization on mesoporous silica (SBA-15)<sup>106,107,146</sup>, metal-organic frameworks (like UiO-66 and MIL-101)<sup>95–101</sup>, and POM-supported ionic liquid phases (POM-SILPs)<sup>147,112</sup>, address this issue. Such methods significantly reduce leaching to < 1 % after 10 cycles (Tables S1 and S2). These enable recyclability over 5–10 cycles with minimal activity loss (**Table S1**)<sup>148–151</sup>. Nevertheless, challenges remain including potential metal cation leaching from POM-composites under prolonged extreme pH exposure and the

need for long-term stability studies under real environmental conditions. These heterogenized systems demonstrate > 95 % POM retention after multiple uses.<sup>63</sup>

Keggin-type POMs (**Figure 2.F–G**) are the most widely studied POM archetype, representing an average of 77.6 % of all published articles, particularly in applications targeting environmental pollutant removal (approximately 69 %). This predominance in environmental applications surpasses that of Wells-Dawson (**Figure 2.H**; ~9 %), Anderson-Evans (**Figure 2.I**; ~9 %), Sandwich-type (**Figure 2.L**; ~5 %), isopolymolybdates (**Figure 2.A–E**; ~5 %), and other types of POMs (each ~5 %). In this review, Keggin-type POMs (**Figure 2.F–G**) are most frequently addressed in Section 3 (wastewater treatment, 75 %) and Section 4 (air pollutant removal, 85 %). Wells-Dawson type POMs (**Figure 2.H**) rank second in environmental pollutant removal (average 16.9 %), with their primary use found in sensing (75 %, Section 5). Notably, Section 4.1. showcases the broadest diversity of structural archetypes for POM-mediated fossil fuel desulfurization.

### Isopolyoxometalates



### Heteropolyoxometalates

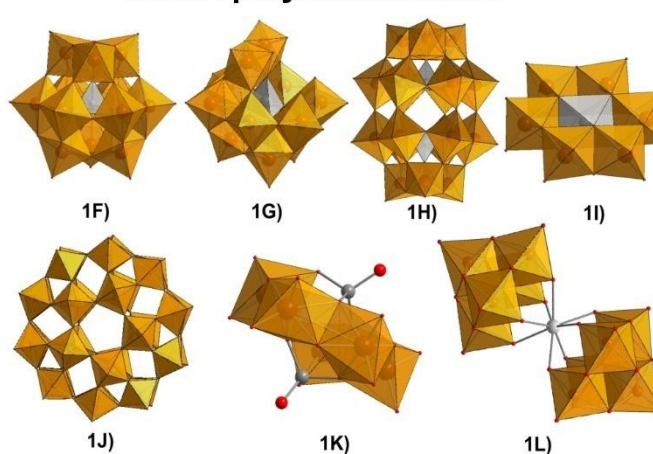


**Figure 2.** Structures of isopolyoxometalates and heteropolyoxometalates: 1A) Lindqvist ( $[M_6O_{19}]^{2-}$ ), 1B) heptamolybdate ( $[Mo^VI_7O_{24}]^{6-}$ ), 1C) octamolybdate ( $[Mo^VI_8O_{26}]^{4-}$ ), 1D) decatungstate ( $[W^VI_{10}O_{32}]^{4-}$ ), 1E) decavanadate ( $[V^VI_{10}O_{28}]^{6-}$ ), 1F) Keggin ( $[XM_{12}O_{40}]^{n-}$ ), 1G) lacunary Keggin ( $[XM_{11}O_{39}]^{n-}$ ), 1H) Wells-Dawson ( $[X_2M_{18}O_{62}]^{n-}$ ), 1I) Anderson-Evans ( $[XM_6O_{24}]^{n-}$ ), 1J) Preyssler ( $[MP_5M_{30}O_{110}]^{(15-n)-}$ ), 1K) Strandberg ( $[X_2Mo^VI_5O_{23}]^{n-}$ ), and 1L) Weakley ( $[M^{III}(M^VI_5O_{18})_2]^{n-}$ ). Color legend: orange = M (either  $Mo^VI$ ,  $W^VI$  or  $V^VI$ ), blue =  $Mo^VI$ , purple =  $W^VI$ , yellow =  $V^VI$ , gray = X (heteroion), white =  $M^{III}$ , and red = oxygen.

A literature search conducted on Web of Science in August 2025 (**Figure 3**) revealed that approximately 12 % (1928) of the



published articles on POMs related to the keyword “environment”, out of a total of 15830 articles. As of August 14, 2025, the number of articles varies by specific subject: the combination of “polyoxometalate” and “degradation” yielded 1306 articles, while “polyoxometalates” and “dyes” yielded 910 articles. These numbers exceed those for “polyoxometalate” combined with “pollutants” (353), “waste” (258), “industrial chemicals” (134), and “wastewater” (215). Fewer articles were found for combinations with “antibiotics” (98), “pesticides” (48), “fossil fuels” (40), and “air pollution” (26). The number of publications related to “antibiotics” and “wastewater” has more than doubled over the past 2 years, reflecting a marked increase in research interest in these areas.

In fact, the importance of POMs in environmental science and their relationship to sustainable development and green chemistry is clearly increasing. POMs are crucial in environmental science for their roles as catalysts and adsorbents, aiding in the degradation of emerging pollutants such as dyes, plastics, and antibiotics, in addition to well-known organic and inorganic contaminants<sup>152–160</sup>. Moreover, POMs can act as novel antibacterial agents for water purification<sup>161</sup>. As described in the sections below, POMs are also fundamental for sustainable development by enabling energy applications such as solar hydrogen production and energy storage<sup>70–76</sup>. Recent studies further explore POMs as electrochemical sensors for the simultaneous detection of inorganic heavy metal ions and organic antibiotic contaminants in aquatic environments<sup>162</sup>, and as triboelectric nanomaterials for gait monitoring<sup>163</sup>.

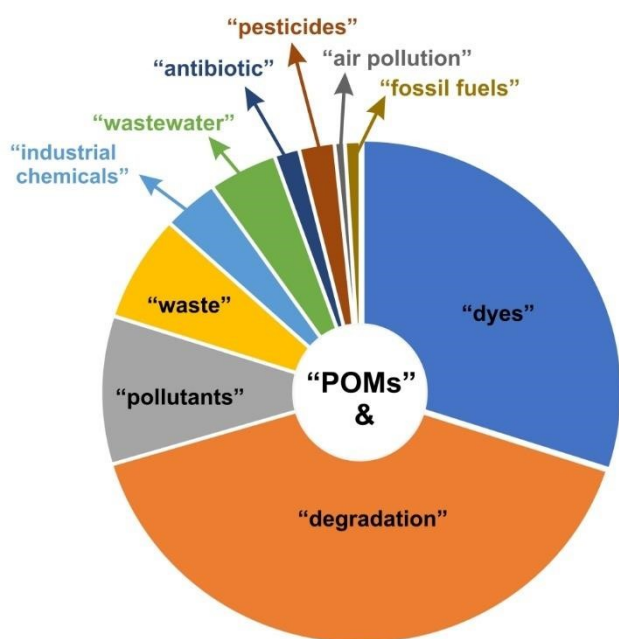


**Figure 3.** Number of articles containing the term “polyoxometalate” combined with keywords such as dyes, pollutants, industrial chemicals, wastewater, pesticides, and antibiotics, as of August 14, 2025.

## 2 Water decontamination by polyoxometalates

Inorganic contaminants (Section 2.2) enter the environment as inorganic salts, mineral acids, sulfates, cyanides, and metal ions,

including heavy and radioactive metals. These contaminants are generally more persistent and more difficult to eliminate than organic ones.<sup>164,165</sup> On the other hand, organic contaminants (Section 2.3) represent a more diverse class, consisting of organic dyes, aromatic hydrocarbons, pesticides, and pharmaceuticals (see Section 3 for pharmaceutical and pesticide removal). Due to rapid industrial development, large amounts of industrial, sewage, and agricultural waste discharged into water bodies cause organic pollutants to become pseudo-persistent in the ecosystem.<sup>166,167</sup> Therefore, the removal of this class of contaminants requires careful consideration to move toward a sustainable ecosystem.

As discussed in Section 2.1, oxidation, catalysis, photocatalysis, ion-exchange, adsorption, and membranes are among the commonly used technologies for the removal of these pollutants due to their high efficiency, cleanliness, and simple operation. POMs have shown promise in mitigating the global water purification issue using the above-mentioned technologies. This section covers novel solutions by highlighting recent achievements in designing multi-component materials for use in water-purification systems.

### 2.1 Emerging pollution treatment technologies

Water treatment is a multi-stage process, comprising several stages with various technologies. Tertiary treatment is the final stage of the multi-stage wastewater treatment process. It is used after preliminary stages, and commonly used techniques utilized for the treatment include oxidation, photocatalysis, ion exchange, adsorption, and membranes technology (Figure 4).<sup>168</sup> Chemical oxidation is a cost-effective and simple technology for the decontamination of both organic and inorganic pollutants using an oxidizing agent such as chlorine, hydrogen peroxide, ozone, and molecular oxygen. In advanced oxidation processes (AOPs), POMs (especially iron-containing POMs) have been used as efficient catalysts for the decomposition of the oxidizing agent ( $H_2O_2$ ) and removal of organic pollutants.<sup>169</sup> In particular, POMs can initiate the activation through electron transfer to  $H_2O_2$  (originating from the redox property of the addenda atoms) or *via* formation of peroxy complexes.<sup>147,170</sup> This method, however, may produce secondary pollutants that are formed after the initial oxidation. This may cause a decrease in the catalyst selectivity, while increasing the costs.

In photocatalysis, the ability of the catalyst to harvest photons from a light source and to generate free radicals to undergo photocatalytic oxidation or reduction reactions is crucial. In this regard, POMs have shown promise since i) their band gap value can be adjusted by changing the heteroatoms or adjusting the valence states of addenda atoms, and ii) they can store multiple electrons in one molecule; thus they exhibit fast charge transfer properties.<sup>171,172</sup> Due to some drawbacks associated with pure POMs (*e.g.*, limited light absorption, high solubility), they are often employed in the form of hybrids or composites.<sup>112</sup> In these structures, the intermolecular interactions between two species can improve the stability and promote the lifetime of photogenerated charge carriers. In this regard, the incorporation of noble



metals,<sup>173,174</sup> metals from the lanthanide series,<sup>175</sup> metal oxides,<sup>176</sup> metal-organic frameworks<sup>177</sup> and metal-free species<sup>110</sup> have been reported to be effective.

View Article Online  
DOI: 10.1039/D5EN00964B

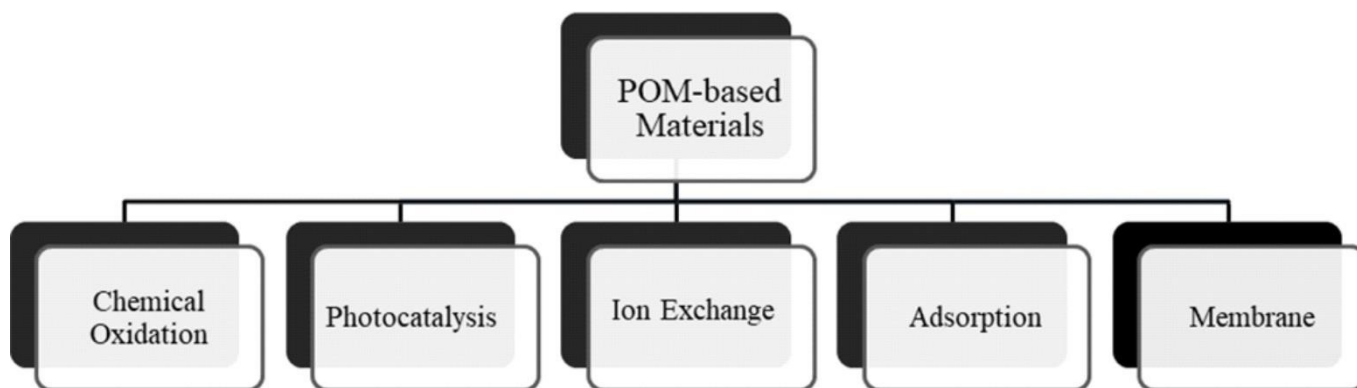


Figure 4. Summary of tertiary treatment technologies used against inorganic and organic pollutants for water purification.

Ion exchange water purification technology relies on the availability of exchange surfaces with accessible specific surface area and the ability to reversibly uptake/release ions from water. POMs can fulfill some of these requirements. For example, their diverse topology, high negative charge, and redox properties of POMs have turned them into potential candidates for cation (heavy metal) uptake and exchange. However, POMs lack a high surface area that is problematic.<sup>113</sup> Adsorption-based protocols have been extensively used for wastewater treatment on the account of cost, simplicity, and energy considerations. The concept of this approach is based on removing pollutants by promoting their adsorption on the adsorbent surface *via* physical or chemical interactions.<sup>178</sup> In this context, some intrinsic properties of POMs (*e.g.*, high negative charge, strongly basic oxygen surfaces) are advantageous for the physio/chemisorption of adsorbate molecules. However, when considering POMs as water purifiers, some limitations such as their high solubility and the low surface area must be taken into consideration. The heterogenization of POMs by inorganic substrates<sup>106,107,179</sup> or organic matrices<sup>111,179,180</sup> is the common approach to solve their solubility issue and low specific surface area. In heterogenization with organic matrices, the surface chemistry of the matrix plays an important role. Along with the degree of POM dispersion and matrix morphology, it can enhance the physicochemical properties and improve the membrane's performance. Heterogenization by porous coordination polymers (MOFs) is another successful strategy that combines both the merits of POMs and MOFs (*e.g.* recyclability and porosity).<sup>95–101</sup> This strategy is commonly used for the adsorptive removal of cationic dyes.<sup>102–105</sup> However, the catalytic activity of POM composites greatly depends on their structural properties. In some cases, as for POM@MOF composites, the activity is mainly governed by pore-dependent diffusion limitation, where the match of pore aperture and POM diameter is essential.<sup>139</sup> Meanwhile, each individual structural component can also induce different electron transfer kinetics due to its unique electron-storage/transfer capacity.<sup>181,182</sup>

Controlled deposition of POMs on substrates is another concept that enables the fabrication of POM-based functional devices for water purification.<sup>94</sup> Techniques such as layer-by-layer assembly, casting, and dip-coating have been recently reported.<sup>183–185</sup>

Membrane filtration is a reliable, and environmentally friendly process with relatively low cost and simple operation, which has been widely used for water purification. Catalytic membranes represent a new generation of membranes created by incorporating inorganic particles, such as POMs, into a polymer matrix to enhance the membrane's (photo)catalytic properties.<sup>186–189</sup> As a convincing demonstration of this approach, Yao *et al.* designed and fabricated an amine-functionalized APTMS-treated PEI membrane for dye removal from wastewater.  $[PV_2MoV_{12}O_{40}]^{5-}$  was incorporated into the matrix *via* a simple sol-gel protocol. The presence of  $[PV_2MoV_{12}O_{40}]^{5-}$  in the membrane not only enhanced the mechanical strength of PEI but also catalyzed the degradation of RB5 in the presence of a diluted solution of an oxidant (Figure 5).<sup>190</sup> The presence of different POM species was reported to be necessary for the self-cleaning property of the membrane.<sup>183</sup>

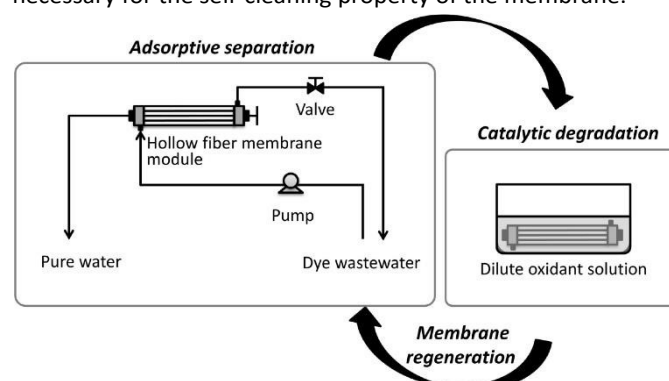


Figure 5. Illustration of a POM-integrated catalytic membrane for organic dye decontamination from water. Reproduced from Ref. 190 with permission from Elsevier, Copyright 2016.

## 2.2 Removal of inorganic pollutants

**2.2.1 Removal of heavy metals.** Catalysis and photocatalysis are appropriate strategies for removing reductive toxic metal ions

from water.<sup>108,191,192</sup> Gong *et al.* demonstrated that different highly reduced molybdophosphate hybrid materials such as  $\{Co^{II}[P^V_4Mo^V_6X_{31}2]^{n-}$  ( $X = O$  or  $OH$ )<sup>193</sup> or  $\{Mn^{II}[P^V_4Mo^V_6O_{31}2]^{194}$  clusters could act as efficient heterogeneous catalysts for the reduction of toxic Cr(VI) to nontoxic Cr(III) in the presence of formic acid as the reducing agent under mild conditions. These noble metal-free POM catalysts have great potential to replace high-priced Pt/Pd catalysts for the elimination of Cr(VI) from water.

POMs or their modified derivatives, acting as electron reservoirs, have demonstrated efficiency in photoactivity, especially in visible light photocatalysis. Therefore, there is continuous effort to design a POM-based photocatalyst that can utilize solar energy for the reduction of highly toxic Cr(VI). Due to the good photocatalytic response of Ag-based photocatalysts, Wang's group heterogenized  $H_3[PMo^{VI}_{12}O_{40}]$  with  $Ag^+$  counter cations.<sup>195</sup>  $Ag/Ag_xH_{3-x}PMo^{VI}_{12}O_{40}$  nanowires were synthesized by a facile solid-state reaction route and in situ photodeposited method. The resulting  $Ag/Ag_x[H_{3-x}PMo^{VI}_{12}O_{40}]$  ( $Ag/AgHPMo_{12}$ ) nanowires, where  $x$  denotes the irradiation time ( $x = 2, 4, 6, 8$  h, respectively), showed higher stability and photocatalytic activity than traditional Ag-based photocatalysts (*e.g.*  $Ag/AgX$  ( $X = Cl, Br, I$ ),  $AgPO_4$  or  $AgVO_3$ )<sup>196–199</sup> for Cr(VI) reduction. This is attributed to their good visible-light absorption and reversible redox properties of the Keggin-type POM (**Figure 2.F**). In addition, a part of the  $Ag^+$  in the nanowires was *in situ* photoreduced to Ag NPs under visible light irradiation, and these Ag NPs enhanced visible-light absorption and the charge separation of photogenerated electrons ( $e^-$ ) and holes ( $h^+$ ) in  $Ag/[AgHPMo^{VI}_{12}]$ . In order to improve the catalytic efficiency of  $Ag/[Ag_xH_{3-x}PMo^{VI}_{12}O_{40}]$  nanowires, these Ag-loaded 1D silver POM nanowires were well dispersed on duplicated 2D graphite-like carbon nitride ( $g-C_3N_4$ ) nanosheets.<sup>200</sup> The obtained  $[Ag_xH_{3-x}PMo^{VI}_{12}O_{40}]/Ag/g-C_3N_4$  ( $x$  represents the irradiation time;  $x = 2, 4, \text{ and } 6$  h, respectively) 1D/2D Z-scheme heterojunction photocatalyst exhibited excellent and durable photocatalytic performance towards the reduction of Cr(VI), methyl orange (MO) and tetracycline (TCY) under visible light.<sup>200</sup>

In attempts to obtain efficient photocatalysts based on inorganic-organic hybrid POMs, a series of  $[Ag_4(H_2O)(L)_3(SiW^{VI}_{12}O_{40})]$ ,  $[Zn(L)(H_2O)_2[SiW^{VI}_{12}O_{40}]\cdot 3H_2O$ ,  $[Cu(L)(H_2O)_2[SiW^{VI}_{12}O_{40}]$ , and  $[Cu_2(L)_2(HPW^{VI}_{10}W^V_2O_{40})\cdot 4H_2O$  ( $L = 1,4\text{-bis}(3\text{-}(2\text{-pyridyl})\text{pyrazole})\text{butane}$ ), have been synthesized.<sup>201</sup> Interestingly,  $[Ag_4(H_2O)(L)_3(SiW^{VI}_{12}O_{40})]$  (1) hybrid was able to act as an efficient photocatalyst to reduce Cr(VI) using the scavenger isopropanol under visible light at ambient temperature. In comparison with  $[Ag_4(H_2O)(L)_3(SiW^{VI}_{12}O_{40})]$ , the three other POM hybrids showed relatively weak photocatalytic activity. In a possible reduction mechanism of Cr(VI) to Cr(III), first, the  $[Ag_4(H_2O)(L)_3]^{4+}$  unit was excited under visible light, and the excited state electrons on the organic ligand were inclined to transfer to the  $[Ag_4(H_2O)(L)_3(SiW^{VI}_{12}O_{40})]$  POM. Simultaneously, the isopropanol on the surface of the hybrid yielded reducing radicals and captured the photoinduced holes produced by the hybrid photocatalyst. Finally, the isopropanol scavenged the

photoinduced holes and formed  $CO_2$ ,  $H_2O$ , and other products. This charge transfer maintains the recombination of holes and electrons. The electrons accumulated on  $[Ag_4(H_2O)(L)_3(SiW^{VI}_{12}O_{40})]$  were responsible for reducing Cr(VI). It was concluded that the much larger  $[Ag_4(H_2O)(L)_3]^{4+}$  metal-organic unit, in comparison to the other metal-organic units presented in other above-mentioned inorganic-organic hybrids, is probably responsible for the higher photocatalytic activity of the  $[Ag_4(H_2O)(L)_3(SiW^{VI}_{12}O_{40})]$  compared to the other three compounds.<sup>201</sup> Adsorption is the other most used purification technique to remove heavy metals from wastewater. In order to prepare a multi-functional composite, Herrmann *et al.*<sup>63</sup> used a combination of lacunary Keggin anions  $[\alpha-SiW^{VI}_{11}O_{39}]^{8-}$  and tetra-*n*-alkyl ammonium cations ( $(n-C_6H_{13})_4N^+$  and  $(n-C_7H_{15})_4N^+$ ) to prepare a highly viscous, lipophilic POM-IL complex, which was then immobilized on porous silica to give POM-SILP.<sup>165</sup> Each component of the POM-SILP composite contributed to the removal of a specific type of water contaminant. The lacunary Keggin tungstate anions (**Figure 2.G**) were responsible for metal-ion binding, whereas the long-chain quaternary organo-ammonium cations<sup>202</sup> acted as an antimicrobial. In addition, the POM-IL lipophilicity enabled the adsorption of organic contaminants, and the silica support bound radionuclides. Thus, using the water-insoluble POM-SILP composite in filtration columns allowed the simultaneous removal of toxic heavy metals (as  $Ni^{2+}$ ,  $Pb^{2+}$ ,  $Cu^{2+}$ ,  $Cr^{3+}$  and  $Co^{2+}$ ), microbes (*E. coli*), organic aromatics (trityl dye), and nuclear waste ( $UO_2^+$ ) from water (**Figure 6**).<sup>63</sup>

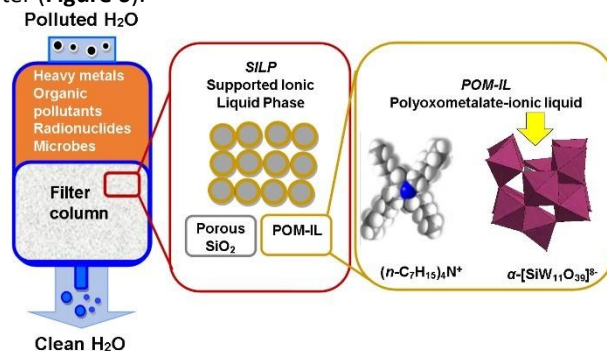


**Figure 6.** Water purification using POM-SILPs: the POM-SILP column filter removes toxic heavy metals (*e.g.*  $Ni(II)$ ,  $Pb(II)$ ,  $UO_2(II)$ ), microbes (*E. coli*), and aromatic organic pollutants (*e.g.* trityl dyes) due to the presence of lacunary polyoxometalate anions with specific metal-binding sites (yellow arrow) and antimicrobial tetra-alkyl ammonium cations. Reproduced from Ref. 63 with permission from Wiley-VCH, Copyright 2017.

The highly hydrophobic nature of POM-IL leads to surface heterogeneity and thus facilitates biphasic removal of metal ions from aqueous solutions. At the same time, the negative charge present on the POM units is the driving force for the removal of metal ions with a positive charge. In order to increase the removal of heavy metals from water by POM-IL, Shakeela and Rao synthesized a series of Keggin-based ionic liquids by reacting in situ generated first-row transition-metal ion ( $Mn^{2+}$ ,  $Fe^{3+}$ ,  $Co^{2+}$ ,  $Ni^{2+}$ ,  $Cu^{2+}$ , and  $Zn^{2+}$ ) substituted monolacunary Keggin with tetraoctylammonium (TOA) cations.<sup>203</sup> Metal-substituted lacunary POMs carried a relatively higher negative charge which facilitated the absorption of metal cations. Thus, all these thermoreversible POM-ILs effectively



removed  $\text{Cd}^{2+}$  and  $\text{Pb}^{2+}$  metal ions from the aqueous phase.<sup>203</sup> Embedding POM-ILs with tri-lacunary Keggin [ $\alpha\text{-PW}^{\text{VI}}_9\text{O}_{34}$ ]<sup>9-</sup> featuring coordinative binding of up to six metal cations into 3D printed organic polymers<sup>204</sup> has been shown to produce a highly porous organic-inorganic composite for effective transition-metal removal (Figure 7).<sup>205</sup>

Cation exchange is another process for the removal of various metal cations from water. Synthetic inorganic ion exchangers with well-defined chemical and phase compositions appear to be the most suitable ones compared to organic ion exchangers due to higher thermal and chemical stability and higher exchange capacity and selectivity for a wide range of metal ions.<sup>113</sup> For example, Cronin's group designed an inorganic open framework nanocube-based  $\text{K}_{18}\text{Li}_6[\text{Mn}^{\text{II}}_8(\text{H}_2\text{O})_{48}\text{P}_8\text{W}^{\text{VI}}_{48}\text{O}_{184}]\cdot 108\text{H}_2\text{O}$ , from highly anionic crown-type POM ( $[\text{P}_8\text{W}^{\text{VI}}_{48}\text{O}_{184}]^{40-}$ ) and  $\text{Mn}^{\text{II}}$  as linkers to accommodate  $\text{Cu}^{\text{II}}$  cations from a solution into the network of channels and cavities. The cation-exchange capacity and rate are controlled by oxidizing the Mn linkers from +II to +III.<sup>206</sup> In some cases, POM-IL systems exhibited greater efficiency than conventional ion-exchange resins.<sup>207</sup>

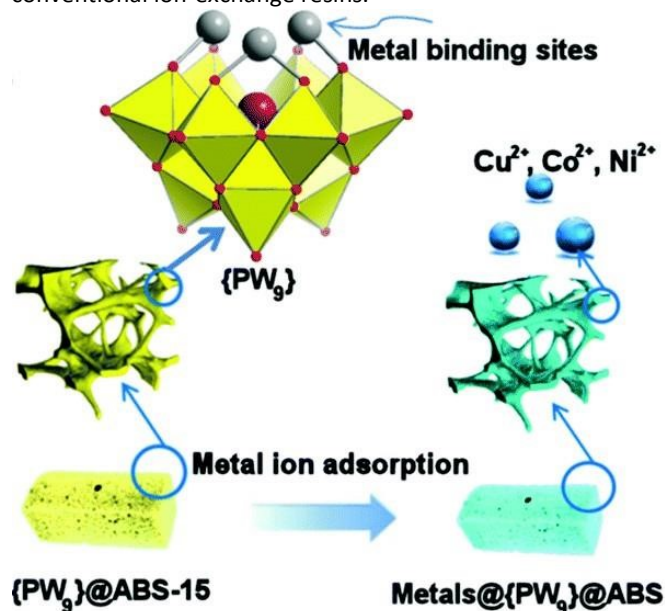


Figure 7. Schematic illustration of the POM-modified 3D-printed copolymer substrates used for transition-metal removal by the cation binding sites of the lacunary [ $\alpha\text{-PW}^{\text{VI}}_9\text{O}_{34}$ ]<sup>9-</sup>. Reproduced from Ref. 205 with permission from The Royal Society of Chemistry, Copyright 2018.

**2.2.2 Removal of radioactive metals.** Although metal-organic frameworks (MOFs) initially exhibited a unique performance for the adsorptive removal of metal ions, most of these materials have low stability in aquatic media, which has limited their applications for water purification. To improve the stability of MOFs, Zou *et al.* functionalized HKUST-1 MOF with Keggin-type POM [ $\text{H}_3\text{PW}^{\text{VI}}_{12}\text{O}_{40}$ ] POM (Figure 2.F) to form HKUST-1@[ $\text{H}_3\text{PW}^{\text{VI}}_{12}\text{O}_{40}$ ] under microwave conditions. It was proposed that the improved water stability of HKUST-1@[ $\text{H}_3\text{PW}^{\text{VI}}_{12}\text{O}_{40}$ ] was the result of POMs being encapsulated into HKUST-1 pores. The HKUST-1@[ $\text{H}_3\text{PW}^{\text{VI}}_{12}\text{O}_{40}$ ] showed high adsorption affinity and capacity towards selective adsorption of heavy metal ions (highly selective for  $\text{Pb}^{2+}$  and  $\text{Cd}^{2+}$ , but no adsorption of  $\text{Hg}^{2+}$ )

from contaminated water.<sup>208</sup> Studies on HKUST-1@[ $\text{H}_3\text{PW}^{\text{VI}}_{12}\text{O}_{40}$ ] adsorption ability to remove U(VI) from wastewater showed that it could selectively adsorb U(VI) from low concentration uranium solutions in the presence of other metal ions.<sup>209</sup> The adsorption capacity of HKUST-1@[ $\text{H}_3\text{PW}^{\text{VI}}_{12}\text{O}_{40}$ ] was strongly pH dependent and did not significantly decrease after three adsorption-desorption cycles. The presence of phosphate groups in the adsorbent structure has a great affinity for radioactive U(VI) ions in an aqueous solution.<sup>210,211</sup> In this regard, a ship-type nano-cage POM  $\{[\text{C}_5\text{NH}_5]_9[\text{H}_{31}\text{Mo}^{\text{VI}}_{12}\text{O}_{24}\text{Co}^{\text{II}}_{12}(\text{PO}_4)_{23}(\text{H}_2\text{O})_4]\}^{2-}$  (Co-POM) with 23  $\{\text{PO}_4\}$  groups was designed and synthesized. The high adsorption capacity of this POM-based inorganic framework for U(VI) ions in aqueous solution was mainly ascribed to coordination interaction between U(VI) and O in the phosphate groups on Co-POM which was proved by FT-IR and XPS analyses.<sup>212</sup> Composites of POMs ( $\text{H}_3\text{PW}^{\text{VI}}_{12}\text{O}_{40}$ ) with graphene oxide also exhibited a significant potential for uranyl uptake from wastewater.<sup>113</sup>

The cation exchange studies by POMs have been widely used to separate radioactive metal ions from radioactive wastes.<sup>109</sup> Kortz's group worked on a cyclic K<sup>+</sup>-templated POM,  $[\text{K}\{(\beta\text{-As}^{\text{III}}\text{W}_8\text{O}_{30})(\text{W}^{\text{VI}}\text{O}(\text{H}_2\text{O}))\}_3]^{14-}$ , which showed high selectivity to  $\text{Rb}^+$ , due to the relatively large size of the central cavity for  $\text{K}^+$  (Figure 8).<sup>114</sup> Uchida's group combined the Keggin cluster  $[\text{SiMo}^{\text{VI}}_{12}\text{O}_{40}]^{4-}$  anions with a cationic oxo-centered trinuclear complex, to produce ionic crystals with isolated pores,  $(\text{etpyH})_2[\text{Cr}_3\text{O}(\text{OOCH})_6(\text{etpy})_3]_2[\text{SiMo}^{\text{VI}}_{12}\text{O}_{40}]\cdot 3\text{H}_2\text{O}$  (etpy = 4-ethylpyridine), which selectively adsorbed  $\text{Cs}^+$  among alkali and alkaline earth metals *via* reduction of the Keggin  $[\text{SiMo}^{\text{VI}}_{12}\text{O}_{40}]$  with ascorbic acid.<sup>213</sup> The previously reported ionic crystal,  $(\text{mepyH})_2[\text{Cr}_3\text{O}(\text{OOCH})_6(\text{mepy})_3]_2[\text{PMo}^{\text{VI}}_{12}\text{O}_{40}]\cdot 5\text{H}_2\text{O}$  (mepy = 4-methylpyridine,  $\text{mepyH}^+$  = 4-methylpyridinium ion), with 1D open channels, was able to incorporate  $\text{Na}^+$  as well as  $\text{Cs}^+$  by the reduction-induced cation exchange processes.<sup>115</sup> The authors concluded that the high selectivity towards  $\text{Cs}^+$  is due to the existence of closed pores rather than open channels. Despite the high selectivity towards  $\text{Cs}^+$  however, several disadvantages such as the requirement of heating (343 K) and slow adsorption kinetics (12 h to reach equilibrium) limited the widespread application of

$(\text{mepyH})_2[\text{Cr}_3\text{O}(\text{OOCH})_6(\text{mepy})_3]_2[\text{PMo}^{\text{VI}}_{12}\text{O}_{40}]\cdot 5\text{H}_2\text{O}$ . Later, this group overcame disadvantages by utilizing the large-molecular size and easily reducible Wells-Dawson-type of POMs  $[\text{P}_2\text{M}^{\text{VI}}_{18}\text{O}_{62}]^{6-}$  (M = Mo, W).<sup>214</sup> In comparison with the Keggin-type POM, the larger molecular size and higher reduction potential of Dawson-type POM increased the pore volume and facilitated the reduction-induced  $\text{Cs}^+$  exchange. As expected, the capacity and rate of  $\text{Cs}^+$  uptake increased significantly (with only 1 h to reach equilibrium at room temperature), demonstrating the potential application of these adsorbents for radioactive  $\text{Cs}^+$  ( $\text{Cs-137}$ ) removal.<sup>214</sup>



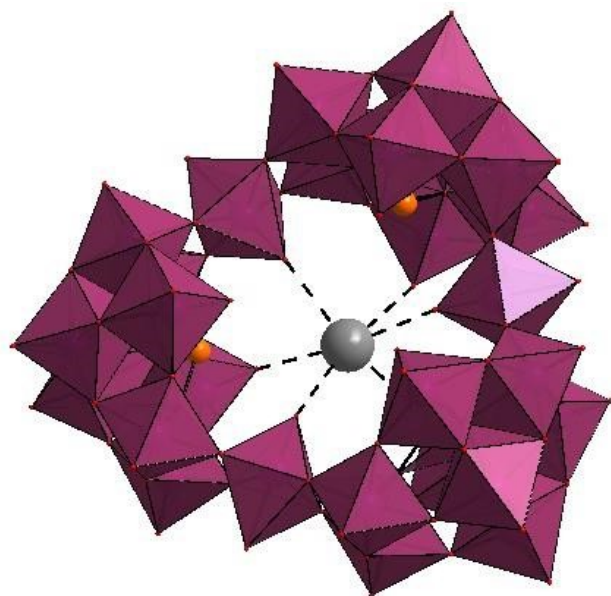


**Figure 8.** Structure of  $[M\{(\beta\text{-As}^{\text{III}}\text{W}_8\text{O}_{30})(\text{WO}(\text{H}_2\text{O}))_3\}]^{14-}$  with the central guest being either  $\text{K}^+$  or  $\text{Rb}^+$ . Color code:  $\text{WO}_6$  (violet octahedra), As (orange), K/Rb (grey).<sup>114</sup>

## 2.3 Removal of organic pollutants

**2.3.1 Removal of organic dyes.** As shown in Table S2 (Supporting Information), the decontamination mechanisms, in the case of organic pollutants, are similar to previously discussed methods for inorganic ones. Adsorption of dye molecules, especially cationic ones, by POMs is strongly governed by solution pH. The selective adsorption of methylene blue (MB) in the presence of methyl orange (MO) over  $[\text{P}_2\text{W}^{\text{VI}}_{18}]/\text{MOF-5}$  catalyst is spontaneous and endothermic. In addition, the pH value of dye solution should also be carefully controlled to obtain maximum adsorption capacity, because the surface charge of the adsorbent is strongly affected by the pH ( $\text{pH}_{\text{PZC}}$ ; PZC = point-of-zero charge).<sup>215</sup> Furthermore, oxidation and reduction processes are responsible for the high negative charge on the POM surface at lower pH values.<sup>216</sup>

In a generally accepted approach, photooxidation of dye molecules occurs through generation of free  $\text{OH}^\bullet$ . The proposed mechanism is based on the photoexcitation of  $\text{Cs}_4\text{SiW}^{\text{VI}}_{12}\text{O}_{40}$  POM and a subsequent hydrogen abstraction reaction which results in the homolytic bond cleavage of  $\text{H}_2\text{O}$ . The photocatalytic activity of POMs, such as  $[\text{SiW}^{\text{VI}}_{12}\text{O}_{40}]^{4-}$ , can be enhanced in the presence of semiconductors. In fact, in such heterojunction structures with suitable energy band alignment, photogenerated carriers could be separated more efficiently.<sup>217</sup> Dye sensitization is another mechanism that may contribute to dye degradation in photocatalytic reactions. Due to the visible-light absorption abilities of the sensitizers, dye-sensitized POM photocatalysts can be excited upon visible-light irradiations. In these cases, the oxidation of dye proceeds through electron transfer between the excited dye (e.g., thionine, phthalocyanine) and LUMO of Keggin ( $[\text{PW}^{\text{VI}}_{12}\text{O}_{40}]^{3-}$ )<sup>218,219</sup> or Wells-Dawson-type ( $[\alpha\text{-P}_2\text{W}^{\text{VI}}_{18}\text{O}_{62}]^{6-}$  ( $\text{P}_2\text{W}_{18}$ ) and  $[\alpha\text{-P}_2\text{W}^{\text{VI}}_{17}\text{O}_{61}]^{10-}$ )<sup>218</sup> type POMs.<sup>218,219</sup>

As an interesting example of membrane filtration technology, Yao *et al.*<sup>179</sup> incorporated surfactant-encapsulated POM microparticles into a PVDF matrix as a microfiltration membrane for the adsorptive removal of the anionic dye Reactive Black 5 (RB5). The authors prepared spherical microparticles through an ion exchange reaction between a cationic surfactant (DODA-Br) and  $[\text{PV}^{\text{VI}}_2\text{Mo}^{\text{VI}}_{10}\text{O}_{40}]^{5-}$ . This architecture enhanced the flow rate of the system and dye removal efficiency reached up to 97.5 % within 120 min.<sup>179</sup> A similar concept has been applied in the case of surface-active ionic-liquid-encapsulated POMs.<sup>220</sup> Ion exchange reaction has also been used to replace small anions in the structure of layered double hydroxides (LDHs) with large polyanions. By this method the surface area of the resulting composite can be enhanced, since the interlayer distances of LDH increase. These composites have been used for the removal of cationic dyes from water; however, the instability of LDH in acidic media may limit their application.<sup>221,222</sup> In 2005 Zhao and co-workers suggested that an active peroxy species is responsible in the photo-Fenton oxidation of Rhodamine B (RhB) under visible light irradiation. The authors proposed that the active species is formed upon the interaction of reduced POM with  $\text{H}_2\text{O}_2$ .<sup>223</sup> Similarly, in Fenton systems the active species is formed by the coordination of iron to  $[\text{PW}^{\text{VI}}_{12}\text{O}_{40}]^{3-}$  POM.<sup>224</sup> In Fenton-like systems the iron species is replaced with different POMs, like mentioned Keggin<sup>224</sup> or  $[\text{HPW}^{\text{VI}}_4\text{W}^{\text{VI}}_8\text{O}_{40}]^{6-}$  POMs.<sup>225</sup> The radical-based pathways, however, can enhance apparent degradation rate if not properly identified or controlled.

Among different transition metals (Co, Ni, Cu), Co-substituted Wells-Dawson anions  $[\alpha\text{-P}_2\text{W}^{\text{VI}}_{17}\text{CoO}_{61}]^{8-}$  exhibited higher catalytic performance.<sup>226</sup> Li's group prepared two POMCPs,  $[\text{Ag}_4(\text{H}_2\text{pyttz-I})(\text{H}_2\text{pyttz-II})(\text{Hpyttz-II})][\text{HSiW}^{\text{VI}}_{12}\text{O}_{40}] \cdot 4\text{H}_2\text{O}$  ( $\text{H}_2\text{pyttz-I}$  = 3-(pyrid-2-yl)-5-(1H-1,2,4-triazol-3-yl)-1,2,4-triazolyl) and  $[\text{Ag}_4(\text{H}_2\text{pyttz-II})(\text{Hpyttz-II})_2][\text{H}_2\text{SiW}^{\text{VI}}_{12}\text{O}_{40}] \cdot 3\text{H}_2\text{O}$  ( $\text{H}_2\text{pyttz-II}$  = 3-(pyrid-4-yl)-5-(1H-1,2,4-triazol-3-yl)-1,2,4-triazolyl) with similar structure and different tunnels (Figure 9a). The photocatalytic degradation of methylene blue (MB) demonstrated that the structure of the hybrids influences the photocatalytic properties. The larger cavities in the compound and  $[\text{Ag}_4(\text{H}_2\text{pyttz-II})(\text{Hpyttz-II})_2][\text{H}_2\text{SiW}^{\text{VI}}_{12}\text{O}_{40}] \cdot 3\text{H}_2\text{O}$  increase the contact area between catalysts and crude materials and promote more active sites to participate in the reactions process. Thus, the photocatalytic properties of  $\text{Ag}_4(\text{H}_2\text{pyttz-II})(\text{Hpyttz-II})_2][\text{H}_2\text{SiW}^{\text{VI}}_{12}\text{O}_{40}] \cdot 3\text{H}_2\text{O}$  were improved. The proposed mechanism for enhanced photocatalytic activity in these hybrids is shown in Figure 9b. This mechanism includes LMCT from the HOMO to the LUMO, which was facilitated by Ag–O bridging units. In addition to this, Ag–pyttz acted as photosensitizers and promoted the transition of electrons onto  $[\text{SiMo}^{\text{VI}}_{12}\text{O}_{40}]^{4-}$  POMs. Therefore, the  $[\text{SiMo}^{\text{VI}}_{12}\text{O}_{40}]^{4-}$  POMs had



a higher charge density and exhibited a considerable impact on the photocatalytic degradation of RhB.<sup>227</sup>

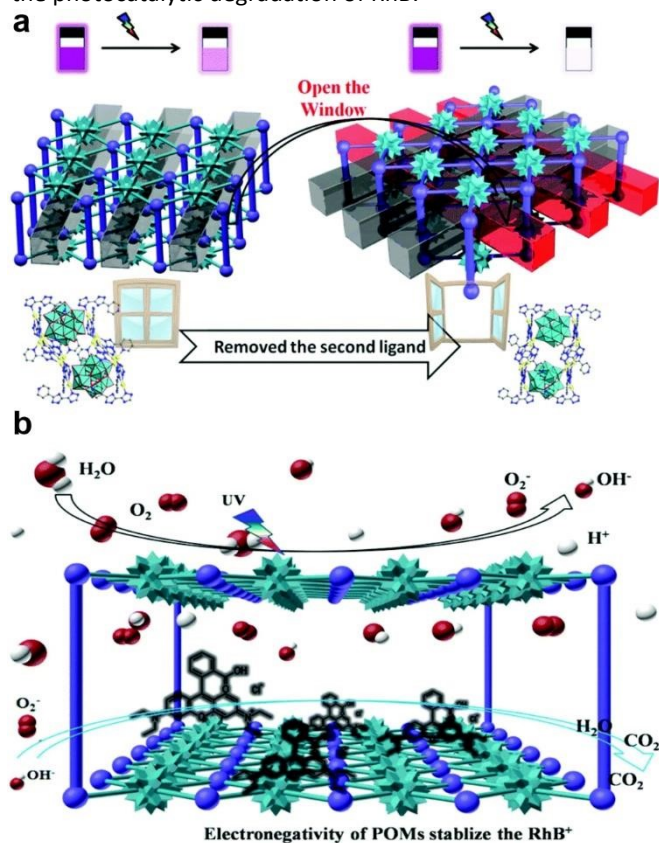


**Figure 9.** a) Representation of the [Ag<sub>4</sub>(H<sub>2</sub>pyttz-II)(H<sub>2</sub>pyttz-II)(Hpyttz-II)] [HSiW<sub>12</sub>O<sub>40</sub>] and [Ag<sub>4</sub>(H<sub>2</sub>pyttz-II)(Hpyttz-II)<sub>2</sub>][H<sub>2</sub>SiW<sub>12</sub>O<sub>40</sub>] compounds ((H<sub>2</sub>pyttz-II = 3-(pyrid-2-yl)-5-(1H-1,2,4-triazol-3-yl)-1,2,4-triazolyl) and H<sub>2</sub>pyttz-II = 3-(pyrid-4-yl)-5-(1H-1,2,4-triazol-3-yl)-1,2,4-triazolyl) with similar underlying frameworks and different tunnels. b) Representation of the photocatalytic mechanisms for POMCPs. Reproduced from Ref. 227 with permission from The Royal Society of Chemistry, Copyright 2015.

**2.3.2 Removal of aromatic hydrocarbons.** The oxidative potential of POMs has been broadly used in AOPs for phenol oxidation.<sup>227</sup> For example, [PW<sub>11</sub>O<sub>39</sub>Fe<sup>III</sup>(H<sub>2</sub>O)]<sup>4-</sup> can degrade chlorophenol (CP) compounds only if H<sub>2</sub>O<sub>2</sub> is added to the solution. No photocatalytic activity was observed in aerated aqueous solution. In addition, the reaction rate was influenced by the initial concentration of the catalyst or H<sub>2</sub>O<sub>2</sub> and the number of chlorines in the aromatic ring of CP.<sup>168</sup> Iron-containing POMs have also been used to construct heterojunction photocatalysts by grafting Fe-POM nanoclusters onto oxygen-deficient TiO<sub>2</sub>. The synergistic effect between photocatalysis and Fenton-like reactions resulted in efficient degradation of sulfosalicylic acid (SSA).<sup>228</sup> Deposition of Au NPs on the surface of POM/TiO<sub>2</sub> is another strategy to improve light absorption and activity of the catalyst. A 4.6-fold increase was observed in photocatalytic degradation of nitrobenzene (NBZ).<sup>229</sup> Zhang *et al.* prepared a ferrocene-containing silicotungstate catalyst *via* a co-precipitation method for the photocatalytic oxidation of 4-chlorophenol (4-CP). It was suggested that the synergism between ferrocene and silicotungstate leads to the charge-transition from ferrocene to the POM unit, which ultimately contributes to the oxidation of the organic pollutant through a Fenton-like mechanism.<sup>230</sup> In another study, [Cs<sub>3</sub>PMo<sup>VI</sup><sub>12</sub>O<sub>40</sub>] was used as a modifier of the

semiconductor Bi<sub>2</sub>O<sub>3</sub>. The experimental results indicated that the [Cs<sub>3</sub>PMo<sup>VI</sup><sub>12</sub>O<sub>40</sub>] generated on the surface of the semiconductor creates a P–N heterojunction photocatalyst with visible-light activity in the degradation of phenol. The best photocatalytic performance was observed when 2.5 % (mol) of [Cs<sub>3</sub>PMo<sup>VI</sup><sub>12</sub>O<sub>40</sub>] was added to the semiconductor. Also, trapping experiments showed that the major active species involved in the degradation process are superoxide and hydroxyl radicals.<sup>231</sup> Heterogenization of POMs with graphene aerogels (GA) has also shown promise in the adsorptive removal of a series of organic compounds from water.<sup>232</sup> A more comprehensive analysis of the studies from the past 5 years is provided in **Table S2** in Supporting Information.

## 2.4 Summary of water treatment technologies by polyoxometalates

Although the literature review shows promising evidence on how POM-based materials have attracted considerable attention for water treatment, like any emerging technology, they also have their own set of challenges and limitations. As tabulated in **Table S2**, POM-based materials have often been utilized as photocatalysts with high removal efficiencies. A key negative result that is rarely reported, but likely exists, is the structural instability of POM-based photocatalysts under realistic water matrices (containing chloride, carbonate, or natural organic matter). Such components can significantly suppress the photocatalytic activity or even partially decompose the structure, yet these effects are often not disclosed. Acknowledging this limitation is important for assessing the practical applicability of POM materials. For their broad implementation, they must also maintain the cost of processed water as low as possible. In this regard, substantial costs associated with synthesizing POMs and their composites remain as a significant challenge. In terms of the technology itself, other economically beneficial methods such as adsorption and ion exchange should also be considered, as they tend to provide more affordable solutions for water purification.

## 3 Removal of emerging health pollutants

Some of the most prominent classes of emerging health pollutants (EPs) are pharmaceuticals (antibiotics, antifungals, antidepressants, synthetic hormones)<sup>12,13,18,27,28,233</sup> plant protection products (pesticides, biocides)<sup>31,234</sup>, and microplastics.<sup>234,236,237</sup> Excessive use of antibiotics and cosmetic products, *e.g.*, disinfectants and cleaning products, has led to the development of bacterial resistance through DNA mutations of bacterial cells, which have resulted in the adaptation and resistance of bacteria to these products.<sup>24,25,238</sup> In addition, bacterial resistance also occurs through the horizontal gene transfer mechanism from resistant bacteria to non-resistant bacteria through transformation, transduction, or conjugation.<sup>25</sup> Moreover, water bodies containing EPs play an essential role in this horizontal gene transfer mechanism by facilitating the horizontal gene transfer from pathogenic to non-



pathogenic microorganisms. In addition to contributing to the development of antibiotic resistance, pollutants such as UV filters from sunscreens have been shown to harm marine life significantly. These compounds accumulate in aquatic environments and negatively affect organisms, including phytoplankton, corals, microalgae, and sea urchins, by disrupting their physiology and ecosystem functions.<sup>24,239</sup>

A study, conducted over two consecutive years (2015 and 2016), on the final effluents from wastewater treatment plants in Europe, revealed high average concentrations of antibiotics in wastewater, especially in countries such as Portugal, Spain, and Ireland. The study identified that the most commonly found antibiotics, ciprofloxacin, azithromycin, and cephalexin, have a potentially significant impact on aquatic systems and the development of antibiotic resistance.<sup>24,240</sup>

Ciprofloxacin, a fluoroquinolone antibiotic, and erythromycin have also been detected in effluents and surface waters in other studies<sup>24</sup>, and are included, along with the macrolides azithromycin and clarithromycin, as well as the penicillin-type antibiotic amoxicillin, in the surface water Watch List under the European Water Framework Directive.<sup>17,240,241</sup> More recently, this report has been updated to include other pharmaceutical products such as the antibacterials sulfamethoxazole and trimethoprim, the antifungal clotrimazole, fluconazole, and miconazole, the antidepressant venlafaxine, and the synthetic hormone norethisterone (**Figure 10**).<sup>240,241</sup> In addition to the aforementioned pharmaceuticals, such as proton pump inhibitors (PPIs), lansoprazole and omeprazole,<sup>242,243</sup> have been proposed as potential Watch List candidates due to their recently discovered possible mutagenic and toxic effects on aquatic organisms.<sup>17,25,240</sup>

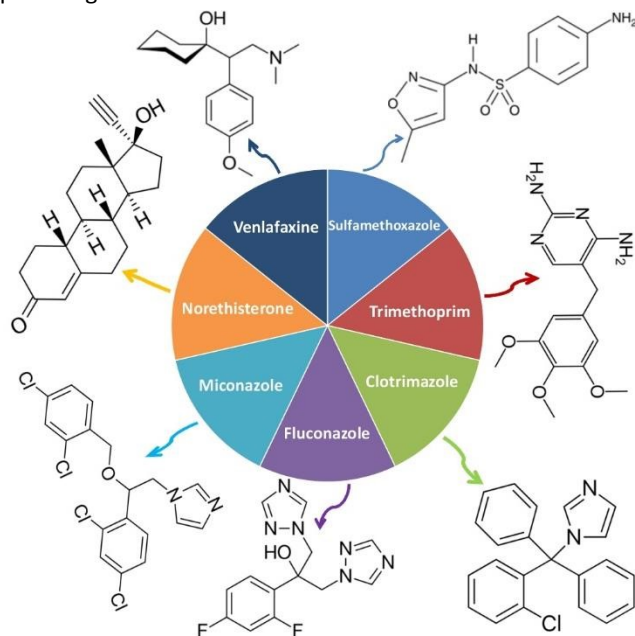


**Figure 10.** Emergent pharmaceuticals pollutants included in the updated 4th water watch list under the European Water Framework Directive: the antibacterial sulfamethoxazole and trimethoprim; the anti-fungus clotrimazole, fluconazole and miconazole; the antidepressant venlafaxine and the synthetic hormone norethisterone.<sup>17</sup>

Herein, we focus on the POMs' ability to degrade priority pharmaceuticals, mainly antibiotics, pesticides, microplastics,

and dyes, to identify POMs with higher removal efficiency and kinetics, thus facilitating the development of more environmentally friendly POM materials.<sup>244,245</sup>

### 3.1 Removal of pharmaceutical pollutants

Every day, humans release pharmaceutical products into the environment in different forms and under different circumstances. This behavior of humanity has a major impact on health and economy and has a profound effect on our lives. It is therefore of great importance to conduct environmental protection in an effective and inexpensive manner to combat emerging health pollutants. Some of the most prominent classes of emerging pharmaceutical pollutants are the antimicrobial pharmaceuticals (antibiotics, antifungals) and other pharmaceuticals (antidepressants, synthetic hormones). It has been described that contamination of the environment with these pharmaceutical products can lead to bacterial resistance, which is an emerging and growing phenomenon worldwide in the 21<sup>st</sup> century.<sup>10,20,22,24,246</sup> Nonconventional low-cost adsorbents for pharmaceutical removal from wastewater, pollutant removal mechanisms, and detection using nanodevices and polymer-based adsorbents, as well as using fungal treatments, were recently summarized.<sup>12,13,18</sup> POMs have also been used for the detection of several pharmaceuticals, such as drugs of abuse<sup>247</sup> and triclosan (TCS)<sup>248</sup>, as well for the selective extraction of antidepressants in undiluted urine.<sup>249</sup> TCS, a diphenyl ether with antibacterial properties, is used as a disinfectant in antiseptic creams, toothpaste, hand soaps, deodorants, and even in plastics.<sup>21,22</sup> In Europe, TCS is one of the most frequently detected contaminants in wastewater. However, studies from the United States have reported that its concentration in wastewater can be up to five times higher.<sup>22</sup> TCS has already been detected in surface waters in several regions of the world, including in fish tissues. In fact, the methylated form of TCS (M-TCS) is bioaccumulative in tissues, due to its lipophilic properties and stability. Moreover, it has been described that contamination of the environment with TCS can lead to bacterial resistance to four antibiotics: chloramphenicol, tetracycline, ciprofloxacin, and colistin. This resistance poses potential risks to human health as well as aquaculture.<sup>21,22</sup>

Of the seventeen pharmaceutical pollutants mentioned above, only one study has referred to the removal of ciprofloxacin by POMs. He *et al.* immobilized three Keggin-type POMs [ $\text{H}_3\text{PMo}^{\text{VI}}_{12}\text{O}_{40}$ ] $\cdot n\text{H}_2\text{O}$ , [ $\text{H}_3\text{PW}^{\text{VI}}_{12}\text{O}_{40}$ ] $\cdot n\text{H}_2\text{O}$ , and [ $\text{H}_3\text{PW}^{\text{VI}}_{12}\text{O}_{40}$ ] $\cdot n\text{H}_2\text{O}$  onto nitrogen-deficient carbon nitride nanosheets (*g*- $\text{C}_3\text{N}_4$ ) and successfully utilized all three POM-based composites (**Figure 11.A**) for the removal of ciprofloxacin within only five minutes under visible light irradiation with 93.1 %, 97.4 % and 95.6 % efficiency, respectively.<sup>250</sup> This type of POM-based hybrid material was further explored on *g*- $\text{C}_3\text{N}_4/\text{PW}_{12}/\text{TiO}_2$  composites ( $\text{PW}_{12} = [\text{H}_3\text{PW}^{\text{VI}}_{12}\text{O}_{40}]$ ) (**Figure 11.A-B**)<sup>250,251</sup>, which showed remarkable and stable photocatalytic performance under visible light irradiation, not only for the removal of TC but also for bisphenol A and Cr(VI).<sup>251</sup> Their removal properties and stability without any observed



structural changes in the photocatalyst were attributed to the enhanced adsorption under visible light irradiation, a high specific surface area, effective separation, and photoinduced charge transfer via g-C<sub>3</sub>N<sub>4</sub> and PW<sub>12</sub>.<sup>251</sup>

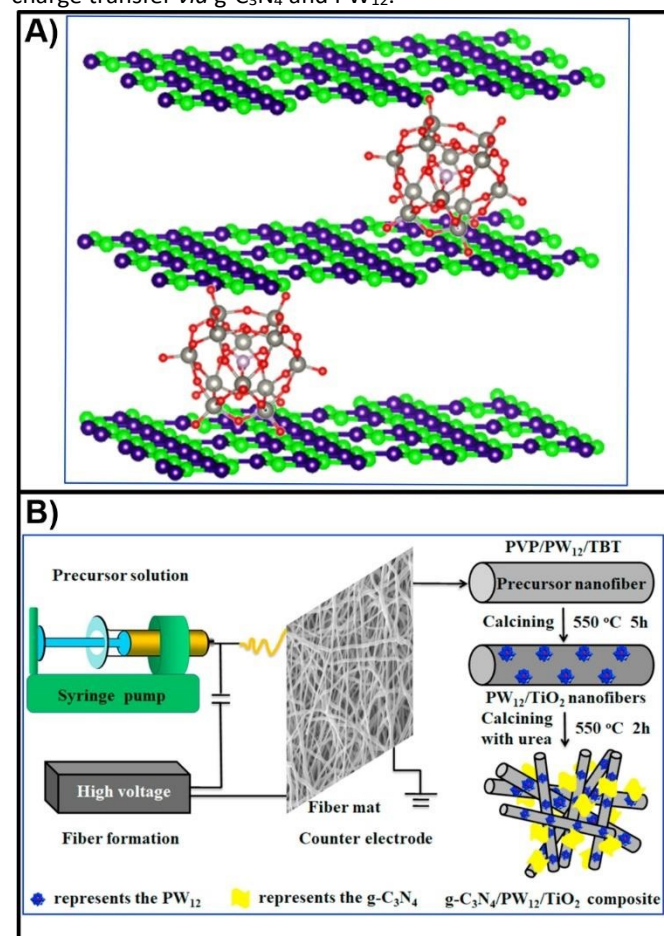


Figure 11. A) Nitrogen-deficient g-C<sub>3</sub>N<sub>4</sub>/POMs porous nanosheets (where x denotes N-deficiency) with P-N heterojunctions capable of photocatalytic degradation of drugs; Recreated from Ref. 250 with permission from The Royal Society of Chemistry. B) Fabrication of g-C<sub>3</sub>N<sub>4</sub>/PW<sub>12</sub>/TiO<sub>2</sub> composite with enhanced photocatalytic performance under visible light; Reproduced from Ref. 251 with permission from Elsevier, Copyright 2021.

Moreover, Cheng *et al.*<sup>252</sup> have utilized the isopolyoxotungstate, decatungstate [W<sup>VI</sup><sub>10</sub>O<sub>32</sub>]<sup>4-</sup> (Figure 2.D) as a photocatalyst for the oxidation of sulfasalazine (SZZ)<sup>253</sup>, an antibiotic commonly found in wastewater, and its human metabolite sulfapyridine (SPD). After 120 min in the presence of H<sub>2</sub>O<sub>2</sub> and under UV irradiation, the metabolite SPD was more efficiently removed (75 %) by decatungstate than was the SZZ antibiotic (25 %). The proposed photocatalytic mechanism (Figure 12), which involves the generation and utilization of hydroxyl radicals (\*OH) in the photocatalytic degradation of sulfasalazine<sup>252</sup>, has attracted increasing attention over the past decades. This mechanism has been extensively studied in the ongoing research and development of novel pollution removal technologies.<sup>254,255</sup> Therefore, a similar strategy has been employed for the photodegradation of antibiotics such as nitrofurazone, tetracyclines and berberine under UV or visible light irradiation. This process utilizes H<sub>2</sub>O<sub>2</sub> and the photoactive POM-based composite [H<sub>3</sub>PW<sub>12</sub>O<sub>40</sub>]<sup>3-</sup>@β-EDA-CD, as shown in Figure 13.A.<sup>256</sup>

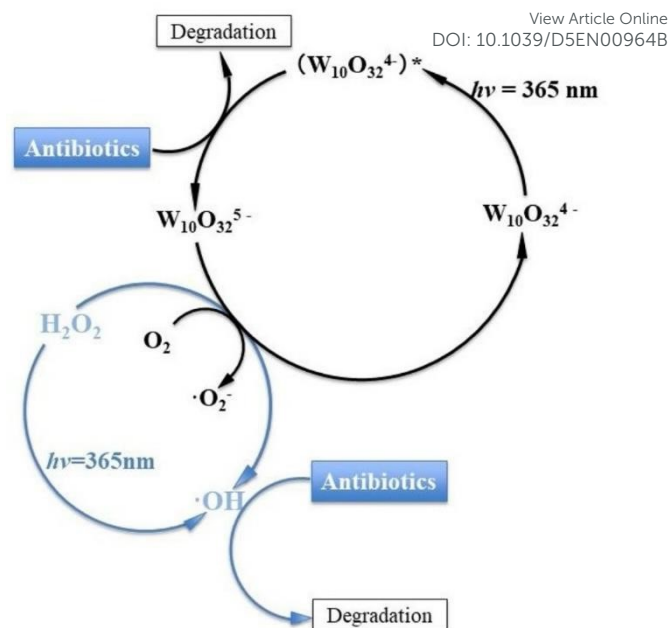


Figure 12. Cycle of photocatalysis and degradation of antibiotics (left) through the isopolyoxometalate decatungstate. Reproduced from Ref. 252 with permission from Elsevier, Copyright 2002

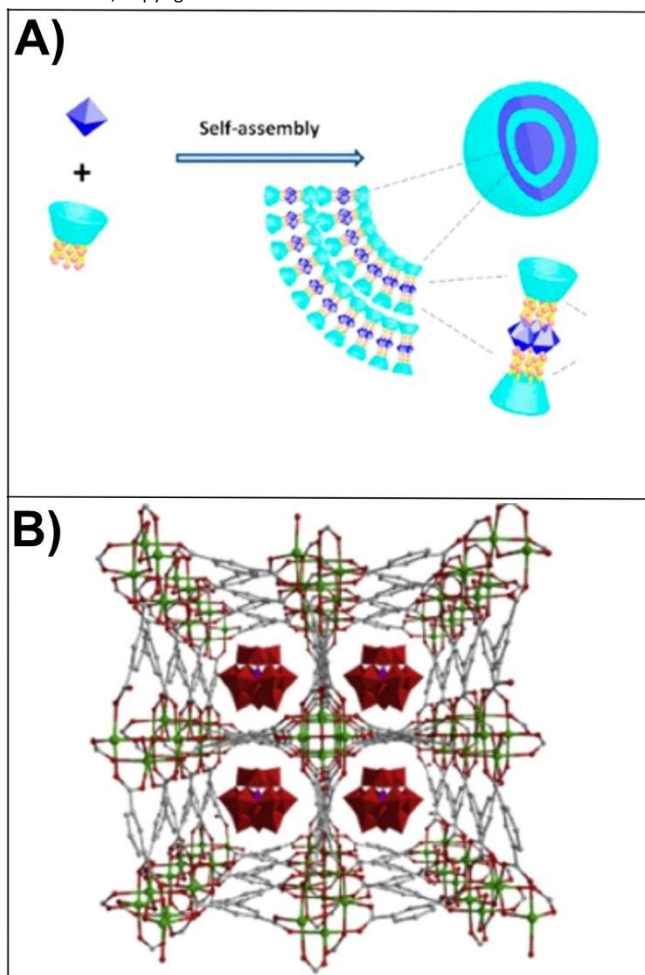


Figure 13. A) Multivalent supramolecular self-assembly between β-Cyclodextrin derivatives and polyoxometalate for photodegradation of dyes and antibiotics; Reproduced from Ref. 256 with permission from The American Chemical Society, Copyright 2019. B) Encapsulate polyoxometalate into metal-organic frameworks as efficient and recyclable photocatalyst for drugs degradation; Reproduced from Ref. 257 with permission from Elsevier, Copyright 2019.

Li *et al.* prepared a POM-based photocatalyst, PW<sub>12</sub>@MFM-300(In) (**Figure 13.B**), by using an environmentally friendly solvent-free method for the encapsulation of the POM [H<sub>3</sub>PW<sup>VI</sup><sub>12</sub>O<sub>40</sub>] into the metal-organic framework MFM-300(In). The PW<sub>12</sub>@MFM-300(In) composite displayed its activity for room temperature visible-light-driven catalytic degradation of the pharmaceutically active compound SMT with a 98 % removal efficiency within 2 h.<sup>257</sup>

### 3.2 Removal of pesticides, microbes and microplastic

POM-based catalysts have been used for decades in pesticide degradation. The decatungstate [W<sup>VI</sup><sub>10</sub>O<sub>32</sub>]<sup>4-</sup>, mentioned in the context of the removal of pharmaceutical pollutants (Section 3.1), also showed photocatalytic activity in the degradation of two common pesticides, 2-(1-naphthyl)acetamide (NAD) and 2-mercaptobenzothiazole (MBT). In the study of da Silva *et al.*, it was shown that [W<sup>VI</sup><sub>10</sub>O<sub>32</sub>]<sup>4-</sup> could promote UV-light-driven degradation of NAD with an efficiency of 89 % within 8 h.<sup>258</sup> Additionally, Allaoui *et al.* described the photodegradation of the pesticide MBT using Na<sub>4</sub>W<sup>VI</sup><sub>10</sub>O<sub>32</sub> as a catalyst with an efficiency of 90% within 8 h.<sup>259</sup> It has been proposed that the photodegradation of MBT occurs *via* e<sup>-</sup> transfer and H-atom abstraction processes with W<sup>VI</sup><sub>10</sub>O<sub>32</sub><sup>4-</sup>\* excited species. The main products of such photodegradation when using decatungstate as a catalyst are monohydroxylated products, sulfoxide derivatives, and dimers of MBT. The whole process was shown to be O<sub>2</sub> dependent because photodegradation was restricted by W<sup>VI</sup><sub>10</sub>O<sub>32</sub><sup>5-</sup> reoxidation.<sup>259</sup> The Keggin-type POM [PW<sup>VI</sup><sub>12</sub>O<sub>40</sub>]<sup>3-</sup> showed activity for the complete photocatalytic degradation of the pesticide lindane to CO<sub>2</sub>, H<sub>2</sub>O, and Cl<sup>-</sup> in an aqueous solution.<sup>260</sup> Photocatalysis of lindane by [PW<sup>VI</sup><sub>12</sub>O<sub>40</sub>]<sup>3-</sup> follows the same principle as that of TiO<sub>2</sub> catalysis, *i.e.* processes involving both oxidation and reduction pathways such as chlorination, dechlorination, hydroxylation, hydrogenation, dehydrogenation, which lead to the C-C bond cleavage and complete mineralization to the final products.<sup>260</sup> Recently, a POM-IL<sup>261</sup> has also been used for the extraction of triazole pesticides (*e.g.*, penconazole, hexaconazole, diniconazole, tebuconazole, triticonazole, and difenconazole) from aqueous samples.<sup>262</sup> In that article, the prepared POM-IL nanomaterial ([3-(1-methylimidazolium-3-yl)propane-1-sulfonate]<sub>3</sub>PW<sup>VI</sup><sub>12</sub>O<sub>40</sub>) was utilized as a coating for a new solid-phase microextraction (SPME) device that was then successfully applied for the extraction of the six triazole pesticides from real aqueous samples. The longevity experiments (at least 50 extractions) of POM-IL coated SPME devices compared with commercially available PDMS-coated SPME devices (PDMS = polydimethylsiloxane) showed that the newly prepared device offers higher extraction efficiency and better longevity.<sup>262</sup> Moreover, the type of POM-IL material (**Figure 6**), already described in Section 2.2, was shown to efficiently remove previously mentioned inorganic and organic contaminants from wastewater, as well as various microbial pollutants, *E. coli* and *B. subtilis*.<sup>63</sup> Recent developments in these organic/inorganic hybrid materials, POM-based ionic liquid crystals and POM-ILs,

and their applications, mainly in pollutants degradation, including microplastics, have been reviewed.<sup>263</sup>

Microplastics (MPs) are among the newly emergent health pollutants of worldwide concern, and their impact on human health and the environment is not yet completely understood.<sup>264</sup> The first reported example of magnetic polyoxometalate-based ionic liquid phases (magPOM-SILPs) for the removal of MPs was designed by anchoring a POM-IL composite (POM = [α-SiW<sup>VI</sup><sub>11</sub>O<sub>39</sub>]<sup>8-</sup> (**Figure 2.F**); IL = (*n*-C<sub>7</sub>H<sub>15</sub>)<sub>4</sub>N<sup>+</sup>) to an Si-enclosed Fe<sub>2</sub>O<sub>3</sub> supermagnetic core, Fe<sub>2</sub>O<sub>3</sub>@SiO<sub>2</sub> (**Figure 14**). The magPOM-SILPs composite showed remarkable effectiveness (90%) for removing microplastic by binding MPs particles via the formation of hydrophobic interactions with the MPs surface and then removing MPs pollutants from water samples by magnetic recovery (**Figure 14**).<sup>263</sup>

Cobalt-based POMs, Na<sub>10</sub>[Co<sub>4</sub>(H<sub>2</sub>O)<sub>2</sub>(V<sup>VI</sup>W<sup>VI</sup><sub>9</sub>O<sub>34</sub>)<sub>2</sub>].34H<sub>2</sub>O were also examined for dye degradation. MB and RhB dyes were chosen as the subject dyes for the degradation test because of their carcinogenic properties and wide use in the textile industry. A 10 mg/L dosage of this POM removed 87.8 % of MB in 30 min. The time required for the complete decomposition of RhB was almost twice as long as that of MB. In this study, in addition to the excellent dye catalytic activity, these CoV-POMs also showed anticancer activities.<sup>265</sup> However, POMs anticancer, antibacterial studies, and other biomedical studies are described elsewhere.<sup>85,266,267,268</sup> Another recent study, described the synthesis of two Keggin-type polyoxometalates ammonium phosphomolybdate (NH<sub>4</sub>)<sub>3</sub>PMo<sup>VI</sup><sub>12</sub>O<sub>40</sub> (PMo) and ammonium phosphotungstate (NH<sub>4</sub>)<sub>3</sub>PW<sup>VI</sup><sub>12</sub>O<sub>40</sub> (PW) that were used as adsorbents for the removal of various antibiotics and heavy metals from water systems. The adsorption efficiency of PMo for dyes and heavy metals was higher than that of PW for various antibiotics such as tetracycline. It was suggested that the more negative surface charges induced by Mo atoms with more electronegativity and higher specific surface area contributed to the superior adsorption efficiency of PMo for dyes and heavy metals.<sup>269</sup>

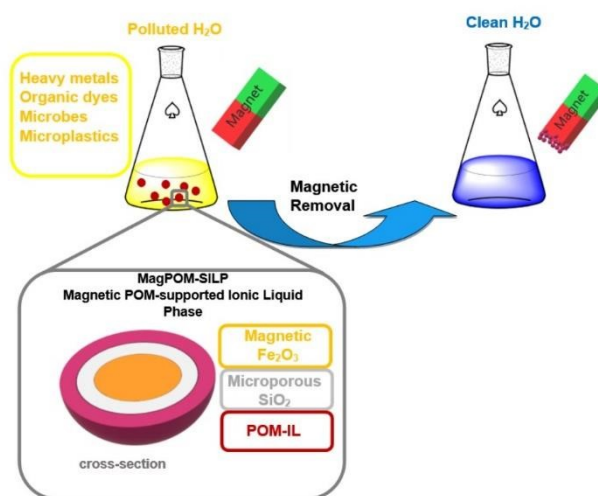


**Figure 14.** Magnetic polyoxometalate-supported ionic liquid (magPOM-SILPs) for heavy metals, organic dyes, microbes and microplastics water removal.<sup>263</sup>



**Table 1** summarizes the recent examples of POMs applications in removal of EPs covered in Section 3.

### 3.3. Summary of POM-based technologies in removal of emerging health pollutants

Section 3 highlights emerging pollutants in the 21<sup>st</sup> century environment, such as drugs, pesticides, and microplastics, and emphasizes their dangers and consequences for human health. Several examples illustrate the use of pure POMs, nanoparticles, composites, or MOFs for removing organic and

inorganic pollutants. The processes involving POMs in pollutant degradation are also discussed, many of which employ photocatalysis by UV and/or visible irradiation, in addition to adsorption or magnetic removal. In short, the different types of POMs mentioned in this section reveal their essential role in removing emerging pollutants from the environment, proving to be efficient and selective.

**Table 1.** Examples of recent polyoxometalates studies in pollutants degradation: antibiotics (A), dyes (D), plastics (P), industrial chemicals (IC) and pesticides (Pest).

Formula	POM Archetype	Pollutant	Conditions	Efficiency	Number of Cycles	Ref.
Na <sub>4</sub> W <sup>VI</sup> <sub>10</sub> O <sub>32</sub>	decatingstat e	sulfasalazine	c(catalyst) = 40 μM; under UV irradiation	25 % removal within 120 min	1	252
		(A) sulfapyridine		75 % removal within 120 min		
g-C <sub>3</sub> N <sub>4</sub> -POMs POMs: [PMo <sup>VI</sup> <sub>12</sub> O <sub>40</sub> ] <sup>3-</sup> , [PW <sup>VI</sup> <sub>12</sub> O <sub>40</sub> ] <sup>3-</sup> , [SiW <sup>VI</sup> <sub>12</sub> O <sub>40</sub> ] <sup>4-</sup>	Keggin	(A) ciprofloxacin	m(catalyst) = 0.01-0.1 g; under visible light	93 % removal within 5 min	1	250
g-C <sub>3</sub> N <sub>4</sub> /H <sub>3</sub> PW <sup>VI</sup> <sub>12</sub> O <sub>40</sub> /TiO <sub>2</sub>	Keggin	(A) tetracycline	m(catalyst) = 20 mg	>70 % removal within 50 min ( <i>k</i> = 0.03443 min <sup>-1</sup> )	1	251
		(P) bisphenol A	m(catalyst) = 20 mg	>38 % removal within 3 hours ( <i>k</i> = 0.00712 min <sup>-1</sup> )	1	
		(IC) Cr(VI)	m(catalyst) = 20 mg	>65 % removal within 60 min ( <i>k</i> = 0.025 min <sup>-1</sup> )	1	
POM-IL, [3-(1-methylimidazolium-3-yl)propane-1-sulfonate] <sub>3</sub> PW <sup>VI</sup> <sub>12</sub> O <sub>40</sub>	Keggin	(Pest) diniconazole	nsp	nsp	1	262
		(Pest) hexaconazole	nsp	nsp	1	
		(Pest) tebuconazole	nsp	nsp	1	
		(Pest) penconazole	nsp	nsp	1	
		(Pest) diniconazole	nsp	nsp	1	
		(Pest) triticonazole	nsp	nsp	1	
biochar-doped g-C <sub>3</sub> N <sub>4</sub> -Co <sub>2</sub> PMo <sub>11</sub> VO <sub>40</sub>	Keggin	(A) sulfamethoxazole	m(catalyst) = 0.2 g/L; under visible light	98.5 % within 20 min ( <i>k</i> = 0.215 min <sup>-1</sup> )	1	273
Ag-L-SiW <sub>12</sub> @BiVO <sub>4</sub> (L = thiacalix [4]arene)	Keggin	(A) ciprofloxacin	pH = 4; v(catalyst) = 30 μL; under simulated solar light	95 % within 240 min ( <i>k</i> = 0.0118 min <sup>-1</sup> )	1	274
H <sub>3</sub> PW <sub>12</sub> O <sub>40</sub> -Fe <sub>3</sub> O <sub>4</sub> -biocar	Keggin	(A) metronidazole	pH = 1; c(catalyst) = 0.6 g/L	>94 % removal within 60 min	1	275
α-K <sub>8</sub> SiW <sub>11</sub> O <sub>39</sub> -MIL-101(Cr)-CoFe <sub>2</sub> O <sub>4</sub>	Lacunary Keggin	(D) methylene blue (D) rhodamine B (D) methyl orange (A) ciprofloxacin	m(catalyst) = 30 mg	methylene blue = 100 % within 25 min rhodamine B = 84 % within 50 min methyl orange = 37 % within 20 min ciprofloxacin = 100 % within 15 min	1	276
EDA-CD-[H <sub>3</sub> PW <sup>VI</sup> <sub>12</sub> O <sub>40</sub> ],	Keggin	(A) nitrofurazone	c(catalyst) = 0.055 mM; under UV irradiation or sunlight; H <sub>2</sub> O <sub>2</sub>	<i>k</i> = 0.163 min <sup>-1</sup>	1	256

(EDA-CD = per-6-deoxy-6-ethylenediamine- $\beta$ -cyclodextrine)		(A) tetracyclines	with H <sub>2</sub> O <sub>2</sub>	$k = 0.152 \text{ min}^{-1}$	1	View Article Online DOI: 10.1039/D5EN00964B
		A) berberine	with H <sub>2</sub> O <sub>2</sub>	$k = 0.115 \text{ min}^{-1}$	1	
		(D) rhodamine B	with H <sub>2</sub> O <sub>2</sub>	$k = 0.868 \text{ min}^{-1}$	1	
		(D) xylene Orange	with H <sub>2</sub> O <sub>2</sub>	$k = 0.214 \text{ min}^{-1}$	1	
		(D) methyl Orange	with H <sub>2</sub> O <sub>2</sub>	$k = 0.164 \text{ min}^{-1}$	1	
		(D) methylene blue	with H <sub>2</sub> O <sub>2</sub>	$k = 0.119 \text{ min}^{-1}$	1	
		(D) crystal violet	with H <sub>2</sub> O <sub>2</sub>	$k = 0.084 \text{ min}^{-1}$	1	
[H <sub>3</sub> PW <sup>VI</sup> <sub>12</sub> O <sub>40</sub> ], @MFM-300(In); MFM-300(In) = indium-based metal-organic framework	Keggin	(A) sulfamethazine (SMT)	nsp	98 % removal within 60 min	1	257
LnTiO <sub>2</sub> /P <sub>2</sub> W <sup>VI</sup> <sub>18</sub> Sn <sub>3</sub>	Keggin	(D) methyl orange	nsp	100 % removal within 5 min	1	270
Na <sub>4</sub> W <sup>VI</sup> <sub>10</sub> O <sub>32</sub>	decatungstate	(Pest) 2-(1-naphthyl)acetamide (NAD)	c(catalyst) = 300 $\mu$ M	89 % removal within 8 hours ( $k = 0.032 \text{ min}^{-1}$ )	1	258
K <sub>2</sub> [V <sup>VO</sup> <sub>10</sub> O <sub>16</sub> (OH) <sub>6</sub> (CH <sub>3</sub> CH <sub>2</sub> CO <sub>2</sub> ) <sub>6</sub> ]	decavanadate	(D) methylene blue	m(catalyst) = 5 mg	93 % removal within 45 min	1	271
Cu(OH <sub>2</sub> ) <sub>3</sub> (2-amp)] <sub>2</sub> (trisH) <sub>2</sub> [V <sup>VO</sup> <sub>10</sub> O <sub>28</sub> ]; 2-amp = 2-aminopyridine, tris = tris(hydroxymethyl)aminomethane	decavanadate	(D) methylene blue	m(catalyst) = 2-10 mg; with H <sub>2</sub> O <sub>2</sub>	93 % removal within 2 min	1	272
Na <sub>10</sub> [Co <sub>4</sub> (H <sub>2</sub> O) <sub>2</sub> (V <sup>VO</sup> <sub>10</sub> O <sub>28</sub> ) <sub>2</sub> ]-34H <sub>2</sub> O	Keggin	(D) methylene blue (D) rhodamine B	c (catalyst) = 10 mg/L	88 % removal within 30 min 88 % removal within 60 min	1	265
NH <sub>4</sub> PW <sup>VI</sup> <sub>12</sub> O <sub>40</sub> (PW) NH <sub>4</sub> PMo <sup>VI</sup> <sub>12</sub> O <sub>40</sub> (PMo)	Keggin	(IC) Ni <sup>2+</sup>	m (catalyst) = 30 mg	72 % removal within 1 min (PW) 90 % removal within 1 min (PMo)	1	269
		(D) tetracycline	m (catalyst) = 30 mg	71 % removal within 30 min (PW) 92 % removal within 30 min (PMo)		
$\alpha$ -H <sub>3</sub> PW <sup>VI</sup> <sub>12</sub> O <sub>40</sub> ·6H <sub>2</sub> O $\alpha$ -H <sub>3</sub> PMo <sup>VI</sup> <sub>12</sub> O <sub>40</sub> ·14H <sub>2</sub> O	Keggin	(D) methylene blue (D) rhodamine B (D) crystal violet (D) methyl orange (D) sunset yellow	m (catalyst) = 5 mg	>90 % removal for all dyes within 30 min	1	277

## 4 Polyoxometalates in air pollution

Various POMs alone and in combination with other compounds<sup>117,278</sup>, such as MOFs, CNTs and mesoporous silica supports, have shown promising results in the removal of air pollutants, such as refractory sulfur compounds<sup>279</sup> from fossil fuels (Section 4.1), toxic gases such as hydrogen sulfide<sup>116</sup> (Section 4.2.1), nitrogen oxides and sulfur dioxide<sup>280</sup> (Section 4.2.2) and carcinogenic volatile organic compounds (VOCs; Section 4.3) present in indoor and outdoor air.<sup>281,282</sup>

Among POM archetypes, Keggin-type structures dominate air purification applications due to their high catalytic activity, particularly in the oxidative desulfurization of refractory sulfur compounds from fossil fuels under mild conditions<sup>61</sup> (~85 % of the reported literature; **Table S1**). Anderson-Evans POMs also contribute effectively to the desulfurization of fossil fuels by showing promising desulfurization performance through alkyl peroxide formation mechanisms with extended catalyst lifetimes.<sup>283,284</sup> Wells-Dawson-type POMs, especially when doped with lanthanide ions, exhibit enhanced regeneration and stability, making them effective for toxic gas removal (Section 4.2; Table 2), such as H<sub>2</sub>S, NO<sub>x</sub>, and SO<sub>2</sub>. Their tunable redox states and structural differences tailor their catalytic behavior, with rare-earth-doped Wells-Dawson POMs<sup>116</sup> showing superior H<sub>2</sub>S oxidation and the photocatalytic activity of Keggin/g-C<sub>3</sub>N<sub>4</sub> composites enabling efficient VOC removal under visible light.<sup>285,286</sup> These reported examples of using different POM structures highlight the unique functions and advantages that structural diversity in POM chemistry provides for air pollutant remediation.<sup>116,282,283,248,285</sup>

### 4.1 Removal of refractory sulfur compounds from fossil fuels

The governments worldwide have introduced stricter regulations and restrictions on the amount of sulfur in fuels to ultra-low levels (< 10 ppm).<sup>53</sup> Therefore, the main goal of industry and science is to find a way to make the fuel desulfurization method efficient, inexpensive, clean, and safe.<sup>52,53</sup> Currently, the established industrial standard for fossil fuel desulfurization is hydrodesulfurization (HDS). The HDS method has proven itself to be very effective in removing thiols, inorganic sulfides, and disulfides. However, due to new regulations requiring ultra-low sulfur fuels<sup>53</sup>, HDS is insufficiently effective for removing the more difficult-to-remove refractory sulfur compounds. Moreover, HDS is a very expensive method and operates under harsh reaction conditions of 300–400 °C and 30–100 bar H<sub>2</sub> pressure. In contrast, POM-based oxidative desulfurization (ODS) operates under mild conditions (rt–100 °C, atmospheric pressure, H<sub>2</sub>O<sub>2</sub>/O<sub>2</sub> (**Table S1**)). POMs provide competitive advantages for the needed ultra-low sulfur fuels (< 10 ppm)<sup>53</sup> through their reversible multi-electron redox capability, oxygen-rich surfaces, and high catalytic stability. This eliminates high-pressure H<sub>2</sub> handling and reduces energy demands for heating and compression.<sup>52,61</sup> ODS-based systems achieve 84–98 % sulfur conversion from 3.5 wt % to < 0.5 wt % with 55.57 % energy efficiency, demonstrating superior energy utilization for refractory sulfur compounds like DBTs.<sup>287</sup> Electrochemical

regeneration (H<sub>2</sub>O<sub>2</sub>/O<sub>2</sub>) further enhances POM recyclability (in most reported literature: > 95 % recovery, and 10<sup>4</sup> cycles, **Table S1**). These data show that the ODS system is more energy cost-efficient for deep desulfurization than HDS.<sup>287,288</sup>

He *et al.* reported a series of Keggin-type K<sub>x</sub>[PMo<sup>VI</sup><sub>12</sub>O<sub>40</sub>] (K<sub>x</sub>PMo, x = 1, 2, 3, 4) polyoxometalate salts prepared by hydrothermal synthesis using commercial F127 templates (Pluronic F127). The prepared K<sub>x</sub>PMo salts (**Figure 15.A**) were mesoporous with a high surface area (> 40 m<sup>2</sup> g<sup>-1</sup>) and could be successfully utilized for complete ODS of model oil in 1 h. By comparing the catalytic activity of the prepared POM salts, K<sub>4</sub>PMo showed the highest activity in the ODS process with a DBT removal rate of 99.5 % within 60 minutes (**Table S1** in Supporting Information, k = 0.076 min<sup>-1</sup>). A reaction mechanism of DBT oxidation by the K<sub>4</sub>PMo/H<sub>2</sub>O<sub>2</sub> catalytic system has been proposed (**Figure 15.B**).<sup>289</sup> In addition, the K<sub>4</sub>PMo catalyst also showed activity for the removal of other refractory sulfur compounds, DMDBT and BT, with removal efficiencies of 99.0 % and 60.3 %, respectively. The authors concluded that the ODS activity of K<sub>x</sub>PMo catalysts has a linear correlation with their electrochemically active surface area (ECSA). The higher activity of the K<sub>4</sub>Mo catalyst can therefore be attributed to its largest ECSA value, which shows that K<sub>4</sub>PMo exposes the largest number of anions [PMo<sup>VI</sup><sub>12</sub>O<sub>40</sub>]<sup>3-</sup> among all prepared catalysts. XRD structural analysis confirmed the good structural stability and successful recovery of the K<sub>4</sub>PMo catalyst that was used.<sup>289</sup>

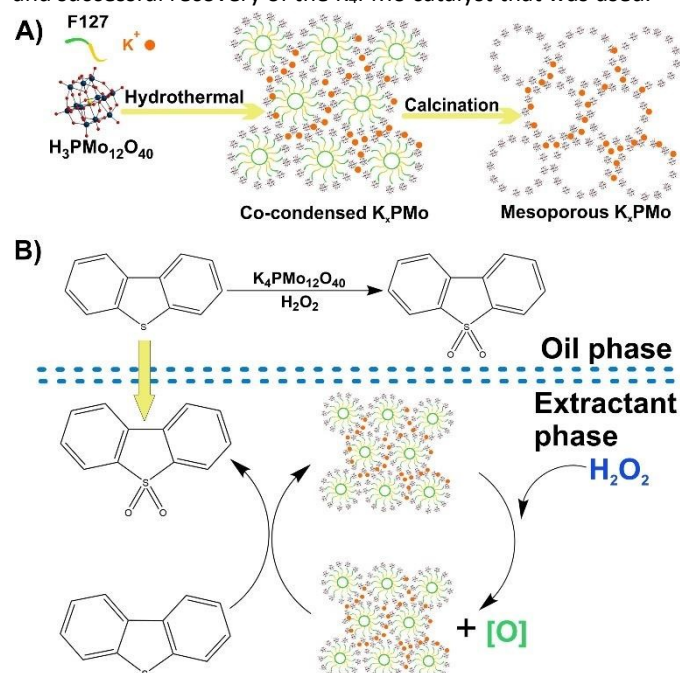


**Figure 15.** A) Illustration of one-pot hydrothermal synthesis of mesoporous K<sub>x</sub>PMo material. The resulting K<sub>x</sub>PMo material was highly crystalline with uniform and spherical morphology. It is denoted as K<sub>x</sub>PMo, where x denotes the amount of HPMO added to the initial mixture. B) A schematic representation of the DBT oxidation mechanism in the presence of H<sub>2</sub>O<sub>2</sub> catalysed by K<sub>x</sub>PMo. DBT preferentially resides in the biphasic system's oil phase (n-octane), whereas the H<sub>2</sub>O<sub>2</sub> oxidant and K<sub>x</sub>PMo catalyst primarily reside in the extractant phase (methanol). Therefore, the first step is to extract into the extractant phase to react with H<sub>2</sub>O<sub>2</sub> in the presence of K<sub>x</sub>PMo.<sup>289</sup>

Besides commonly utilized Keggin-type POMs, other archetypes, especially Anderson-Evans and Wells-Dawson, have also been used in the ODS process. Eseva *et al.* prepared a series of Anderson-type polyoxometalates (**Figure 16**),



( $\text{NR}_4$ )<sub>3</sub>[ $\text{X}^{\text{III}}\text{Mo}^{\text{VI}}_6\text{O}_{24}\text{H}_6$ ] ( $\text{X}^{\text{III}} = \text{Cr, Fe, Co; R} = \text{H or alkyl}$ ), and tested their catalytic properties in the ODS process of model fuel. The Co(III)-based Anderson type POM exhibited the highest catalytic activity in the desulfurization of model diesel with a 100 % conversion rate of DBT within 60 minutes with a molar ratio of  $n(\text{S}):n(\text{cat.}) = 50:1$  (Table S1 in Supporting Information). By prolonging the reaction time to 120 min, 100 % conversion was also achieved for BT. However, for 3-methylbenzene, only 59 % conversion was achieved in 4 h.<sup>283</sup> A reaction mechanism for DBT oxidation by the Co(III)-POM has been proposed (Figure 16). The crucial oxidation step in the catalytic system is based on the oxidation of a solvent (decalin), with the formation of an alkyl peroxide as the active species. Alkyl peroxide formation occurs by the reaction with an  $\text{O}_2$  molecule from the air in the presence of a Co(III)-POM to form alkyl peroxides and the subsequent formation of the polyoxometalate's metal-dioxo species, as the source of active oxygen in the further oxidation of DBT. The quaternary ammonium cation in the ( $\text{NR}_4$ )<sub>3</sub>[ $\text{X}^{\text{III}}\text{Mo}^{\text{VI}}_6\text{O}_{24}\text{H}_6$ ] catalyst structure allows the catalyst to adsorb the substrate molecules (DBT) and coordinate with the sulfur atom, after which the coordinated DBT is oxidized to a sulfone, thus simultaneously reducing ( $\text{NR}_4$ )<sub>3</sub>[ $\text{Co}^{\text{III}}\text{Mo}^{\text{VI}}_6\text{O}_{24}\text{H}_6$ ] POM. The reduced form of ( $\text{NR}_4$ )<sub>3</sub>[ $\text{Co}^{\text{III}}\text{Mo}^{\text{VI}}_6\text{O}_{24}\text{H}_6$ ] POM is re-oxidized with a new peroxide molecule, and a new catalytic cycle is started.<sup>283</sup>

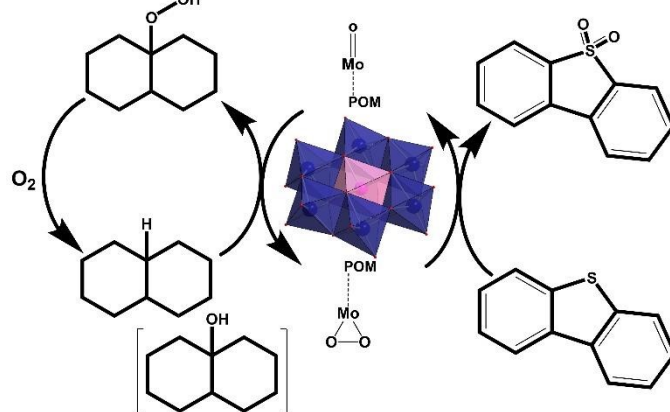


Figure 16. A schematic representation of DBT oxidation mechanism catalyzed by Anderson-type polyoxometalates ( $(\text{NR}_4)_3[\text{X}^{\text{III}}\text{Mo}^{\text{VI}}_6\text{O}_{24}\text{H}_6]$  ( $\text{X} = \text{Cr, Fe, Co; R} = \text{H or alkyl}$ ) in the presence of  $\text{O}_2$  from air.<sup>283</sup>

Hybrid POM-based materials have also been researched and have shown promising results as catalysts in ODS processes. Chi *et al.* reported the preparation of a new biomimetic catalytic system consisting of an Anderson-type POM ( $[\text{Na}_3\text{H}_6\text{Cr}^{\text{III}}\text{Mo}^{\text{VI}}_6\text{O}_{24}]$ ) and deep eutectic solvents (DESs) and its successful application as a catalyst for the removal of sulfur compounds from both model and commercial diesel.<sup>284</sup> Six different DESs (PEG/PAS, PEG/SSA, PEG/SA, PEG/DHBA, PEG/PXA and PEG/DL-MA) were combined with  $\text{CrMo}_6$  (Figure 17), and their activity was tested. Only the addition of PEG/SSA, DES, containing an  $-\text{SO}_3\text{H}$  group, resulted in 100% sulfur removal, while utilizing other DESs resulted in no higher than 30 % sulfur removal.<sup>284</sup> The desulfurization process followed the extraction-oxidation mechanism in which the POM and the DES acted as the electron transfer mediators and were both crucial for the process (Figure 17).<sup>284</sup>



Figure 17. Schematic representation of the reaction mechanism for the oxidation desulfurization of DBT catalyzed by coupling  $\text{CrMo}_6$  polyoxometalate with DESs under mild conditions ( $T = 60^\circ\text{C}$ ).<sup>284</sup>

Ye *et al.* designed a new porous POM-based hybrid material by encapsulating a Keggin-type polyoxometalate [ $\text{H}_3\text{PW}^{\text{VI}}_{12}\text{O}_{40}$ ] (PW) in the metal-organic framework UiO-66(Zr) and employed it as a catalyst in the ODS reaction of BT, DBT, and DMDBT at room temperature, with 98.2 % DBT removal efficiency.<sup>290</sup> A proposed reaction mechanism includes the extraction of DBT molecules from the model oil into the acetonitrile phase by the POM catalyst and  $\text{H}_2\text{O}_2$ . After extraction, DBT and  $\text{H}_2\text{O}_2$  can be adsorbed into the catalyst pores, leading to the formation of  $\bullet\text{OH}$  radicals via electron transfer from Zr-OH<sub>2</sub> active centers in UiO-66 (Zr). Another  $\text{H}_2\text{O}_2$  molecule can react with a W(VI) metal ion in the [ $\text{H}_3\text{PW}^{\text{VI}}_{12}\text{O}_{40}$ ] POM to form the W(VI)-peroxy species that lead to the formation of  $\text{O}_2^{\bullet-}$  radicals. Both  $\text{O}_2^{\bullet-}$  and  $\bullet\text{OH}$  radicals can oxidize DBT to DBTO<sub>2</sub>. The existence of two types of active centers in the catalyst, W(VI) in [ $\text{H}_3\text{PW}^{\text{VI}}_{12}\text{O}_{40}$ ] and Zr-OH<sub>2</sub> in UiO-66 (Zr), which forms two different active species, is probably responsible for the high efficiency of the catalyst in the ODS process.<sup>290</sup>

For the desulfurization of fossil fuels, Gao *et al.* prepared a series of Wells-Dawson-type POMs [ $\text{H}_{6+n}\text{P}_2\text{Mo}^{\text{VI}}_{18-n}\text{V}_n\text{O}_{62}\text{-mH}_2\text{O}$ ] ( $n = 1-5$ ;  $\text{Mo}_{17}\text{V}_1$ ,  $\text{Mo}_{16}\text{V}_2$ ,  $\text{Mo}_{15}\text{V}_3$ ,  $\text{Mo}_{14}\text{V}_4$ , and  $\text{Mo}_{13}\text{V}_5$ ), immobilized them on CNT carriers, and thereby prepared two different types of catalysts, CNT@PDDA@POM and POM@CNT.<sup>291</sup> All prepared POM-based materials have shown to be catalytically active in the ODS process. CNT@PDDA@ $\text{Mo}_{16}\text{V}_2$  showed the highest catalytic activity with 99.4 % desulfurization efficiency. The better efficiency of this type of catalyst was due to a different POM position in CNT@PDDA@POM (on the surface of CNT@PDDA) compared to POM@CNT (deep in the CNTs' channel). Moreover, it was observed that the number of Mo centers replaced with V centers affects the efficiency, with a 16:2 ratio being the optimal Mo:V ratio for obtaining a high desulfurization activity of both catalysts. By combining CNT carriers with high mechanical properties, high thermal stability, and a high specific surface area, Gao *et al.* overcame disadvantages such as a low specific surface area and the difficulty of reclamation for pure POMs.<sup>291</sup> More literature-known POM-based catalysts and their



efficiency in the removal of refractory compounds from fossil fuels are summarized in **Table S1** in the Supporting Information.

## 4.2 Removal of toxic gases - H<sub>2</sub>S, NO<sub>x</sub> and SO<sub>2</sub>

**4.2.1 Hydrogen sulfide (H<sub>2</sub>S) in air pollution.** Hydrogen sulfide is naturally present in crude petroleum, natural gas, volcanic gases, and geothermal sources. It is also a common by-product of many human activities, such as wastewater treatment<sup>292</sup>, fossil fuel combustion<sup>54</sup>, sewage treatment facilities<sup>55</sup>, paper factories<sup>56</sup>, food processing factories, and agriculture.<sup>57</sup> Hydrogen sulfide is an odorous toxic gas with a corrosive nature and an adverse effect on human health and directly affects industrial production by reducing industrial catalysts' efficiency and causing equipment failure. It can also easily oxidize and form SO<sub>2</sub> gas (**Eq. 1**), one of the leading causes of acid rain:<sup>58</sup>



Furthermore, hydrogen sulfide readily reacts with metals, such as copper, and forms the corresponding sulfides (Cu<sub>2</sub>S) on the surface of electrical devices, causing electrical failures. H<sub>2</sub>S can also cause corrosion on surfaces, which can cause damage to buildings, for example, sewage plant facilities.<sup>293</sup> In addition to SO<sub>2</sub> (Section 4.2.2), H<sub>2</sub>S can react with different compounds present in the atmosphere and form many other toxic by-products, such as carbonyl sulfides (**Eq. 2**), carbon disulfides (**Eq. 3**), sulfurous acid (**Eq. 4**), and PMs, that have been linked to ozone layer depletion:<sup>294</sup>



Scientists and engineers have developed different methods for removing H<sub>2</sub>S from the environment, such as metal oxide oxidation<sup>295</sup>, adsorption using different adsorbents (activated carbon or wet scrubbing)<sup>296</sup>, the Claus process<sup>297</sup>, biofiltration, oxidative desulfurization, and the LRSR process<sup>298</sup>. The latter two methods are recently the most commonly used methods with a very high desulfurization capacity and efficient production of elemental sulfur using various redox mediators (e.g., Fe(III)/Fe(II)).<sup>298</sup> Such mediators have shown outstanding results, but they are still mostly chemically unstable and require low pH, which is unfavorable for H<sub>2</sub>S removal processes.

POMs and different POM-based hybrid materials have shown high efficiency in H<sub>2</sub>S removal due to their redox properties and structural stability. For the regeneration of these POM-based catalysts, a redox-mediated electrochemical regeneration method using oxidants such as H<sub>2</sub>O<sub>2</sub> or O<sub>2</sub> has recently been shown to be effective.<sup>280</sup>

A purely inorganic POM was applied by Pei *et al.* who successfully synthesized a set of rare-earth Dawson-type polyoxometalates (K<sub>17</sub>[Pr<sup>III</sup>(P<sub>2</sub>Mo<sup>VI</sup><sub>17</sub>O<sub>61</sub>)<sub>2</sub>] (PrPMo), K<sub>17</sub>[Gd<sup>III</sup>(P<sub>2</sub>Mo<sup>VI</sup><sub>17</sub>O<sub>61</sub>)<sub>2</sub>] (GdPMo), K<sub>17</sub>[Sm<sup>III</sup>(P<sub>2</sub>Mo<sup>VI</sup><sub>17</sub>O<sub>61</sub>)<sub>2</sub>] (SmPMo) and K<sub>17</sub>[Eu<sup>III</sup>(P<sub>2</sub>Mo<sup>VI</sup><sub>17</sub>O<sub>61</sub>)<sub>2</sub>] (EuPMo)) and utilized them in the removal of H<sub>2</sub>S. Due to the excellent redox

properties of Ln(III)-doped POMs, the influence of different Ln(III) species on H<sub>2</sub>S removal was investigated. From the experimental results, the prepared compounds were ranked according to their efficiency for the removal of H<sub>2</sub>S in the following order: PrPMo (90 %) > EuPMo (88 %) > SmPMo (87 %) > GdPMo (85 %). The PrPMo polyoxometalate showed the best desulfurization and regeneration properties with 90 % efficiency at 25 °C within 400 min. The XPS spectral analysis showed that H<sub>2</sub>S is first oxidized to S by a redox reaction with PrPMo, in which Mo(VI) is simultaneously reduced to Mo(IV). During the electrochemical regeneration of PrPMo, S is further oxidized to SO<sub>4</sub><sup>2-</sup> as the main desulfurization product, and Pr(IV) is reduced to Pr(III) during the regeneration process. The results of repeated XPS measurements confirmed the successful regeneration of PrPMo.<sup>116</sup>

Ma *et al.* described a new approach for an H<sub>2</sub>S oxidation and sulfur recovery system using the hybrid POM-based hybrid materials, [C<sub>4</sub>mim]<sub>3</sub>PMo<sup>VI</sup><sub>12</sub>O<sub>40</sub>-ILs ([C<sub>4</sub>mim]<sup>+</sup> = 1-butyl-3-methylimidazolium cation), where they investigated the influence of several different [C<sub>4</sub>mim]<sup>+</sup>-based ionic liquids (ILs), [C<sub>4</sub>mim]Cl, [C<sub>4</sub>mim]BF<sub>4</sub>, [C<sub>4</sub>mim]PF<sub>6</sub> and [C<sub>4</sub>mim]NTf<sub>2</sub>. Of all the POM-IL systems tested, the [C<sub>4</sub>mim]<sub>3</sub>PMo<sup>VI</sup><sub>12</sub>O<sub>40</sub>-[C<sub>4</sub>mim]Cl system has shown to be the most effective for removing H<sub>2</sub>S, with 100 % efficiency. The adsorption mechanism of H<sub>2</sub>S desulfurization is explained by the theory of cavities and the strong interaction between H<sub>2</sub>S and Cl<sup>-</sup>. Additionally, they confirmed that the POM-IL material could be successfully recovered more than six times without losing its efficiency.<sup>299</sup>

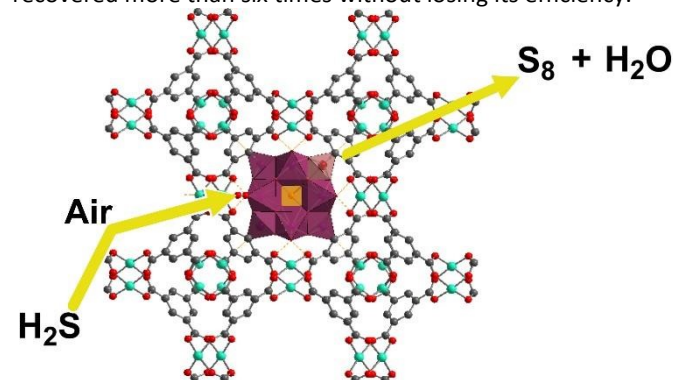


**Figure 18.** Crystal structure of POM-MOF ( $\{[(\text{CH}_3)_4\text{N}]_4\text{CuPW}_{11}\text{O}_{39}\text{H}\}$ ) material. The  $[\text{CuPW}_{11}\text{O}_{39}]^{5-}$  polyhedra are orientationally disordered into the pores. It was concluded that the catalytic decomposition of H<sub>2</sub>S was taking place inside the pores.<sup>300</sup>

Song *et al.* prepared a POM-based metal-organic framework  $\{[(\text{CH}_3)_4\text{N}]_4\text{CuPW}_{11}\text{O}_{39}\text{H}\}$  (POM-MOF) hybrid material (**Figure 18**) by combining a Keggin-type polyoxometalate  $[\text{CuPW}_{11}\text{O}_{39}]^{5-}$  and MOF-199.<sup>300</sup> The POM-MOF/O<sub>2</sub> catalytic system effectively oxidizes H<sub>2</sub>S to solid S<sub>8</sub> with up to 95 % H<sub>2</sub>S removal efficiency. Additionally, it has been shown that the POM-MOF system can successfully oxidize mercaptans to disulfides. The POM-MOF catalyst can be successfully reused in the oxidation process after simple filtration, washing, and drying. The UV-VIS and FT-IR spectra showed that the  $[\text{CuPW}_{11}\text{O}_{39}]^{5-}$  structure was preserved in the POM-MOF catalyst at pH 11 for at least 12 h. The POM-MOF hybrid material showed better stability and pH resistance than the  $[\text{CuPW}_{11}\text{O}_{39}]^{5-}$  POM alone.<sup>300</sup>

A summary of literature-reported POMs and POM-based hybrid materials and their efficiencies in H<sub>2</sub>S removal are given in **Table 2** at the end of Section 4.

**4.2.2 Nitrogen oxides (NO<sub>x</sub>) and sulfur dioxide SO<sub>2</sub> in air pollution.** Interest in NO<sub>x</sub> emissions and their regulation began after 1952 with the confirmation of their role in the formation of photochemical smog.<sup>301</sup> Several different nitrogen oxides are present in the atmosphere, e.g., N<sub>2</sub>O, NO, NO<sub>2</sub>, N<sub>2</sub>O<sub>3</sub>, N<sub>2</sub>O<sub>4</sub>, NO<sub>3</sub>, and N<sub>2</sub>O<sub>5</sub>. However, NO<sub>x</sub> mainly refers to NO and NO<sub>2</sub> oxides because nitrogen oxides are primarily released into the environment in these forms, and NO<sub>x</sub> emissions contain 95 % NO and 5 % NO<sub>2</sub>.<sup>302</sup> NO is considered less toxic than NO<sub>2</sub> and can cause eye irritation, but NO<sub>2</sub>, even at low concentrations, can cause acute lung injury with pneumonitis<sup>303</sup> and fulminant pulmonary edema.<sup>304</sup> In urban areas where a higher concentration of NO<sub>2</sub> gas present, many respiratory and cardiovascular diseases and even increased mortality among the exposed population have been observed.<sup>303,305</sup>

Moreover, H<sub>2</sub>S and NO<sub>x</sub> gases are considered to be among the major air pollutants because they are thought to be responsible for various environmental issues, such as photochemical smog, acid rain<sup>306</sup>, tropospheric ozone<sup>307</sup>, ozone layer depletion, and even global warming, as a result of N<sub>2</sub>O.<sup>308,309</sup> NO<sub>x</sub> gases are also associated with the greenhouse effect, and in the higher layers of the atmosphere, they can react with various compounds present there (O<sub>3</sub>, VOCs, etc.), leading to ozone depletion. Most air pollution occurs and remains within the lowest layer of the atmosphere, the troposphere. NO<sub>x</sub> gases can lead to the formation of tropospheric ozone after photochemical degradation to NO (**Eq. 5**):



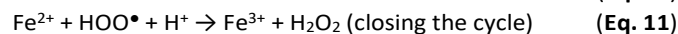
With NO not absorbing radiation above 230 nm and thus not acting as an inhibitor in the lower atmosphere, the resulting atomic oxygen reacts with O<sub>2</sub> in the troposphere to form ozone (**Eq. 6**), leading to the tropospheric ozone formation.<sup>301,307</sup> Great efforts have been made to develop methods for removing NO<sub>x</sub> from the atmosphere in the last few decades.<sup>306,310,311</sup> Adsorptive-desorption methods<sup>307,309</sup> and Fenton-like reactions<sup>285</sup>, as examples of AOPs, have been extensively studied for the removal of NO<sub>x</sub> and SO<sub>2</sub> gases. The Fenton-like oxidation process consists of oxidation and degradation of different pollutants in the presence of a catalyst and H<sub>2</sub>O<sub>2</sub> as an oxidant activated by UV-light irradiation.<sup>280,311</sup>

In the oxidation process, the generated reactive •OH radicals (**Eq. 7**) oxidize a wide range of different substrates. Such radical-assisted oxidation processes have been shown to be particularly effective in removing organic dyes, phenols, antibiotics, and insecticides from wastewater and are a popular research topic for pollution removal applications.<sup>212</sup>

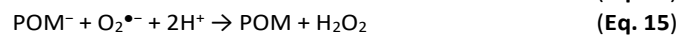
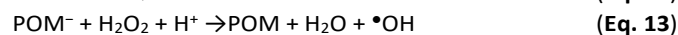


Zhao *et al.*<sup>312</sup> reported the synthesis of an iron-substituted Keggin-type polyoxometalate-based catalyst Fe<sup>III</sup>AspPW from

ferric chloride (FeCl<sub>3</sub>), aspartic acid (Asp), and phosphotungstic acid ([H<sub>3</sub>PW<sup>VI</sup><sub>12</sub>O<sub>40</sub>]). The Fe<sup>III</sup>AspPW was used to activate H<sub>2</sub>O<sub>2</sub> to form active •OH species, which are crucial for the removal of NO from flue gas. The proposed catalytic mechanism consists of two redox cycles that occur on the surface of the Fe<sup>III</sup>AspPW catalyst: the redox cycles of Fe<sup>III</sup> ↔ Fe<sup>II</sup> and POM ↔ POM<sup>-</sup>. In the Fenton-like process, first, in the redox cycle of Fe<sup>III</sup> ↔ Fe<sup>II</sup>, Fe<sup>3+</sup> reacts with H<sub>2</sub>O<sub>2</sub> to first form HOO• (**Eq. 8**) and then •OH (**Eq. 9**) active species:



In the POM ↔ POM<sup>-</sup> redox cycle, the POM component is firstly reduced to the POM<sup>-</sup> form in a reversible reaction, and then the reduced POM<sup>-</sup> form further reacts with H<sub>2</sub>O<sub>2</sub> to form active •OH species (**Eq. 13**). In addition, to close the redox cycle, POM<sup>-</sup> is oxidized by O<sub>2</sub> or O<sub>2</sub><sup>•-</sup>:



This catalytic system showed great activity for removing NO with 94.6 % efficiency.<sup>312</sup> Moreover, Liu *et al.* showed that the Fe<sup>III</sup>AspPW/H<sub>2</sub>O<sub>2</sub> catalytic system could also be used to simultaneously remove SO<sub>2</sub> and NO from flue gas in a UV-Fenton-like process with efficiencies of the Fe<sup>III</sup>AspPW catalyst of 100 % for SO<sub>2</sub> removal and 84.27 % for NO removal.<sup>312</sup> Wang *et al.* presented a series of Ge(IV)-based Keggin-type polyoxometalates ([H<sub>4</sub>GeW<sup>VI</sup><sub>12</sub>O<sub>40</sub>] (HGeW), [H<sub>5</sub>GeW<sup>VI</sup><sub>11</sub>V<sup>VO</sup><sub>40</sub>] (HGeWV), [H<sub>5</sub>GeMo<sup>VI</sup><sub>11</sub>V<sup>VO</sup><sub>40</sub>] (HGeMoV), [H<sub>5</sub>GeW<sup>VI</sup><sub>9</sub>Mo<sup>VI</sup><sub>2</sub>V<sup>VO</sup><sub>40</sub>] (HGeWMoV)) and utilized them in the removal of NO<sub>x</sub> pollutants.<sup>313</sup> The adsorption-desorption experiments showed the following adsorption efficiencies for the removal of NO<sub>x</sub> gases: HGeW (81.5 %) > HGeWV (74 %) > HGeWMoV (67 %) > HGeMoV (52 %). The Keggin-type polyoxometalate HGeW (**Figure 2.E**) showed the highest NO<sub>x</sub> removal activity with 81.5 % removal and 68.3 % N<sub>2</sub> selectivity, of which 65% was from fractionated NO and 35 % NO<sub>2</sub> gas. Additionally, the H<sub>2</sub>S removal efficiency of HGeW was compared with that of the parent Keggin [H<sub>3</sub>PW<sup>VI</sup><sub>12</sub>O<sub>40</sub>] (HPW) polyoxometalate (54.1 % efficiency). The FT-IR studies revealed that NO<sub>x</sub> is adsorbed on HGeW mainly in the form of NOH<sup>+</sup> and NO• species, but on the HPW, only NOH<sup>+</sup> is observed as the main form during adsorption. Moreover, TPD-MS experiments were carried out to investigate the further decomposition mechanism of NO<sub>x</sub> over HGeW and HPW. The TPD-MS analysis showed that while the decomposition products (NO, N<sub>2</sub>O, N<sub>2</sub>, and O<sub>2</sub>) appear in the same order for both HPW and HGeW, they appear at different temperatures, lower in the case of HPW. The NO species appeared at the lowest temperature for both NO<sub>x</sub> decomposition experiments. It is believed that a significant part of the NO<sub>x</sub> is physically adsorbed onto HPW and HGeW in the



form of NO at a lower temperature. Meanwhile, the later appearing N<sub>2</sub>O could be a product of the disproportionation reaction of NO in which N<sub>2</sub> is formed because of the bonding effect of N-atom, which comes from N-O bond breakage. The difference in NO<sub>x</sub> removal efficiency and N<sub>2</sub> selectivity between HPW and HGeW could be due to the HGeW's ability to intensively loosen the N-O bond, resulting in easier NO<sub>x</sub> decomposition, and by better NO<sub>x</sub> adsorption for HGeW in the form of both NO• and NOH<sup>+</sup>. It is believed that the presence of the Ge(IV) atom instead of P as the central atom plays a significant role in the processes described above.<sup>313</sup>

#### 4.3 Volatile organic compounds in air pollution (VOCs)

##### 4.3.1 Removal of volatile organic compounds - refractory BETX compounds (benzene, ethylbenzene, toluene, and xylenes).

VOCs are a group of liquid organic compounds that can easily evaporate at room temperature. In addition to their volatility, this group of compounds has variable lipophilicity, small molecular size, and are uncharged, resulting in inhalation as the primary route of human exposure.<sup>314</sup> VOCs are classified according to molecular structure and functional groups and include aliphatic hydrocarbons, aromatic hydrocarbons, alcohols, ethers, esters, aldehydes, etc. Due to their properties and wide application in different areas of everyday life, they are common indoor and outdoor air pollutants.<sup>314,285</sup> As outdoor pollutants, they result from the development of industry and urbanization, which involves the increased use of fossil fuels in transport, industrial production, and wastewater treatment plants. As indoor air pollutants, VOCs are found in tobacco smoke, various air fresheners and perfumes, paints and coatings, cleaning products, etc., and can be harmful to human health at excessive concentrations.<sup>285,286,314</sup> Especially, the group of so-called refractory BETX compounds, which stands for benzene, ethylbenzene, toluene, and xylenes, is problematic due to their high toxicity and confirmed carcinogenic nature.<sup>285,314</sup> Besides being confirmed carcinogens, depending on the concentration and length of exposure, various consequences of VOCs exposure have been reported: eye and respiratory tract irritation, headache, dizziness, allergic skin reaction, fatigue, memory impairment, loss of consciousness, and even death.<sup>286,315,316</sup>

Various methods<sup>314</sup> have been studied in search of an efficient and affordable method for removing volatile organic compounds (VOCs) from the air, such as condensation, adsorption<sup>317,318</sup>, and (photo)catalytic oxidation.<sup>314</sup> Photocatalytic oxidation (PCO) is a promising method for removing VOCs from the air, and so far, TiO<sub>2</sub>-based photocatalytic oxidation<sup>318</sup> has mainly been investigated. Due to the tendency to develop a sunlight/visible-light-driven method, TiO<sub>2</sub> has been shown to be a non-ideal photocatalyst due to its poor solar energy utilization.<sup>320</sup> Therefore, there is a need to design new materials that could be successfully applied as photocatalysts for VOCs' photocatalytic oxidation.<sup>315,321</sup>

Meng *et al.* have shown that photoactive PW<sub>12</sub>/g-C<sub>3</sub>N<sub>4</sub> optical films (Figure 19.B) can be obtained by combining the Keggin-

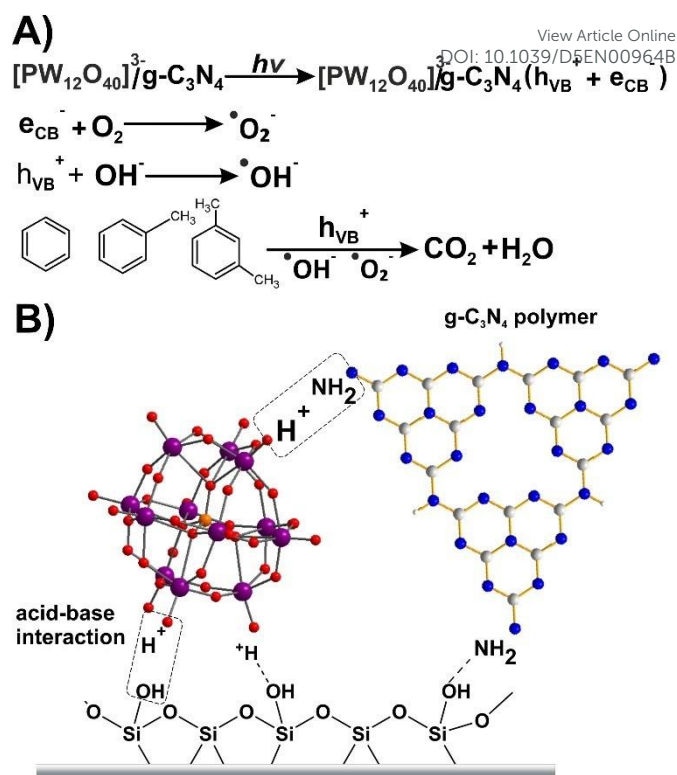


**Figure 19.** A) Reaction mechanism of photocatalytic oxidation of VOCs catalysed by PW<sub>12</sub>/g-C<sub>3</sub>N<sub>4</sub> films. B) Schematic representation of the preparation of PW<sub>12</sub>/g-C<sub>3</sub>N<sub>4</sub> catalyst and its framework structure.<sup>286</sup>

type POM, [H<sub>3</sub>PW<sup>VI</sup><sub>12</sub>O<sub>40</sub>], with polymeric graphitic carbon nitride (g-C<sub>3</sub>N<sub>4</sub>) and then successfully utilized them as photocatalysts for the efficient removal of benzene, toluene, and *m*-xylene. The PW<sub>12</sub>/g-C<sub>3</sub>N<sub>4</sub> optical films showed excellent removal efficiencies for benzene (90.3 %), toluene (100 %) and *m*-xylene (97.5 %). They also demonstrated excellent stability and reusability for up to 30 cycles without signs of activity loss. The results of DMPO spin-trapping ESR measurements indicated that the PW<sub>12</sub>/g-C<sub>3</sub>N<sub>4</sub> films follow a simulated sunlight-driven direct Z-scheme-dictated charge carrier transformation mechanism that accelerates interfacial charge carrier separation and the formation of O<sub>2</sub><sup>-•</sup> and HO• radicals that are involved in VOCs oxidation. In the suggested mechanism (Figure 19.A), charge separation and formation of e<sub>CB</sub><sup>-</sup>-h<sub>VB</sub><sup>+</sup> pair occur (photocurrent), resulting in the formation of O<sub>2</sub><sup>-•</sup> and HO• active species that directly participate in the complete mineralization of VOCs to CO<sub>2</sub> and H<sub>2</sub>O (Figure 19.A).<sup>286</sup> Also, Gamelas *et al.* presented a series of new cellulose/silica hybrid composites functionalized with different Keggin-type POMs ([PV<sub>2</sub>Mo<sup>VI</sup><sub>10</sub>O<sub>40</sub>]<sup>5-</sup>, [PV<sup>VI</sup>Mo<sup>VI</sup><sub>11</sub>O<sub>40</sub>]<sup>4-</sup>, [PMo<sup>VI</sup><sub>12</sub>O<sub>40</sub>]<sup>3-</sup> and [PW<sup>VI</sup><sub>12</sub>O<sub>40</sub>]<sup>3-</sup>) and investigated their potential application in the catalytic oxidation of VOCs present in urban air.<sup>281</sup> The new cellulose/silica hybrid materials were composed of approximately 56 wt % of polysaccharides, ca. 37 wt % of propylamine-modified silica, 2 wt % of POM, and 5 wt % of hydration water. Catalytic activity experiments were performed by pumping polluted air through Teflon tubes filled with the catalysts and then analyzing the treated air by GC-chromatography.



The catalytic activity of the new POM-based hybrid material for VOCs oxidation was visible as a change in the color of the material from yellow to green, indicating the occurrence of  $V(V) \rightarrow V(IV)$  reduction in the POM. The GC-chromatography of a real air sample treated with the new hybrid material indicated complete oxidation of most  $C_5$ - $C_{11}$  volatile organic compounds. The successful recovery of the used catalyst was achieved by passing purified air through the Teflon tubes filled with used catalyst, which was noticeable by the color change of the material from green to yellow.<sup>281</sup>

POMs have also proven as suitable adsorbents for adsorption techniques to remove VOCs from the air. Ma *et al.* reported a newly synthesized POM/MOF hybrid material,  $K_2[Cu_{12}(BTC)_8 \cdot 12H_2O][HPW^{VI}_{12}O_{40}] \cdot 28H_2O$  or NENU-28 and its possible application as an adsorbent for the adsorption of VOCs, including short-chain alcohols (MeOH and EtOH), cyclohexane, benzene, and toluene.<sup>322</sup> The adsorption capacity of NENU-28 for methanol, ethanol, 1-propanol, 2-propanol, cyclohexane, benzene and toluene was tested in VOCs adsorption experiments. The adsorption amount of MeOH for NENU-28 is  $6.70 \text{ mmol g}^{-1}$  which corresponds to the adsorption of 37.52 molecules of MeOH per catalyst formula unit. Comparison with the initial MOF ( $Cu_3(BTC)_2$ ), which can adsorb  $5.14 \text{ mmol g}^{-1}$  methanol (14.36 MeOH molecules per formula unit), shows that POM-functionalized MOFs bring a significant improvement in the adsorption capacity for MeOH. The NENU-28 hybrid material also showed an increase in the amount of adsorbed EtOH ( $4.78 \text{ mmol g}^{-1}$  or 26.77 molecules of EtOH per formula unit) compared to  $Cu_3(BTC)_2$  ( $3.54 \text{ mmol g}^{-1}$  or 9.89 molecules of EtOH per formula unit). Although the mechanistic details are not fully understood yet, the results indicate that the presence of the Keggin-type POM [ $HPW_{12}O_{40}$ ] in the NENU-28 has a favorable effect on the adsorption properties of the POM-MOF material.<sup>322</sup>

**4.3.2 Removal of aldehydes.** Aldehydes, especially formaldehyde and acetaldehyde, are the most common VOCs present in the air as indoor air pollutants.<sup>323</sup> The primary sources of these air pollutants come from building materials, varnishes, and paints, flooring, and furniture materials. Formaldehyde and acetaldehyde are classified as Group 1 carcinogens and are therefore proven harmful to human health.<sup>323,324</sup> Several approaches have been developed to reduce their concentration. They can be divided into passive (e.g., better ventilation, using formaldehyde-free materials) and active (e.g., removal techniques – adsorption and catalytic oxidation) approaches.<sup>323,324</sup> In this section, the focus will be on the development of different active approaches for the removal of aldehydes.

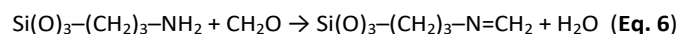
[ $H_4SiW^{VI}_{12}O_{40}$ ] and [ $K_8SiW^{VI}_{11}O_{39}$ ] (0 % efficiency). Kholdeeva *et al.* developed a new Ce-containing polyoxometalate  $NaH_3[SiW^{VI}_{11}Ce^{IV}O_{39}]$  (Ce-POM; **Figure 20**)<sup>278</sup> and its dimer in the solid-state, and tested their promising efficiency in the removal of formaldehyde ( $CH_2O$ ) under mild conditions (20–40 °C). Although the reaction mechanism itself is complex and involves  $CH_2O$  autooxidation, the Haber-Weiss radical-chain process,<sup>325</sup> and product formation inhibition, the reaction stoichiometry itself satisfies the equation in **Figure 20**. The efficiency of an

unoptimized oxidation process of  $CH_2O$  in the presence of Ce-POM/ $O_2$  (efficiency 25 %) was compared to the oxidation of  $CH_2O$  in the presence of  $Ce(SO_4)_2$  (efficiency 9 %) and in the presence of two POMs without Ce(IV) metal atom. The results of these efficiency comparisons suggested that the activity of the Ce-POM catalyst could be attributed to the synergistic action of the POM and Ce(IV). By optimizing the reaction conditions (adding a small amount of  $H_2O_2$ ), the conversion efficiency of  $CH_2O$  increased from 25 % to 85 % with a yield of 66 % HCOOH in the presence of  $NaH_3[SiW^{VI}_{11}Ce^{IV}O_{39}]$ .<sup>278</sup>



**Figure 20.** Aerobic oxidation of formaldehyde to formic acid catalysed by Ce-containing Keggin-type POM ( $NaH_3[SiW_{11}Ce^{IV}O_{39}]$ ) under mild conditions (air,  $T = 25^\circ C$ ).<sup>278</sup>

Gamelas *et al.* successfully immobilized the  $\alpha$ -isomer of the polyoxometalate [ $SiW^{VI}_9O_{37}Ru^{III}_3(H_2O)_3Cl_3$ ] $^{7-}$  (Ru-POM) onto a CSH support, obtaining a heterogeneous catalyst Ru-POM-CSH that was active in formaldehyde oxidation.<sup>326</sup> Oxidation of  $CH_2O$  was performed at room temperature by flushing an air/formaldehyde gas mixture through a Teflon tube filled with Ru-POM-CSH catalyst or only the CSH carrier without POM. Initially, the  $CH_2O$  degradation results for the first two cycles did not differ significantly between CSH and Ru-POM-CSH. This lack of degradation increase could be explained by chemisorption and the reaction between the amino groups of the CSH carrier and  $CH_2O$ :



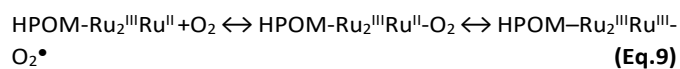
After the second cycle, the efficiency of CSH in the removal of  $CH_2O$  dropped sharply. By the 4th cycle, it was 0 %, which indicates the simple saturation of the CSH carrier. When Ru-POM-CSH was used as a catalyst, efficiency decreased more slowly, with about an 8 % decrease between cycles after the 5th cycle. No catalyst saturation was observed, which can be attributed to the oxidation of  $CH_2O$  catalyzed by Ru-POM. After passing purified air through a Teflon tube containing Ru-POM-CSH material, unlike CSH alone, the material was successfully regenerated. Product analysis revealed that  $CO_2$  and  $H_2O$  were the main reaction products formed by catalytic oxidation of  $CH_2O$  in the presence of Ru-POM-CSH. These results indicate that the reaction undergoes a predominantly non-radical mechanism because the final product would be formic acid and carbon monoxide in the case of a radical mechanism.<sup>326</sup>

The following mechanism of a  $CH_2O$  oxidation reaction in the presence of Ru-POM-CSH was proposed:





The initial step probably involves oxidation of the substrate ( $\text{CH}_2\text{O}$ ) by a catalyst through ligand replacement, binding of  $\text{O}_2$  to the partially reduced catalyst (Eq. 9), and its activation and further reaction with  $\bullet\text{CHO}$ :



The oxidation reaction of  $\text{CH}_2\text{O}$  with Ru-POM-CSH can be summarized as follows:<sup>325</sup>



Kholdeeva *et al.* also synthesized tetra-*n*-butylammonium (TBA) salts of Co-substituted Keggin-type polyoxometalates [TBA<sub>4</sub>HPW<sup>VI</sup><sub>11</sub>CoO<sub>39</sub>] (I) and [TBA<sub>5</sub>PW<sup>VI</sup><sub>11</sub>CoO<sub>39</sub>] (II) (Co-POM) and immobilized them onto both  $\text{NH}_2^-$  and  $\text{NH}_3^+$  modified mesoporous silica surfaces.<sup>282</sup>

The catalytic activity of the solid Co-POM materials (I) and (II) was tested for the oxidation of isobutyraldehyde (IBA) and compared with the activity of the homogeneous Co-POM salts (I) and (II). The results showed that the IBA conversion rate in MeCN under mild conditions (1 atm of air,  $T = 20-40^\circ\text{C}$ ) without a catalyst was 28 %. In the presence of only the  $\text{NH}_2^-$ -modified mesoporous silica support, the IBA conversion rate was only 6 %, indicating that the  $\text{NH}_2^-$  silica support is an inhibitor of the IBA oxidation. When one of the solid Co-POM catalysts, [TBA<sub>4</sub>HPW<sup>VI</sup><sub>11</sub>CoO<sub>39</sub>] (I) or the non-protonated [TBA<sub>5</sub>PW<sup>VI</sup><sub>11</sub>CoO<sub>39</sub>] (II), (immobilized on  $\text{NH}_2^-$  or  $\text{NH}_3^+$ -silica support) was added to the reaction mixture, the IBA oxidation to IBAC continued at room temperature. The protonated salt [TBA<sub>4</sub>HPW<sup>VI</sup><sub>11</sub>CoO<sub>39</sub>] (I) had a higher redox potential and better catalytic activity for IBA oxidation than the non-protonated salt

(II). The catalytic activity of the immobilized Co-POM (I) and the homogeneous salt (I) exhibited similar catalytic performance (92 % IBA conversion) for the first two cycles. However, after the third cycle, the immobilized Co-POM (I) catalyst lost up to 15 % of its activity due to Co-POM leaching, showing that the homogeneous Co-POM (I) salt had better long-term stability.<sup>282</sup> All literature-known polyoxometalates and their applications in removing aldehydes are summarized in Table 2.

#### 4.4 Summary of POM-based technologies in air purification

Various POMs alone and combined with MOFs, CNTs, and mesoporous silica supports show promising results for removing air pollutants including refractory sulfur compounds from fossil fuels (Section 4.1), toxic gases like  $\text{H}_2\text{S}$  (Section 4.2.1),  $\text{NO}_x/\text{SO}_2$  (Section 4.2.2), and carcinogenic VOCs (Section 4.3) in indoor/outdoor air. Keggin-type POM structures dominate oxidative desulfurization of fossil fuels under mild conditions (~85 % of literature; Table S1), outperforming traditional HDS processes and avoiding high pressures/temperatures while meeting ultra-low sulfur regulations. Anderson-Evans POMs enable efficient desulfurization through alkyl peroxide mechanisms with extended lifetimes, while lanthanide-doped Wells-Dawson POMs exhibit superior  $\text{H}_2\text{S}$  oxidation and stability for  $\text{NO}_x/\text{SO}_2$  removal (Table 2).

POM-based hybrid materials further enhance performance, such as  $\text{K}_4\text{PMo}$  mesoporous salts for rapid DBT removal (Table S1),  $\text{PW}_{12}/\text{g-C}_3\text{N}_4$  films mineralizing BETX VOCs under visible light via Z-scheme mechanism, and POM-MOFs like NENU-28 boosting VOC adsorption (Section 4.3). Ce- and Ru-containing Keggin POMs catalyze aldehyde oxidation to  $\text{CO}_2/\text{H}_2\text{O}$  at room temperature, with Ru-POM-CSH showing sustained activity over cycles without saturation (Table 2). Structural diversity tailors redox properties and active oxygen species ( $\bullet\text{OH}$ ,  $\text{O}_2\bullet^-$ ), addressing key air pollutants effectively.

**Table 2.** List of polyoxometalates and POM-based materials utilized in air purification. All POMs are ordered chronologically from the most recent to the oldest published paper.

REMOVAL OF $\text{H}_2\text{S}$					
Formula	POM Archetype	Conditions	Efficiency	Number of cycles	Ref.
$\text{PMo}_{12}@\text{RH-MCM-14}$ ; $\text{PMo}_{12} = [\text{H}_3\text{PMo}^{\text{VI}}_{12}\text{O}_{40}]$	Keggin (Figure 2F)	$T = \text{rt}$ ; $t = 120 \text{ min}$ ; $m(\text{catalyst}) = 0.3 \text{ g}$ ; $c_0(\text{H}_2\text{S}) = 1000 \text{ mg/m}^3$ ; flow rate = 100 $\text{mL/min}$ ( $\text{N}_2/\text{H}_2\text{S}$ gas mixture)	61.3 % yield of $\text{H}_2\text{S}$ transformation to S	more than 8	328
$(\text{Himi})_2[\text{S}^{\text{VI}}\text{Mo}^{\text{VI}}_{12}\text{O}_{40}] \cdot (\text{imi})_2 \cdot \text{H}_2\text{O}$ ; imi = imidazole	Keggin (Figure 2F)	$T = 0-50^\circ\text{C}$ ; $\text{pH} = 4-9$ ; $c(\text{POM}) = 1 \text{ mmol/L}$ ; $c(\text{H}_2\text{S}) = 2 \text{ g/m}^3$ ; flow rate = 100 $\text{mL/min}$ ( $\text{N}_2/\text{H}_2\text{S}$ gas mixture)	$\text{H}_2\text{S}$ capacity in water: 627 $\text{mg/g}$ ; after electro treatment up to 2174 $\text{mg/g}$	4 cycles	329
$(n\text{-Bu}_4\text{N})_3[\text{VMo}^{\text{VI}}_{12}\text{O}_{40}]/[\text{Bmim}]\text{Oac}$ ; [Bmim] = 1-butyl-3-methylimidazolium	Keggin (Figure 2F)	$T = 150^\circ\text{C}$ ; $c(\text{POM}) = 0.005 \text{ mol/L}$ ; flow rate = 100 $\text{mL/min}$ ( $\text{N}_2/\text{H}_2\text{S}$ gas mixture); $t = 10$ h	98.6 % within 10 h	at least 4 cycles	330
$(\text{NH}_4)_{11}[\text{Ln}^{\text{III}}(\text{PMo}^{\text{VI}}_{11}\text{O}_{39})_2]$ ; Ln = Sm, Ce, Dy and Gd	lacunary Keggin (Figure 2G)	$T = \text{rt}$ ; $\text{pH} = 5$ ; $t = 360 \text{ min}$ ; $c(\text{catalyst}) =$ 0.002 M; $c_0(\text{H}_2\text{S}) = 2900 \text{ mg/m}^3$	94.8 % within 360 min	at least 4	331



$K_{17}[Pr^{III}(P_2Mo^{VI}_{17}O_{61})_2]$ , $K_{17}[Gd^{III}(P_2Mo^{VI}_{17}O_{61})_2]$ , $K_{17}[Sm^{III}(P_2Mo^{VI}_{17}O_{61})_2]$ , $K_{17}[Eu^{III}(P_2Mo^{VI}_{17}O_{61})_2]$	Wells-Dawson (Figure 2H)	T = 25 °C; pH = 6.8; t = 400 min; c(catalyst) = 0.015 M; $c_0(H_2S) = 2200 \text{ mg/m}^3$	90 % within 400 min DOI: 10.1039/D5EN00964B	nsp	116
$[Ca^{II}mim]_3[PMo^{VI}_{12}O_{40}] \cdot [Ca^{II}mim]Cl$ ; [Ca <sup>II</sup> mim] = 1-butyl-3-methylimidazolium	Keggin (Figure 2F)	T = 80-180 °C; t = 60 min; H <sub>2</sub> S flow rate 100 mL/min; c(catalyst) = 0.001 M	100 % within 60 min	more than 6	299
TM-salts of $[H_4PMo^{VI}_{11}V^VO_{40}]$ , (TM = Cu <sup>II</sup> , Fe <sup>III</sup> , Zn <sup>II</sup> , Mn <sup>IV</sup> and Cr <sup>VI</sup> )	Keggin (Figure 2F)	T = 25 °C; t = 300 min; H <sub>2</sub> S gas flow = 200 mL/min; $c_0(H_2S) = 1241 \text{ mg/m}^3$ ; c(catalyst) = 0.01 M, H <sub>2</sub> O <sub>2</sub> – oxidant	98 % within 300 min	nsp	54
PyBs-PW, PhPyBs-PW and QBs-PW; PW = H <sub>3</sub> PW <sup>VI</sup> <sub>12</sub> O <sub>40</sub>	Keggin (Figure 2F)	T = 70 °C; t = 10 min; n(H <sub>2</sub> S) <sub>0</sub> = 1 mmol, 30 % H <sub>2</sub> O <sub>2</sub> (n = 1 mmol); solvent mixture H <sub>2</sub> O/EtOH (v:v = 7:3); m(catalyst) = 80 mg	98 % within 10 min	at least 5	332
$[\{(CH_3)_4N\}_4Cu^{II}PW^{VI}_{11}O_{39}H]$	lacunary Keggin (Figure 2G)	T = rt.; t = 20 h; m(cat.) = 10 mg; $c(H_2S)_0 = 0.1M$	95.0 % within 20 h	at least 2	300
$[Na_2HPMo^{VI}_{12}O_{40}]$	Keggin (Figure 2F)	T = 20 °C; c(catalyst) = $1.25 \times 10^{-2} \text{ M}$ ; $c_0(H_2S) = 240.72 \text{ mg/m}^3$ ; H <sub>2</sub> S gas flow = 0.5 L/min	sulfur loading capacity of 1.14 mol of H <sub>2</sub> S per mol of POM	nsp	333
$[Na_3PMo^{VI}_{12}O_{40}]$ , ([Na <sub>3</sub> PMo <sup>VI</sup> <sub>12</sub> O <sub>40</sub> ):NaVO <sub>3</sub> :Na <sub>2</sub> CO <sub>3</sub> :NaCl = 1:1:0.377:5.472)	Keggin (Figure 2F)	T = rt; t = 47 min; c(adsorbent) = $5 \times 10^{-3} \text{ M}$ ; $c_0(H_2S) = 500.863 \text{ mg/m}^3$ ; H <sub>2</sub> S gas flow = 3.931 L/min	up to 99.67 % within 35-50 min	nsp	334
PCDES@3C <sub>14</sub> -2Im; PCDES = long-chain ionic liquid hybrid POM deep eutectic solvent, POM present as $[C_{14}mim]_3PMo^{VI}_{12}O_{40}$ ; [C <sub>14</sub> mim] = 1-tetradecyl-3-methylimidazolium	Keggin (Figure 2F)	T = 25-200 °C; c(adsorbent) = 0.01 mol/L; t = 150 min, H <sub>2</sub> O <sub>2</sub> ; 12.93 mg H <sub>2</sub> S / g adsorbent	Up to 100 % within 150 min	at least 5	334
PPIls@IBuPN-9; PPIls = phosphazene POM ionic liquid, 1-bityl-3-methylimidazolium chloride with phosphazenes and H <sub>3</sub> PMo <sup>VI</sup> <sub>12</sub> O <sub>40</sub>	Keggin (Figure 2F)	T = 100 – 200 °C; t = 2 h; c(PPIls@IBuPN-9) = 0.015 mol/L; 21.88 mg H <sub>2</sub> S / g PPIls@IBuPN-9	Up to 100 % fpr 120 min	at least 4 cycles	336
PMo <sub>12</sub> @UiO-66@H <sub>2</sub> S-MIP-β-CDs; CD = β-cyclodextrin, MIP = molecular imprinted polymers; UiO-66 = metal-organic framework	Keggin (Figure 2F)	T = room temperature; 31.67 mg H <sub>2</sub> S / g; m(adsorbent) = 0.3 g, H <sub>2</sub> S 1000 mg/m <sup>3</sup>	Up to 31.67 mg/g H <sub>2</sub> S within 150 min	5 cycles	337
PMo12-BmimCl@SiO <sub>2</sub> -0.05 %	Keggin (Figure 2F)	m(PMo12-BmimCl@SiO <sub>2</sub> -0.05 %) = 5 g; H <sub>2</sub> S 1000 mg/m <sup>3</sup> , flow rate = 100 mL/min; T = 100 – 200 °C; BmimCl = 1-butyl-3-methylimidazolium chloride	97 % desulfurization for 480 min	3 cycles	338
<b>Formula</b>	<b>POM Archetype</b>	<b>Conditions</b>	<b>Efficiency</b>	<b>Number of cycles</b>	<b>Ref.</b>
<b>REMOVAL OF NO<sub>x</sub> AND SO<sub>2</sub></b>					
PW <sub>12</sub> @Bi <sub>2</sub> O <sub>3-x</sub> /Bi; PW <sub>12</sub> = H <sub>3</sub> PW <sup>VI</sup> <sub>12</sub> O <sub>40</sub> , x = nsp	Keggin (Figure 2F)	LED lamp (λ > 420 nm); m(catalyst) = 0.3 mg; c(NO) = 600 ppb (in air mixture), flow rate(NO) = 500 mL/min	83.3 % within 30 min (in gas phase)	nsp	339
$[H_4GeW^{VI}_{12}O_{40}](HGeW)$ , $[H_5GeW^{VI}_{11}V^VO_{40}](HGeWV)$ , $[H_5GeMo^{VI}_{11}V^VO_{40}](HGeMoV)$ , $[H_5GeW^{VI}_9Mo^{VI}_2V^VO_{40}](HGeWMoV)$	Keggin (Figure 2F)	T = 100-350 °C; rate = 4 °C/min; t = 90 min; c(NO <sub>x</sub> ) = 1696 mg/m <sup>3</sup> ; c(O <sub>2</sub> ) = 8 vol %; c(H <sub>2</sub> O vapor) = 5 vol %	81.5 % NO <sub>x</sub> removal with N <sub>2</sub> selectivity of 68.3 % within 90 min	at least 3	314
H <sub>6</sub> P <sub>2</sub> W <sup>VI</sup> <sub>18</sub> O <sub>62</sub> ·28H <sub>2</sub> O	Wells-Dawson (Figure 2H)	T = 50-200 °C; t = 60 min; $c_0(NO_x) = 1696 \text{ mg/m}^3$ ; c(O <sub>2</sub> ) = 8 vol %; c(vapor) = 4.5 vol %	up to 90 % of NO <sub>x</sub> adsorption within 60 min	at least 2	340
$[Fe^{III}(C_4H_5NO_4)]_3PW^{VI}_{12}O_{40} \cdot 14H_2O$ (Fe <sup>III</sup> AspPW)	Keggin (Figure 2F)	T = 50 °C; t = 15 min; c(H <sub>2</sub> O <sub>2</sub> ) = 4mol/L; pH = 5.5; $c_0(NO) = 603 \text{ mg/m}^3$	94.6 % within 15 min	3	312
Ce <sup>IV</sup> O <sub>2</sub> /H <sub>3</sub> PW <sup>VI</sup> <sub>12</sub> O <sub>40</sub>	Keggin (Figure 2F)	T = 160-220 °C; t = 30 min; $c_0(NO) = 600 \text{ mg/m}^3$ ; c(NH <sub>3</sub> ) = 600 mg/m <sup>3</sup>	90 % NO removal within 30 min	nsp	341

$H_4[(Cu_4Cl)_3(BTC)_8]_2[SiW^{VI}_{12}O_{40}] \cdot (C_4H_{12}N)_6 \cdot 3H_2O$ (NENU-15)	Keggin (Figure 2F)	T = 20-300 °C; c(NO) = 1.74 mmol/g; m(cat.) = 0.2 g; gas mixture NO (5 %) and He (95 %), gas flow rate = 30 mL/min	NO adsorption efficiency of 1.74 mmol/g of NO at rt, and 64 % efficiency at 300 °C	nsp	342
$[Fe^{III}(C_4H_5NO_4)]_3PW^{VI}_{12}O_{40} \cdot 14H_2O$ , ( $Fe^{III}AspPW$ )	Keggin (Figure 2F)	T = 65-80 °C; t = 15 min; c(NO) <sub>inlet</sub> = 614 mg/m <sup>3</sup> ; c(SO <sub>2</sub> ) <sub>inlet</sub> = 2094 mg/m <sup>3</sup> ; c(catalyst) = 0.5 g/L	84.27 % (NO) and 100 % (SO <sub>2</sub> ) within 15 min	3	280
HPW <sup>VI</sup> -M/Ce <sup>IV</sup> <sub>x</sub> Zr <sup>IV</sup> <sub>4-x</sub> O <sub>8</sub> and HPW <sup>VI</sup> -M/Ti <sup>IV</sup> <sub>x</sub> Zr <sup>IV</sup> <sub>1-x</sub> O <sub>4</sub> (M = Pt <sup>IV</sup> , Pd <sup>II</sup> or Rh <sup>III</sup> (1 wt %); Zr <sup>IV</sup> /Ce <sup>IV</sup> = 0.5; Zr <sup>IV</sup> /Ti <sup>IV</sup> = 0.5)	Keggin (Figure 2F)	T = 170-250 °C; t = 31-32 min; m(catalyst) = 300 mg, gas mixture: NO = NO <sub>2</sub> = 500 ppm, O <sub>2</sub> = 10 %, CO <sub>2</sub> = 5 %, H <sub>2</sub> O = 5 %	48 % NO <sub>x</sub> reduction efficiency and 84 % NO <sub>x</sub> storage efficiency within 31-32 min	12	343
H <sub>3</sub> PW <sup>VI</sup> <sub>12</sub> O <sub>40</sub> · 6H <sub>2</sub> O (HPW)	Keggin (Figure 2F)	T = 80-170 °C; m(HPW) = 330 mg; gas mixture: NO = NO <sub>2</sub> = 500 ppm, O <sub>2</sub> = 10 %, CO <sub>2</sub> = 5 %, H <sub>2</sub> O = 5 %	NO <sub>x</sub> adsorption amount is equal to 38 mg/g of HPW	6	344
$[(NH_4)_3PW^{VI}_{12}O_{40}]$	Keggin (Figure 2F)	T = 150 °C; t = 60 min; He gas flow = 15 mL/min; n(NO <sub>2</sub> ) = 17.0 μmol	68 % NO <sub>2</sub> removal within 60 min	3	345
MnCeO <sub>x</sub> -SiW, where SiW = H <sub>4</sub> [SiW <sup>VI</sup> <sub>12</sub> O <sub>40</sub> ]	Keggin (Figure 2F)	gas mixture: 100 ppm chlorobenzene, 500 ppm NO and 500 ppm NH <sub>3</sub> , 11 vol % O <sub>2</sub> ; T = 120-180 °C; t = 30 min; m(catalyst) = 200 mg	100 % NO and chlorobenzene conversion at 180 °C	nsp	346
10HPW-CS-Ce <sub>0.3</sub> -TiO <sub>2</sub> , HPW = H <sub>3</sub> PW <sup>VI</sup> <sub>12</sub> O <sub>40</sub> , CS = chitosan	Keggin (Figure 2F)	gas mixture: 50 ppm chlorobenzene, 500 ppm NO, 500 ppm NH <sub>3</sub> , 5 vol % O <sub>2</sub> , and N <sub>2</sub> as balance gas; m(catalyst) = 100 mg; T = 167-291 °C	100 % conversion of NO at 167 – 288 °C, 90 % conversion of chlorobenzene at 291 °C	nsp	347
<b>Formula</b>	<b>POM Archetype</b>	<b>Conditions</b>	<b>Efficiency</b>	<b>Number of cycles</b>	<b>Ref.</b>
<b>REMOVAL OF ALDEHYDES</b>					
$[SiW^{VI}_5O_{37}Ru^{III}_3(H_2O)_3Cl_3]^{2-}/CSH$ ; CSH = cellulose propylamine-modified silica	Keggin (Figure 2F)	T = rt; c(CH <sub>2</sub> O) = 833 ppm ± 10 %; CH <sub>2</sub> O gas flow rate = 0.25 dm <sup>3</sup> /min; m(catalyst) = 110 mg	44 % for 1 <sup>st</sup> cycle	5	327
$[n-Bu_4N]_4H_5PW^{VI}_6V^{VI}_6O_{40} \cdot 20H_2O$ (PW <sub>6</sub> V <sub>6</sub> ); $[n-Bu_4N]_6[PW^{VI}_9V^{VI}_3O_{40}]$ (PW <sub>9</sub> V <sub>3</sub> ); $[n-Bu_4N]_5H_2PW^{VI}_8V^{VI}_4O_{40}$ (PW <sub>8</sub> V <sub>4</sub> )	Keggin (Figure 2F)	T = rt; t = 144 h; c(CH <sub>2</sub> O) = 0.52 mol/L; P(air) = 1 atm; c(catalyst) = 3.8 mmol/L; solvent – DMA:H <sub>2</sub> O (v/v = 20/1); v(solvent) = 2 mL	up to 42 % of CH <sub>2</sub> O conversion within 144 h	at least 3	348
H <sub>5</sub> PMo <sup>VI</sup> <sub>10</sub> V <sup>VI</sup> <sub>2</sub> O <sub>40</sub> /APTS/SBA-15; H <sub>6</sub> PMo <sup>VI</sup> <sub>9</sub> V <sup>VI</sup> <sub>3</sub> O <sub>40</sub> /APTS/SBA-15; H <sub>4</sub> PMo <sup>VI</sup> <sub>11</sub> V <sup>VI</sup> <sub>1</sub> O <sub>40</sub> /APTS/SBA-15; APTS = γ-aminopropyltriethoxysilane; SBA-15 = aminosilylated silica	Keggin (Figure 2F)	T = 20 °C; t = 24 h; m(catalyst) = 0.1 g; v(O <sub>2</sub> ) = 500 mL; O <sub>2</sub> – oxidant	up to 73 % acetaldehyde conversion after 24 h	5	349
NaH <sub>3</sub> [SiW <sup>VI</sup> <sub>11</sub> Ce <sup>IV</sup> O <sub>39</sub> ]	Keggin (Figure 2F)	T = 20-60 °C; t = 5 h; P = 1 atm; c(CH <sub>2</sub> O) = 4 mM; c(catalyst) = 5.2 mM; solvent H <sub>2</sub> O	85 % CH <sub>2</sub> O conversion within 5 h	30	278
TBA <sub>4</sub> HPW <sup>VI</sup> <sub>11</sub> Co <sup>III</sup> O <sub>39</sub>	Keggin (Figure 2F)	T = 20-40 °C; t = 6 h; P = 1 atm; m(catalyst) = 100 mg; solvents: MeCN or H <sub>2</sub> O	92 % conversion of isobutyraldehyde	at least 3	282

\*nsp- not specified by authors

## 5 Polyoxometalates in sensor applications

Immobilization of POMs on the different supporting surfaces facilitates their electrochemical properties for sensor applications.<sup>350</sup> Numerous methods, such as chemical adsorption<sup>351,352</sup>, electrodeposition<sup>353,354</sup>, encapsulation<sup>355</sup>, the Langmuir-Blodgett process<sup>356,357</sup>, and layer-by-layer deposition<sup>358,359</sup>, have been used to deposit POMs on electrodes to form monolayer or multilayer structures.<sup>352</sup> As can be seen in **Figure 21**, POM-based sensors are used as the analytical unit, in which the POM is immobilized onto a solid substrate utilized as a transducer. If the POM has been successfully immobilized onto the transducer while preserving its structural integrity, the POM part of the sensor should be able to recognize and catalyze the analyte *via* an induced chemical reaction followed by the transformation of the chemical reaction energy into an electrical signal. The electrical signal is later amplified and converted by signal processing equipment into a display.<sup>349</sup> The POM-based sensors, like other sensors, show all main characteristics such as sensitivity, selectivity, linear range, response time, detection limit, and stability.<sup>360</sup> The most critical properties of most POM-based sensors are selectivity and response rate, and often, they are not addressed by authors. For sensors to have high selectivity, the sensor should have a heightened response to a substrate but an inadequate response to interferences. Recently, it has been shown that these issues could be solved by combining the POMs with organic moieties or CNTs with the addition of noble metal NPs. Generally, the POM-based sensors showed good selectivity and low response time while being stable and active at neutral pH.<sup>360,361</sup>

POM-based sensors operate through a synergistic mechanism that involves redox-driven signal transduction, coordination-induced structural alterations, and catalytic amplification processes. This enables the highly sensitive detection of various chemical and biological analytes. The multi-electron redox functionality of POM clusters allows them to undergo reversible changes in oxidation state upon interaction with target species, resulting in measurable outputs that can be electrochemical, optical, or conductometric. In the realm of electrochemical sensing, POMs facilitate rapid electron transfer at the electrode-analyte interface, a process that can be enhanced through their incorporation into conductive matrices or nanostructured supports, thereby optimizing charge-transfer kinetics and reducing detection limits.<sup>362</sup> Optical sensors utilize intervalence charge-transfer transitions or ligand-to-metal charge-transfer phenomena that occur when analytes interact with or reduce the POM framework, resulting in observable shifts in absorbance or luminescence.<sup>363</sup> Furthermore, the catalytic sensing mechanisms exploit the inherent oxidative or reductive catalytic properties of POMs, where reactions initiated by the analyte generate amplified signals under controlled conditions such as specific pH levels, ionic strength adjustments, or the presence of co-substrates.<sup>364</sup> The overall performance of these sensors is heavily influenced by various experimental factors, including the speciation of POMs, electrode modification strategies, solvent polarity, and the

stability range of the POM in the working environment. Consequently, methodological optimization becomes vital for achieving selectivity, reproducibility, and reliability in practical applications.<sup>365</sup>

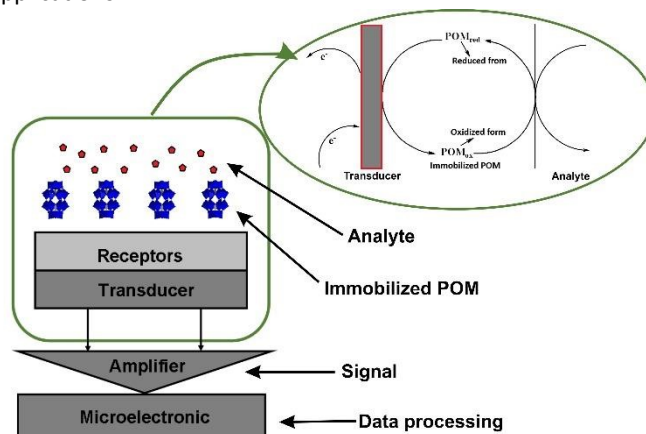


**Figure 21.** Schematic representation of POM-based electrochemical sensors.<sup>349</sup>

### 5.1 POM-based sensors in the detection of water pollution

The POM-based sensors have already explored various analyte classes dispersed in either the gas or liquid phase. The electrocatalytic reduction of nitrate, iodate, bromate, nitrite, and hydrogen peroxide by POMs immobilized on a substrate was carried out for sensing applications. Starting with stable Keggin and Dawson type POMs ( $[H_3PMo^{VI}_{12}O_{40}]$ ,  $[H_6P_2Mo^{VI}_{18}O_{62} \cdot nH_2O]$ ,  $[H_3PW^{VI}_{12}O_{40}]$ ,  $[P_2W^{VI}_{18}O_{62}]^{6-}$ , and  $\alpha-[H_4SiMo^{VI}_{12}O_{40}]$ ) are extensively explored as electrochemical sensors.<sup>361,366–369</sup> Though the sensors showed prominent sensitivity and wide linear range, they operated at a low pH ( $pH < 2$ ) to stabilize the POM architecture.<sup>370</sup> In 2012, Ma *et al.*<sup>371</sup> synthesized a layer-by-layer composite film using palladium nanoparticles and a Dawson-type POM ( $[K_7P_2W^{VI}_{17}O_{61}(FeOH_2) \cdot 8H_2O]$ ,  $(P_2W^{VI}_{17}Fe)$ ) to determine the electrolytic behavior towards the oxidation of hydrazine sulfate ( $N_2H_4SO_4$ ) and reduction of hydrogen peroxide. The  $H_2O_2$  exhibits sensitivity, detection limit, and linear concentration in the range of  $66.7 \mu A mM^{-1}$ ,  $1 \mu M$  ( $S/N = 3$ ),  $1.5 \mu M$  to  $3.9 mM$ , respectively. Likewise,  $N_2H_4SO_4$  displays the same parameter in the range of  $0.2 \mu A mM^{-1}$ ,  $1.5 \mu M$  ( $S/N = 3$ ),  $2 \mu M$  to  $3.4 mM$ , respectively, with sensing response time around  $4s$ .<sup>371</sup> Furthermore, Zhu *et al.*<sup>372</sup> synthesized four Preyssler-type POM-based organic-inorganic crystals to effectively detect non-enzymatic  $H_2O_2$ . The compounds exhibit the lowest detection limit of  $0.13 mM$  with a high sensitivity of  $4.35 \mu A mM^{-1}$  and a response time of  $1s$ .<sup>372</sup> Ag-doped  $MoO_3$  immobilized on the graphene-like carbon nitride ( $C_3N_4$ ) was first prepared and employed as an electrochemical sensor by Zhao *et al.*<sup>373</sup> to detect  $H_2O_2$ . Herein,  $[Ag_6Mo^{VI}_7O_{24}]/Ag-MOF$  precursor was used to synthesize the nanoporous structure resulting in a linear detection range of  $0.25 \mu M-0.43 mM$  towards  $H_2O_2$  owing to its efficient electrocatalytic property.<sup>373</sup> Additionally, isopolymolybdate-based compounds are explored as photoelectric sensors for detecting inorganic ions (e.g.,  $Cr(VI)$ ,  $Hg^{2+}$ ,  $NO_2^-$ ).<sup>374</sup> Additionally, complex POM structures (e.g., pyrazole derivative Keggin ions,<sup>375</sup> 3D coordination polymers doped with Keggin POM<sup>376</sup> or hourglass-type POM



crystals<sup>377</sup> have been explored as the active electrode for the acute and faster sensing of bromate, nitrate, and heavy, metal ions.

## 5.2 POM-based sensors in the detection of air pollution

Krutovtsev *et al.* first addressed POM-based gas sensors by employing various Wells-Dawson type POMs doped with polyaniline to detect ammonia gas.<sup>378</sup> POM-doped conducting polymer film is ideal for gas sensing as POMs react with the gas, and conducting polymer substrate converts that into an electrical signal. The recognition of other hazardous gases, such as NO<sub>x</sub>, CO, and the vapors of organic solvents, can also be determined because the proton-conducting POMs enhance the material's selectivity and sensitivity.<sup>379,380</sup> Ammam *et al.*<sup>381</sup> recently reported a sensitive and selective NO<sub>x</sub> gas sensor using the [K<sub>6</sub>P<sub>2</sub>Mo<sup>VI</sup><sub>18</sub>O<sub>62</sub>·H<sub>2</sub>O] POM and polypyrrole (PPy), exhibiting extended linearities (up to 5500 ppm NO<sub>x</sub>). Although all so far mentioned POM-modified electrodes shows catalytic properties and can recognize the analyte, not all can be employed as sensors. In order to achieve a high-performance sensor, the modified electrode should fulfill the conditions of molecular recognition between POMs and specific analytes.<sup>381</sup> A high-performance gas sensor was developed by Wang *et al.*<sup>382</sup> by using heteropolytungstate (HPT) doped SnO<sub>2</sub> nanorods [HPT abbreviation as (C<sub>4</sub>H<sub>10</sub>ON)<sub>23</sub>[HN(CH<sub>2</sub>CH<sub>2</sub>OH)<sub>3</sub>]<sub>10</sub>H<sub>2</sub>[Fe<sup>III</sup>(CN)<sub>6</sub>(α<sub>2</sub>-P<sub>2</sub>W<sup>VI</sup><sub>17</sub>O<sub>61</sub>Co<sup>II</sup>)<sub>4</sub>·27H<sub>2</sub>O]·SnO<sub>2</sub>/HPT composite film, which demonstrated higher photoconductivity than pristine SnO<sub>2</sub> and revealed improved gas sensing for the methylbenzene and formaldehyde at room temperature (25 °C). Electron-hole recombination in the composite was retarded due to the photo-induced transfer of an electron from SnO<sub>2</sub> to HPT. An n-type semiconductor material BiVO<sub>4</sub> loaded with different POMs, was exploited as a photo-anode for photoelectrochemical gas sensing capability for NO<sub>2</sub>.<sup>382</sup> Among different Keggin type POMs ([Na<sub>7</sub>PW<sup>VI</sup><sub>11</sub>O<sub>39</sub>], [H<sub>3</sub>PW<sup>VI</sup><sub>12</sub>O<sub>40</sub>], [H<sub>3</sub>PMo<sup>VI</sup><sub>12</sub>O<sub>40</sub>], [Na<sub>10</sub>SiW<sup>VI</sup><sub>9</sub>O<sub>34</sub>], [H<sub>3</sub>PW<sup>VI</sup><sub>12</sub>O<sub>40</sub>]) displayed the highest photocurrent response intensity. In addition, BiVO<sub>4</sub>/[H<sub>3</sub>PMo<sup>VI</sup><sub>12</sub>O<sub>40</sub>] demonstrates an enhanced response of 32.8 % toward 50 ppm of NO<sub>2</sub>.<sup>383</sup> In similarity with the previous discussion, herein, the electron-hole recombination was slowed down as the POM facilitates charge separation and photogenerated electron transfer to the semiconductor. Shi *et al.*<sup>384</sup> made an interface modification on the grain boundary by integrating TiO<sub>2</sub>, and Ti<sup>IV</sup> substituted POMs (K<sub>5</sub>[PW<sup>VI</sup><sub>11</sub>Ti<sup>IV</sup>O<sub>40</sub>] and K<sub>5</sub>[PW<sup>VI</sup><sub>10</sub>Ti<sup>IV</sup><sub>2</sub>O<sub>40</sub>]). The resultant nanocomposite exhibited improved photoconductivity and elevated gas sensing properties towards acetone gas.<sup>384</sup> Tian *et al.*<sup>385</sup> investigated the effect of [H<sub>3</sub>PW<sup>VI</sup><sub>12</sub>O<sub>40</sub>] doped In<sub>2</sub>O<sub>3</sub> compound for gas sensing at room temperature toward formaldehyde. The doping of the POM successfully suppressed the recombination of photo-induced carriers in the system resulting in a 35 % enhancement in photoconductivity alongside a 26 % gas sensing response compared with pristine In<sub>2</sub>O<sub>3</sub>.<sup>385</sup> Similarly, Wang *et al.*<sup>386</sup> also incorporated [PW<sup>VI</sup><sub>12</sub>O<sub>40</sub>]<sup>3-</sup> with Cu<sub>2</sub>ZnSnS<sub>4</sub> for high-performance NO<sub>2</sub> gas sensors. The composite exhibited 88.83 % enhanced gas sensing properties compared with pristine

Cu<sub>2</sub>ZnSnS<sub>4</sub> due to the restriction of electron-hole recombination and effective charge transfer through the POM.<sup>386</sup> Furthermore, Sun *et al.*<sup>387</sup> developed dye-sensitized TiO<sub>2</sub>-PW<sub>12</sub> using a simple, economical sol-gel method followed by a screen-printing technique for faster NO<sub>2</sub> gas sensing at room temperature under visible light irradiation. The heterostructure enabled faster separation and transportation of the photogenerated carriers as the POM acted as the electron acceptors. The effective increase in sensitivity (233.1–1 ppm) over a wide range of NO<sub>2</sub> concentration (50 ppb–5 ppm) for POM decorated dye/TiO<sub>2</sub> film occurred due to the expansion of the narrow bandgap of the POM doped dye under visible light without loss in thermal energy.<sup>387</sup> An inorganic-organic hybrid film was fabricated by Kida *et al.* for selective H<sub>2</sub> (50–500 ppm) and NH<sub>3</sub> (10–100 ppm) sensing using yttrium-stabilized zirconia with Mo<sup>VI</sup><sub>7</sub>O<sub>24</sub><sup>6-</sup>/hexylamine hybrid film. Calcination of the POM alkylamine hybrid film resulted in porous MoO<sub>3</sub> particles, making them an effective precursor for synthesizing nanosized metal oxide.<sup>388</sup> POM-based supramolecular chemosensors were developed for the acute gas sensing of toxic gases. Wei *et al.* demonstrated a CO<sub>2</sub> sensor using Na<sub>9</sub>DyW<sup>VI</sup><sub>10</sub>O<sub>36</sub> and block copolymer poly (ethylene oxide-*b*-N, N-dimethyl aminoethyl methacrylate).<sup>389</sup> Likewise, Guo *et al.* developed POM-based supramolecular chemosensors for H<sub>2</sub>S detection (detection limit 1.25 μM) with dual signals (*via* absorption spectra and fluorescence).<sup>390</sup> In the field, rapid detection of acutely corrosive and toxic gases like H<sub>2</sub>S at room temperature is important. Bezdek *et al.* developed enhanced chemiresistive gas sensors to detect H<sub>2</sub>S using highly oxidized Pt-doped POM with single-walled CNT. They have also demonstrated ppb level detection with high stability and a wide range of selectivity.<sup>391</sup> Furthermore, Liu *et al.*<sup>392</sup> immobilized POMs on a polyelectrolyte matrix and then used them for the sensitive detection of NO. The ability to electrocatalyze the reduction of NO resulted in a wide range of selectivity (1 nM to 10 μM).<sup>392</sup> Triethylamine gas sensors developed by Cai *et al.*<sup>393</sup> exhibited ultra-sensitive selectivity and stability over repeated use. One-dimensional heterostructure nanofibers of ZnO and ZnWO<sub>4</sub> were synthesized *via* POM (varying the molar ratio of H<sub>3</sub>PW<sup>VI</sup><sub>12</sub>O<sub>40</sub>) assisted electrospinning methods. The highly porous structure of the nanofibers and the synergistic effect between the ZnO and ZnWO<sub>4</sub> resulted in an enhanced relative response of 108.5 for 50 ppm triethylamine. The barrier-control electron transfer at the interface was attributed to remarkable selectivity with a low detection level of 150 ppb.<sup>393</sup> The recent advances led Tian *et al.*<sup>394</sup> to fabricate POM-semiconductor heterojunctions via a one-step coaxial electrospinning technique for the effective sensing of ethanol gas. One-dimensional tandem heterojunctions SnO<sub>2</sub>/POM/WO<sub>3</sub> significantly increased the sensing characteristics compared with the SnO<sub>2</sub>/WO<sub>3</sub> nanofibers. The sensitivity was optimized to 100 ppm of ethanol. The construction of the interface allowed the POM to act as the electron acceptor, promoting faster carrier separation and exhibiting enhanced sensing behavior.<sup>394</sup> Next, a bottom-up POM-assisted *in-situ* growth of 1D nanofilament architecture was achieved by electrospinning, followed by the thermal oxidation method for the detection of

acetone. A broad range of concentration, *i.e.*, 50 ppb–50 ppm, was detected with enhanced selectivity and sensitivity owing to the charge transfer to the interface of the ZnO–ZnMoO<sub>4</sub> nanofilament.<sup>395</sup> A unique nanostructure was developed by Ren *et al.*<sup>396</sup> using Pt-draped Si-doped WO<sub>3</sub> nanowires interwoven into a three-dimensional mesoporous superstructure for low-temperature ethanol gas sensing (with a detection limit of 0.5 ppm).<sup>396</sup> Selective and ultrasensitive dual detection (Raman and photochromic) of ethylenediamine gas was demonstrated by Zhang *et al.* using POM/viologen hybrid crystal. It exhibits a very low detection limit of 0.1 ppb via Raman signal output.<sup>397</sup>

### 5.3 POM-based sensors in the detection of emerging health pollutants

Very recently, Wang *et al.*<sup>398</sup> synthesized isostructural Anderson-type POM-based compounds and fabricated photoelectric sensors to detect inorganic ions. Three different transition metal ions (M<sup>II</sup> = Co<sup>II</sup>, Cd<sup>II</sup>, Zn<sup>II</sup>) were incorporated for the preparation of the [M<sub>2</sub><sup>II</sup>(H<sub>3</sub>bdpm)<sub>2</sub>TeMo<sup>VI</sup><sub>6</sub>O<sub>24</sub>·6H<sub>2</sub>O] (H<sub>3</sub>bdpm = 1-1'-bis(3,5-dimethyl-1H-pyrazolatemethane) compounds which contain a 2D supramolecular layer and 1D chain structures. All prepared [M<sub>2</sub><sup>II</sup>(H<sub>3</sub>bdpm)<sub>2</sub>TeMo<sup>VI</sup><sub>6</sub>O<sub>24</sub>·6H<sub>2</sub>O] compounds have been successfully utilized as fluorescence sensors toward Cr<sub>2</sub>O<sub>7</sub><sup>2-</sup> at different concentrations. Furthermore, the compounds with Co<sup>II</sup> and Cd<sup>II</sup> also exhibited electrochemical sensing behavior for detecting NO<sub>2</sub><sup>-</sup> (Cd-containing compound possesses a response time of 2.16 s at a detection limit of 5.11 × 10<sup>-5</sup> M alongside a sensitivity of 43.10 μA mM<sup>-1</sup>).<sup>398</sup>

POM and Zn-based complexes derived from pyrazole were reported by Tian *et al.* for photocatalysis and electrochemical

sensors to detect hydrogen peroxide, bromate, and nitrite, by tuning pH.<sup>399</sup> Likewise, Zhang *et al.* tuned the N and O coordination donors in morpholine and piperazine derivatives to derive various POM-based compounds for photocatalysis, electrochemical, and fluorescent sensor applications (towards Hg<sup>2+</sup>).<sup>400</sup> Furthermore, researchers explored POM-modified MOFs for various sensing applications, *e.g.*, photocatalytic, electrochemical (towards the detection of inorganic ions, H<sub>2</sub>O<sub>2</sub>, Cr(VI), bromate, *etc.*).<sup>401–405</sup>

All literature known polyoxometalates and their applications in sensing are summarized in **Table 3**.

### 5.4. Summary of POM-based sensors

POM-based sensors for water pollution, air pollution, and emerging health pollutants are discussed thoroughly. In aqueous sensing, Keggin, Dawson, Preyssler, and isopolymolybdate POMs exhibit strong electrocatalytic activity toward species such as hydrogen peroxide, nitrate, bromate, nitrite, and heavy metal ions, often achieving low detection limits and quick response times. For gas sensing, POM–polymer, POM–metal oxide, and POM–semiconductor heterostructures enable the sensitive and selective detection of gases, including NO<sub>2</sub>, NH<sub>3</sub>, H<sub>2</sub>S, formaldehyde, acetone, ethanol, and volatile amines, mainly by promoting charge separation and reducing electron–hole recombination. Lastly, emerging health-related pollutants are addressed through advanced POM-based supramolecular systems, MOFs, and hybrid complexes that offer electrochemical, photoelectrochemical, and fluorescent sensing modes. Overall, the manuscript highlights the versatility of POMs as functional building blocks for high-performance, multifunctional sensors that operate under mild and environmentally friendly conditions.

**Table 3.** Summarization of the reported POM-based sensors.

POM-based Composite	POM Archetype	Type of Sensor	Significant Results	Ref.
(P <sub>2</sub> W <sup>VI</sup> <sub>17</sub> Fe) and palladium NPs; NPs = nanoparticles	Wells-Dawson (Figure 2H)	electrochemical sensor towards H <sub>2</sub> O <sub>2</sub> and N <sub>2</sub> H <sub>4</sub> SO <sub>4</sub>	The H <sub>2</sub> O <sub>2</sub> and N <sub>2</sub> H <sub>4</sub> SO <sub>4</sub> exhibit sensitivity, detection limit, and linear concentration in the range of 66.7 μA mM <sup>-1</sup> , 1 μM (S/N = 3), 1.5 μM to 3.9 mM, and 0.2 μA mM <sup>-1</sup> , 1.5 μM (S/N = 3), 2 μM to 3.4 mM, respectively.	36
[M <sup>n+</sup> (H <sub>2</sub> O)P <sub>3</sub> W <sub>30</sub> O <sub>110</sub> ] <sup>(15-n)-</sup>	Preyssler-type	electrochemical sensor towards H <sub>2</sub> O <sub>2</sub>	exhibit the lowest detection limit of 0.13 mM with a high sensitivity of 4.35 μA mM <sup>-1</sup> and response time of 1 s	369
K <sub>6</sub> P <sub>2</sub> Mo <sup>VI</sup> <sub>18</sub> O <sub>62</sub> ·H <sub>2</sub> O with polypyrrole	Wells-Dawson (Figure 2H)	NO <sub>x</sub> gas sensor	exhibits extended linearities up to 5500 ppm NO <sub>x</sub>	374
SnO <sub>2</sub> /HPT composite film	Keggin (Figure 2F)	gas sensor for the formaldehyde and methylbenzene	higher photoconductivity compared with pristine SnO <sub>2</sub>	375
BiVO <sub>4</sub> /H <sub>3</sub> PW <sup>VI</sup> <sub>12</sub> O <sub>40</sub>	Keggin (Figure 2F)	NO <sub>2</sub> gas sensor	enhanced response of 32.8 % towards the 50 ppm of NO <sub>2</sub>	376
[M <sub>2</sub> <sup>II</sup> (H <sub>3</sub> bdpm) <sub>2</sub> TeMo <sup>VI</sup> <sub>6</sub> O <sub>24</sub> ·6H <sub>2</sub> O]; H <sub>3</sub> bdpm = 1-1'-bis(3,5-dimethyl-1H-pyrazolatemethane	Anderson-Evans (Figure 2I)	photoelectric sensors for the detection of inorganic ions	Cd-based compound possesses a response time of 2.16 s at a detection limit of 5.11 × 10 <sup>-5</sup> M with a sensitivity of 43.10 μA mM <sup>-1</sup>	377
BiVO <sub>4</sub> /(H <sub>3</sub> PW <sup>VI</sup> <sub>12</sub> O <sub>40</sub> or H <sub>3</sub> PMo <sup>VI</sup> <sub>12</sub> O <sub>40</sub> or	Keggin (Figure 2F)	NO <sub>2</sub> gas sensor	BiVO <sub>4</sub> /PW <sub>12</sub> exhibits highest response of 32.8 % towards 50 ppm of NO <sub>2</sub>	379



Na <sub>7</sub> PW <sup>VI</sup> <sub>11</sub> O <sub>39</sub> Or Na <sub>10</sub> SiW <sup>VI</sup> <sub>9</sub> O <sub>34</sub> )			View Article Online DOI: 10.1039/D5EN00954B	
TiO <sub>2</sub> /[PW <sup>VI</sup> <sub>11</sub> TiO <sub>40</sub> ] <sup>5-</sup> and TiO <sub>2</sub> /[PW <sup>VI</sup> <sub>10</sub> Ti <sub>2</sub> O <sub>40</sub> ] <sup>7-</sup>	Keggin (Figure 2F)	acetone gas sensor	low detection concentration level of acetone is 50 and 80 ppm for TiO <sub>2</sub> /[PW <sup>VI</sup> <sub>11</sub> TiO <sub>40</sub> ] <sup>5-</sup> and TiO <sub>2</sub> /[PW <sup>VI</sup> <sub>10</sub> Ti <sub>2</sub> O <sub>40</sub> ] <sup>7-</sup> , respectively	380
H <sub>3</sub> PW <sup>VI</sup> <sub>12</sub> O <sub>40</sub> doped In <sub>2</sub> O <sub>3</sub> compound	Keggin (Figure 2F)	gas sensor for the formaldehyde at room temperature.	35 % enhancement in photoconductivity alongside a 26 % of gas sensing response compared with pristine In <sub>2</sub> O <sub>3</sub>	381
H <sub>3</sub> PW <sup>VI</sup> <sub>12</sub> O <sub>40</sub> with Cu <sub>2</sub> ZnSnS <sub>4</sub>	Keggin (Figure 2F)	NO <sub>2</sub> gas sensor	exhibits 88.83 % enhanced gas sensing property compared with pristine Cu <sub>2</sub> ZnSnS <sub>4</sub>	382

## 6 Polyoxometalate based battery and supercapacitors

POMs emerge as an exceptional electrode component for supercapacitors (SCs) or batteries due to their high proton mobility and extraordinary redox chemistry.<sup>406–408</sup> POM's variable redox activities and outstanding electron/proton transport capacities apply POM-based composite materials in electrochemical fields. As a powerful electron reservoir in the multi-electron reduction process, POM enables high proton conductivity even in the composite. This interesting behavior has led to various applications of POM-based composites such as green catalysis, sensors, and electrochemical energy storage devices (batteries and SCs). However, POMs are pH-sensitive; therefore, a well-known strategy of coordination chemistry has been used to enhance the mechanical and electrochemical properties of the electrode material for better performance.<sup>407–411</sup>

### 6.1 POM-based battery electrodes

#### 6.1.1 POM as the electrode for lithium-ion batteries (LiBs).

Transition metal oxides are used as the cathode/anode material for LiBs as they are oxidized to their highest oxidation state when the Li has been released.<sup>412</sup> The first reported POMs for LiB are focused on polyoxomolybdates.<sup>413</sup> Further improvements of the electrode material have been made by modifying the structural and electronic states of POMs, altering the reversible faradaic reaction associated with them. Vanadium-based POMs are being explored as cathode materials for rechargeable batteries to achieve high energy and power density by multi-electron redox processes via fast transfer of Li ions. Chen *et al.*<sup>414</sup> reported Li<sub>7</sub>[V<sup>V</sup><sub>15</sub>O<sub>36</sub>(CO<sub>3</sub>)] as a cathode material with a specific capacity of 250 mA h g<sup>-1</sup> alongside energy and power densities of 1.5 kW h L<sup>-1</sup> and 55 kW L<sup>-1</sup>, respectively. Additionally, Li<sub>7</sub>[V<sup>V</sup><sub>15</sub>O<sub>36</sub>(CO<sub>3</sub>)] exhibits a very high potential window (1.9 to 4.0 V) for reversible redox reactions. The theoretical calculation for the specific capacity for the oxometalate mentioned above at the same potential window (by considering n is 14, which is the next nearest integer no. of electrons) shows the specific capacity of 259 mA h g<sup>-1</sup>, which is in corroboration with the experimental data.<sup>414</sup> Further, the vanadium-based K<sub>7</sub>[NiV<sup>V</sup><sub>13</sub>O<sub>38</sub>] structure is explored by Ni *et al.*<sup>415</sup> The maximum discharge capacity of 218.2 mA h g<sup>-1</sup> was

recorded at a discharge current density of 17 mA g<sup>-1</sup> with 93.2 % coulombic efficiency.<sup>415</sup> Thus, the nano-sized polyoxovanadates can be utilized as cathode materials for LiBs for moderate capacity and rate capability.

Furthermore, POMs are combined with carbonaceous nanostructures for better cycle and rate performance. Ma *et al.*<sup>416</sup> synthesized covalent functional pyrene (Py) with [H<sub>4</sub>SiW<sup>VI</sup><sub>12</sub>O<sub>40</sub>] (SiW<sub>12</sub>) and attached it to the surface of SWCNTs *via* spontaneous adsorption. SWCNT/Py-SiW<sub>11</sub> exhibited an initial discharge capacity of 1569.8 mA h g<sup>-1</sup> at a current density of 0.5 mA cm<sup>-2</sup>. However, the capacity decreased to 580 mA h g<sup>-1</sup> after 100 cycles at the same current density.<sup>416</sup> Graphene sheets are represented by single-layer two-dimensional sp<sup>2</sup>-bonded carbon atoms, having a high affinity towards POMs. Wang *et al.*<sup>417</sup> synthesized environmentally friendly nanomaterials by incorporating reduced graphene oxide (rGO) with Keggin type [H<sub>4</sub>SiW<sup>VI</sup><sub>12</sub>O<sub>40</sub>] (SiW<sub>12</sub>) clusters. rGO/SiW<sub>12</sub> exhibits a discharge capacity of 275 mA h g<sup>-1</sup> with an increased potential of 4 V at a current density of 50 mA g<sup>-1</sup>. The nanocomposite can hold a capacity of 120 mA h g<sup>-1</sup> at 1.5 V operating potential even at a high current density of 2000 mA g<sup>-1</sup>.<sup>417</sup> Besides carbonaceous nanostructures, POMs are often synthesized with silver nanoparticles due to their chemical structure, elevated surface area, and high electrical conductivity.<sup>418,419</sup>

In recent years, the POM-based composite structure has been further modified by including MXenes, e.g., i) POM@PANI/Mo<sub>2</sub>TiC<sub>2</sub>TxMXene/CNTs delivers lithium storage capacity of 621 mA h g<sup>-1</sup> at 0.1 A g<sup>-1</sup> and promising cyclic stability (445 mA h g<sup>-1</sup> after 1000 periods at 1.0 A g<sup>-1</sup>)<sup>390</sup>; and ii) PMo<sub>12</sub>@PPy/Ti<sub>3</sub>C<sub>2</sub>T<sub>x</sub> delivers high capacity of 764 mA h g<sup>-1</sup> at 0.1 Ag<sup>-1</sup> with long cycling stability of 2000 cycles at 3 A g<sup>-1</sup>.<sup>420</sup> Additionally, the hybridization of various POMs with different supports such as porphyrins<sup>420</sup>, CoS<sub>2</sub>/MoS<sub>2</sub>/functionalized rGO<sup>421</sup>, and various MOFs<sup>422–425</sup> results in enhanced lithium capacity and overall stability as an anode.

**6.1.2 POM as the electrode for sodium-ion batteries.** Besides LiBs, POM-based composites are applied as cathode/anode material for Na-ion batteries. Liu *et al.*<sup>426</sup> prepared a robust composite by coating Na<sub>2</sub>H<sub>8</sub>[MnV<sup>V</sup><sub>13</sub>O<sub>38</sub>] (POM) clusters on the graphene nanoflakes. The discharge process of the composite demonstrates a two-phase reaction due to the presence of V(V)/V(IV) redox couple related to Na-ion insertion, and a high capacity of 202 mA h g<sup>-1</sup> is recorded at 1.5 V (at the end of the

discharge). Furthermore, the composite can retain 81 % of its initial capacity over 100 cycles at 0.2 C with 95 % coulombic efficiency.<sup>426</sup> Hartung *et al.*<sup>427</sup> reported that the sodium salt of decavanadate,  $\text{Na}_6[\text{V}_{10}\text{O}_{28}]$ , acts as a high-performance cathode material for rechargeable Na-ion batteries. The potential discharge range observed from the CV graph is within the range of 0.01–3.0 V. The capacitive process associated with the  $\text{Na}_6[\text{V}_{10}\text{O}_{28}]$  ion is completed by the insertion of the Na ion in the voids of  $[\text{V}_{10}\text{O}_{28}]^{6-}$  cluster.<sup>427</sup> Additionally, MOFs are proven to be effective supporting materials for POMs. Using a simple impregnation strategy, Cao *et al.*<sup>428</sup> demonstrated that  $\text{PMo}_{12}/\text{MIL-88B}/\text{GO}$  composite delivers an excellent specific capacity of  $214.2 \text{ mA h g}^{-1}$  for 600 cycles at  $2 \text{ A g}^{-1}$ . Another example is a layer-by-layer arrangement of vanadium-based POM immobilized on Co-based MOF resulted in a capacity of  $413 \text{ mA h g}^{-1}$  due to accommodating the larger  $\text{Na}^+$  ions efficiently.<sup>428</sup>

## 6.2 POM-based supercapacitor electrodes

Electrochemical capacitors or SCs, on the other hand, are promising energy storage devices that meet a significant performance gap between batteries and electrostatic capacitors. They supply high-power electric pulses over a short time scale, exhibiting a high dynamic of charge propagation with elevated charge and discharge rates.<sup>429</sup> In the maximum reported SC, high capacitance and energy are achieved by incorporating a pseudocapacitive or faradaic type of active material with a double-layer capacitive component. Mostly, metal oxides and sulfides show promising results for SC electrodes as they generate a large number of charges at the electrode interface via multi-step reversible redox reactions.

**6.2.1 Composite-type hybrid electrode.** Early in 2005, Gómez-Romero *et al.*<sup>407</sup> established the POM-based composite hybrid electrode for SC as they dispersed three different POMs, namely,  $[\text{H}_3\text{PW}^{\text{VI}}_{12}\text{O}_{40}]$ ,  $[\text{H}_4\text{SiW}^{\text{VI}}_{12}\text{O}_{40}]$ , and  $[\text{H}_3\text{PMo}^{\text{VI}}_{12}\text{O}_{40}]$ , in the conducting polymer PANI. The highest specific capacitance of  $120 \text{ F g}^{-1}$  with cycle stability over 1000 cycles was observed for PANI/ $[\text{H}_3\text{PMo}^{\text{VI}}_{12}\text{O}_{40}]$ , which is higher than the other two POM ( $[\text{H}_3\text{PW}^{\text{VI}}_{12}\text{O}_{40}]$ ,  $[\text{H}_4\text{SiW}^{\text{VI}}_{12}\text{O}_{40}]$ ) composite, due to the higher proton conductivity of the  $[\text{H}_3\text{PMo}^{\text{VI}}_{12}\text{O}_{40}]$  in 1 M  $\text{HClO}_4$  electrolyte.<sup>407</sup> In the later years, the same group deposited  $[\text{H}_3\text{PMo}^{\text{VI}}_{12}\text{O}_{40}]$  on different conducting polymers (e.g., poly(3,4-ethylenedioxythiophene) (PEDOT)) with an external oxidizing agent ( $\text{H}_2\text{O}_2$ ) for further electrochemical improvement (Figure 22).<sup>408</sup> Later, the Freund's<sup>430</sup> group used the same Keggin POM,  $[\text{H}_3\text{PMo}^{\text{VI}}_{12}\text{O}_{40}]$ , incorporated into the porous PPy, exhibiting a specific capacitance of  $210 \text{ F g}^{-1}$  in 0.5 M  $\text{H}_2\text{SO}_4$  electrolyte in three-electrode configuration.<sup>430</sup> Recently, Vannathan *et al.*<sup>431</sup> reported high-performance pseudocapacitors of vanadium substituted Keggin POMs and combined with a conducting polymer for enhancement of electrochemical activity.<sup>431</sup> Carbonaceous nanostructures (e.g., CNT, GO/rGO, AC) come into play as the supporting elements to the POMs as they provide better mechanical and electrochemical stability.<sup>429</sup> To replace the conducting polymer as a supporting element for POM, inventors need a high electrical conducting substrate like

the former. CNTs exhibit higher electrical conductivity due to their hierarchical architecture among all the carbonaceous

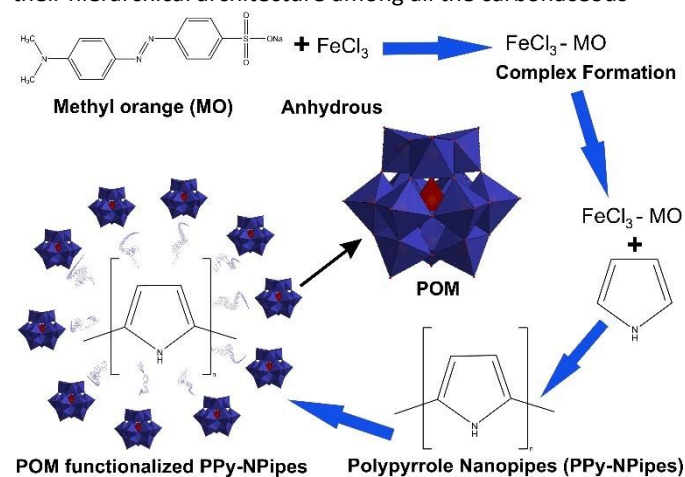


**Figure 22.** Schematic illustration of steps involved in synthesizing polypyrrole nanopipes and polyoxometalates (POMs,  $\text{PMo}_{12}$ , or  $\text{PW}_{12}$ ) hybrid material with the simple chemical method.<sup>408</sup>

nanostructures. At first, Cuentas-Gallegos *et al.*<sup>432</sup> prepared a single-wall CNT and POM composite using Cs substituted phosphomolybdate ( $\text{Cs}[\text{PMo}^{\text{VI}}_{12}\text{O}_{40}]^{3-}$ ). The composite material presented a specific capacitance of  $285 \text{ F g}^{-1}$  and an energy density of  $57 \text{ W h kg}^{-1}$ .<sup>432</sup> Later Shunik *et al.*<sup>433</sup> further developed this concept using multi-walled CNT instead of a single wall. Phosphomolybdic acid-modified multi-walled CNT revealed a specific capacitance of  $40 \text{ F g}^{-1}$  at a discharged current of 7 mA.<sup>433</sup> Furthermore, to achieve a higher surface area substrate without compromising electrical conductivity, the researchers employed AC as a supporting material because it possesses a larger surface area (up to  $3000 \text{ m}^2 \text{ g}^{-1}$ ) with different pore distribution (micro, meso, or macropores). Ruiz *et al.*<sup>434</sup> prepared a hybrid electrode by integrating activated carbon with Keggin-type phosphomolybdate  $[\text{H}_3\text{PMo}^{\text{VI}}_{12}\text{O}_{40}]$  ( $\text{PMo}_{12}$ ). The highest specific capacitance was generated due to the faradaic component, around  $183 \text{ F g}^{-1}$  at  $2 \text{ A g}^{-1}$  current density.<sup>434</sup> In 2014, the same group used molybdenum-based POMs instead of phosphotungstate  $[\text{H}_3\text{PW}^{\text{VI}}_{12}\text{O}_{40}]$  for an electrochemical study and observed an enhancement of the capacitance to  $254 \text{ F g}^{-1}$  in an operating potential of 1.6 V. Moreover, the composite can possess 98 % capacitance over 30000 cycles.<sup>435</sup> Besides Keggin-type POMs, Mu *et al.*<sup>436</sup> for the first time embedded a Dawson-type POM,  $(\text{NH}_4)_6[\text{P}_2\text{Mo}^{\text{VI}}_{18}\text{O}_{62}]$  on AC and achieved the highest capacitance of  $308 \text{ F g}^{-1}$  at  $2 \text{ A g}^{-1}$  current density due to the high proton conductivity and unique redox behavior of the faradaic component.<sup>436</sup> Besides commercially available activated carbon, Lian *et al.* used biomass-derived pinecone activated carbon, in which POMs ( $\text{PMo}^{\text{VI}}_{12}\text{O}_{40}^{3-}$ ) contributed to a high specific capacitance of  $361 \text{ F g}^{-1}$ , showing the trend of proton-coupled electron transfer (Figure 23).<sup>437</sup> Recently, Maity *et al.*<sup>438</sup> developed vanadium-substituted Keggin structures ( $\text{PMo}^{\text{VI}}_{11}\text{VO}_{40}$  and  $\text{PMo}^{\text{VI}}_{10}\text{V}_2\text{O}_{40}$ ) impregnated into the surface of AC. The vanadium



concentration in the polyanion plays a vital role as it decides the morphology and microstructure of the nanocomposite.<sup>438</sup>

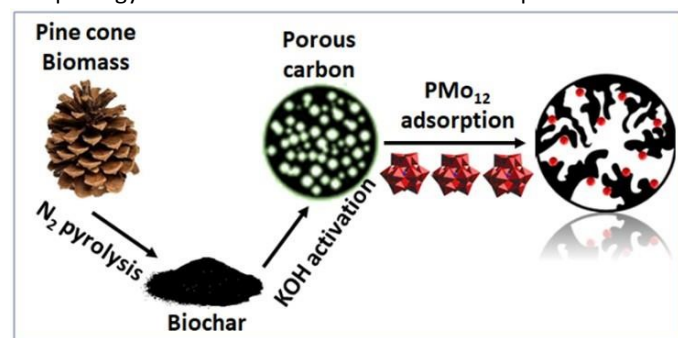


**Figure 23.** Synthesis schematic for porous pinecone biomass carbon and fabrication of pinecone – polyoxometalate hybrid material.<sup>437</sup>

Graphene or its oxide derivatives (GO and rGO) are used mainly as substrate components other than CNTs and AC because of their high surface area with sizeable electrical conductivity. Additionally, the presence of oxygen-containing functional groups in GO and rGO enables many active sites for the physisorption of a faradaic component. Gomez-Romero and his team did permutation and combined possible routes to achieve high-performance SC using POM and graphene offshoots.<sup>439,440</sup> In this course, they have found a new route to synthesize the hybrid  $\text{PMo}_{12}$ -rGO nanoelectrode with a hydroquinone-doped hybrid gel hybrid electrolyte. The double hybridization enhances cell potential (1.6 V) and electrochemical properties by increasing the volumetric capacitance to  $3.18 \text{ F cm}^{-3}$ . Similarly, for the phosphotungstate composite (rGO-PW<sub>12</sub>), the areal capacitance is calculated as  $2.95 \text{ F cm}^{-3}$ .<sup>439,440</sup> Instead of a single supporting medium for POMs, Qin *et al.*<sup>441</sup> (**Figure 24**) prepared a new type of composite by anchoring  $\text{PMo}_{12}$  to PPy/rGO by layer-by-layer deposition for high-performance micro-SC in solid gel electrolyte medium (PVA/H<sub>2</sub>SO<sub>4</sub>; PVA = polyvinyl alcohol). The resultant composite exhibited high energy and power densities of  $4.8 \text{ mW h cc}^{-1}$  and  $645.1 \text{ mW cc}^{-1}$ , respectively. Also, due to the presence of a solid electrolyte, it presents excellent mechanical flexibility (96 % capacitance retention at a highly bending angle of 180°).<sup>441</sup> Furthermore, surface modifications of graphene derivatives were made using various POM structures, demonstrating enhanced electrochemical performances.<sup>442–445</sup> To achieve seamless ion transportation to the electrode/electrolyte interface Maity *et al.*<sup>446</sup> designed and tailored a facile bottom-up approach in which vanadium-substituted Keggin POMs ( $\text{PMo}_{11}\text{VO}_{40}$ ) were used to oxidize pyrrole monomer followed by the deposition on the GO surface. The resultant nanohybrid not only exhibits unique architecture but displays high-performance supercapacitive behavior.<sup>446</sup> The designing and construction of polyoxometalates-based metal-organic frameworks composites further expands the search for promising high-performance electrode materials for SCs. A Dawson type<sup>447</sup> the basket-shaped heteropoly blue<sup>448</sup>, Keggin type<sup>449</sup>, and Anderson type<sup>450,451</sup> POMs hybridized in metal or covalent organic frameworks overcome the limitations of POMs, e.g.,

high solubility in common electrolytes and results in better stability over longer cycles with improved capacitance.

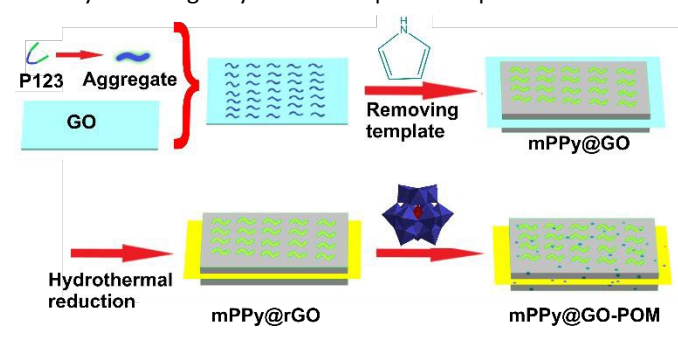


**Figure 24.** Scheme illustration of fabrication procedure of mPPy@rGO-POM nanosheets.<sup>441</sup>

**6.2.2 Asymmetric type hybrid electrode.** Asymmetric type hybrid enhances electrochemical performances in two ways; for instance, incorporating two types of material in a single device enables different charge storage mechanisms simultaneously. Secondly, the cell voltage is tuneable (mainly can be enhanced) due to the presence of various active materials in electrodes. Chen *et al.*<sup>452</sup> studied the electrochemical properties of vanadium-based iso-polyanion, sodium decavanadate ( $[\text{Na}_6\text{V}_{10}\text{O}_{28}]$ ) in 1 M LiClO<sub>4</sub> organic solution, exhibiting an excellent electrochemical behavior in a 3-electrode configuration. Furthermore, an asymmetric SC configuration was developed using activated carbon as the positive and  $[\text{Na}_6\text{V}_{10}\text{O}_{28}]$  as the negative electrode, exhibiting a maximum specific capacitance of  $269 \text{ F g}^{-1}$ , with energy and power densities of  $73 \text{ W h kg}^{-1}$  and  $312 \text{ W kg}^{-1}$ , respectively, in a 2.8 V operating potential.<sup>452</sup> Hu *et al.*<sup>453</sup> studied a composite type of electrode using regular  $\text{PMo}_{12}$  anchored on AC in a protic ionic liquid electrolyte. Later, the nanocomposite was assembled as an asymmetric SC device with commercially available AC. The asymmetric cell operates in an elevated potential window of 0–0.85 V, even at a high current density ( $10 \text{ A g}^{-1}$ ).<sup>453</sup> Dubal *et al.*<sup>454</sup> developed a high-performance symmetric SC based on  $\text{PMo}^{\text{VI}}_{12}$  and  $\text{PMo}^{\text{VI}}_{12}$ -rGO. They assembled an asymmetrical SC device using rGO- $\text{PMo}^{\text{VI}}_{12}$  and rGO-PW<sup>VI</sup><sub>12</sub> electrodes for higher energy density. The SC cell also operates at 1.6 V potential and elevated energy density of  $39 \text{ Wh kg}^{-1}$  at a power density of  $658 \text{ W kg}^{-1}$ .<sup>454</sup> Maity *et al.*<sup>455</sup> optimized the effective loading of POM ( $[\text{Ni}^{\text{IV}}_{14}\text{O}_{40}]^{7-}$ ) on the AC surface for the first time and employed the nanocomposite as the cathode in an asymmetric configuration with AC as the anode. The resultant device exhibited an enhanced specific energy of  $90 \text{ W h kg}^{-1}$  and specific power of  $2400 \text{ W kg}^{-1}$ . Moreover, the nanocomposite-based asymmetric configuration with pristine POM as the positive electrode showed supercapattery behavior.<sup>455</sup> All literature-known POM-based batteries and supercapacitors are summarized in **Table 4**.

### 6.3. Summary of POM-based batteries and supercapacitors

The use of polyoxometalates (POMs) as advanced electrode materials for electrochemical energy storage highlights their

 1  
2  
3  
4  
5  
6  
7  
8  
9  
10  
11  
12  
13  
14  
15  
16  
17  
18  
19  
20  
21  
22  
23  
24  
25  
26  
27  
28  
29  
30  
31  
32  
33  
34  
35  
36  
37  
38  
39  
40  
41  
42  
43  
44  
45  
46  
47  
48  
49  
50  
51  
52  
53  
54  
55  
56  
57  
58  
59  
60  
 Downloaded on 24/10/2026 22:48:39  
 This article is licensed under a Creative Commons Attribution 3.0 Unported Licence.

remarkable redox activity, high proton mobility, and fast electron/proton transport. These inherent qualities make POMs appealing for use in batteries and supercapacitors, although their sensitivity to pH and solubility issues necessitate structural modifications and hybridization via coordination chemistry to develop mechanically durable and electrochemically stable electrodes. In batteries, especially those based on vanadium- and molybdenum-based clusters, POMs serve as active materials in lithium- and sodium-ion batteries. Their multi-electron redox processes allow for moderate to high specific capacities and a wide range of operating potentials. Hybridizing POMs with conductive supports, such as carbon nanotubes, graphene, MXenes, metal nanoparticles, MOFs, and polymer matrices, significantly improves capacity retention, rate performance, and long-term cycling stability. These approaches

effectively overcome the limitations of pure POMs and facilitate efficient ion accommodation. In supercapacitors, POM-based composite and asymmetric electrodes bridge the performance gap with batteries by combining faradaic pseudocapacitance and electric double-layer storage. Key supports such as conducting polymers, carbon materials, graphene derivatives, and porous carbons enhance electrical conductivity, surface area, and mechanical strength. Advanced hybrid structures—including layer-by-layer assemblies, POM-graphene gels, MOF-supported POMs, and asymmetric devices—offer high specific capacitance, broader voltage ranges, excellent energy and power densities, and long cycle life. Overall, this manuscript presents POM-based composites as versatile, high-performance electrode platforms for future energy storage solutions.

**Table 4.** Summarization of the reported POM-based battery and supercapacitors.

POM-based Composite	POM Archetype	Type of Energy Storage	Significant Results	Ref.
$\text{Li}_7[\text{V}_{15}\text{O}_{36}(\text{CO}_3)]$	spherical isopolyvanadate	Li-ion Battery	specific capacity of $250 \text{ mA h g}^{-1}$ alongside energy and power density of $1.5 \text{ kW h L}^{-1}$ and $55 \text{ kW L}^{-1}$ , respectively	392
SWCNT/Py-SiW $^{VI}_{11}$ ; SWCNT = single-walled carbon nanotubes	lacunary Keggin	Li-ion Battery	exhibits an initial discharge capacity of $1569.8 \text{ mA h g}^{-1}$ at a current density of $0.5 \text{ mAcm}^{-2}$	394
$\text{Na}_2\text{H}_8[\text{MnV}_{13}\text{O}_{38}]$ cluster on the graphene nanoflakes	trimeric polyoxovanadate	Na ion Battery	high capacity of $202 \text{ mA h g}^{-1}$ is recorded at $1.5 \text{ V}$ with <b>81 %</b> of its initial capacity retention over 100 cycles	396
PANI/H $_3$ PMo $^{VI}_{12}$ O $_{40}$ ; PANI = polyaniline	Keggin	composite type SC	highest specific capacitance of $120 \text{ F/g}$ with cycle stability over 1000 cycles	385
$([\text{PV}^{\text{V}}\text{Mo}^{\text{VI}}_{11}\text{O}_{40}]^{4-}, [\text{PV}^{\text{V}}_2\text{Mo}^{\text{VI}}_{10}\text{O}_{40}]^{5-})$ with AC	Keggin	composite type SC	AC-VMo $_{11}$ composite displayed an enhanced capacitance of $450 \text{ F g}^{-1}$ with an improved energy density of $59.7 \text{ W h kg}^{-1}$ alongside 99.99 % capacitance retention of over 5000 cycles	407
PMo $^{VI}_{12}$ to PPy/rGO by layer-by-layer deposition; PPy = polypyrrole; rGO = reduced graphene oxide	Keggin	composite type SC	composite possesses high energy and power densities of $4.8 \text{ mW h/cc}$ and $645.1 \text{ mW/cc}$ , respectively	410
$[\text{MnV}^{\text{V}}_{14}\text{O}_{40}]^{6-}$ on the AC and GO; AC = activated carbon; GO = graphene oxide	Lindqvist	composite type SC	AC/MnV $_{14}$ nanohybrid exhibits a specific capacitance of $547 \text{ F g}^{-1}$ with specific energy and power of $76 \text{ W h kg}^{-1}$ and $1600 \text{ W kg}^{-1}$ , respectively, at $0.8 \text{ Ag}^{-1}$ current density. GO/MnV $_{14}$ shows a specific capacitance of $330 \text{ F g}^{-1}$ with specific energy and power of $30 \text{ W h kg}^{-1}$ and $1276 \text{ W kg}^{-1}$ , respectively, at the same current density	414
PMo $^{VI}_{12}$ anchored on AC in a protic ionic liquid; AC = activated carbon	Keggin	asymmetric SC	asymmetric cell operates in a potential window of $0-0.85 \text{ V}$ at $10 \text{ A g}^{-1}$ of current density	417
rGO-PMo $^{VI}_{12}$ and rGO-PW $^{VI}_{12}$ ; rGO = reduced graphene oxide	Keggin	asymmetric SC	the cell operates at $1.6 \text{ V}$ potential and elevated energy density to $39 \text{ W h/kg}$ with a power density of $658 \text{ W/kg}$	426
AC//AC-K $_2$ H $_5$ [NiV $^{\text{V}}$ $_{14}$ O $_{40}$ ]; AC = activated carbon	Lindqvist	asymmetric SC	increased the potential window up to $1.5 \text{ V}$ and enhanced the specific energy and power values ( $90.1 \text{ W h kg}^{-1}$ and $2400 \text{ W kg}^{-1}$ , respectively), with 98 % coulombic efficiency	427

## 7 Conclusions and Outlook

It is almost impossible to overemphasize the applications of POMs in environmental remediation. By looking at the number of environmental studies mentioning POMs in the removal of various pollutants from water, soil or air, it seems that POMs are involved everywhere. This increasing number of environmental degradation studies (Figure 3) involving POMs could be mostly explained by the versatility of the structural chemistry of POMs (Figure 2) and the catalytic features specific to transition metals.

POMs in water column filters and/or in porous organic-inorganic composites proved to be effective in the removal of toxic heavy metals, aromatic organic pollutants, and bacteria (Figures 4, 5 and 7). POMs in porous nanosheets are capable of the photocatalytic degradation of emergent pollutants, particularly antibiotics (Figure 8, Tables 1 and S2), with enhanced photocatalytic performance under visible light (Figure 9), but also dyes, plastics, industrial chemicals, and pesticides (Tables 1 and S2). Moreover, a magnetic core enclosed by polyoxometalate-based ionic liquid phases (Figure 12) was used to remove dyes, heavy metals, microbes, and microplastics (MPs). MPs are not only one of the new emergent health pollutants but also a major one of worldwide concern, in addition to being associated with joint contamination with heavy metals.

POMs, alone and/or in combination with other compounds, such as metal-organic frameworks (MOFs), carbon nanotubes (CNTs) and mesoporous silica supports, have shown promising results in the removal of air pollutants from fossil fuels due to their selective catalytic properties for the oxidation of sulfur compounds (Figures 13, 14, and 15, Table S1). In addition, toxic gases such as hydrogen sulfide, nitrogen oxides and sulfur dioxide are efficiently removed by POMs (Figure 16, Table 2), whereas the volatile organic compounds' reaction mechanism involves a photocatalytic oxidation catalyzed by the  $PW_{12}/g-C_3N_4$  hybrid material (Figure 17).

The immobilization of POMs on different supporting surfaces facilitates their electrochemical properties for sensor application (Figure 19, Table 3). Conversely, their variable redox activities and outstanding electron/proton transport capacities make POM-based composite materials suitable for use in electrochemical fields as an exceptional electrode component for supercapacitors and batteries (Table 4). A high-performance pseudocapacitor was obtained by replacing multiple Mo centers in  $[H_3PMo^{VI}_{12}O_{40}]$  with vanadium and incorporating modified a phosphomolybdate with a conducting polymer for improved electrochemical activity (Figure 20), whereas a biomass-derived pinecone activated carbon, that includes POMs contributed to a high specific capacitance (Figure 21). Carbon nanostructures, graphene oxide/reduced graphene oxide, and activated carbon composites come into play as supporting elements for the POMs as they provide better mechanical and electrochemical stability for broader electrochemical applications (Figures 22 and 23). Although this review does not reveal everything, it may help to get closer to viable solutions for the effective use of the POM-based materials for the removal of the

environmental pollutants. The future is bright for POM applications in environmental treatments!

## Data availability

Data sharing does not apply to this article as no datasets were generated or analyzed during the current study.

## Conflicts of interest

There are no conflicts to declare.

## Acknowledgements

M.M. is grateful to Ferdowsi University of Mashhad and RADA Think Tank (Research for Academic Development & Advancement) for financial support. This study received Portuguese national funds from FCT - Foundation for Science and Technology through contracts UID/04326/2025, UID/PRR/04326/2025 and LA/P/0101/2020 (DOI:10.54499/LA/P/0101/2020) (M.A.)

This research was also funded in whole or in part by the Austrian Science Fund (FWF) (Grant DOI: 10.55776/PAT4299925 (A.R.)). For open access purposes, the author has applied a CC BY public copyright license to any author accepted manuscript version arising from this submission.

The authors would like to acknowledge Dr João Mateus for providing the professional illustration of Figure 1 and also for the Graphical abstract illustration.

## Notes and references

**Abbreviations.** Ac, acetic acid; AC, activated carbon; AOP, advanced oxidation process; APTMS, 3-aminopropyltrimethoxysilane; APTS,  $\gamma$ -aminopropyltriethoxysilane; Asp, aspartic acid; Bbi, 1,1'-(1,4-butanediyl)bis(imidazole); BE, berberine; bimb, 1,4-bis(1-imidazolyl)benzene; bipy, bipyridine; BMIM or bmim, 1-butyl-3-methylimidazolium; BPA, bisphenol A; BPA-Br, bromobisphenol-A; BPy, 1-butylpyridinium or N-butylpyridinium; BR46, basic red 46; BT, benzothiophene; BTC, 1,3,5-benzenetricarboxylate; CCNF, carbonized cellulose nanofiber; CNTs, carbon nanotubes; CP, chlorphenole; 4-CP, 4-chlorophenole; CPF, ciprofloxacin; CPBPY, N-(3-carboxyphenyl)-4,4'-bipyridinium; cpt, 4-(4'-carboxyphenyl)-1,2,4-triazolate; CSH, cellulose propylamine-modified silica; CTS, chitosan; CV, crystal violet; DBP, di-n-butyl phthalate; DBT, dibenzothiophene; DESs, deep eutectic solvents; DMDBT, 4,6-dimethyldibenzothiophene; DODA-Br, dimethyldioctadecylammonium bromide; DODMAC, dimethyldioctadecylammonium chloride; ECSA, electrochemically active surface area; EDA-CD, per-(6-deoxy-6-iodo)- $\beta$ -cyclodextrin; ELSA, electrochemically active surface area; en, ethylenediamine; EPs, emergent pollutants; EtOH, ethanol; etpy, 4-ethylpyridine; EY, eosin Y; g-BN, graphene-like hexagonal boron nitride; GA, graphene aerogel; GO, graphene oxide; Gr, graphene; HOMO, highest occupied molecular orbital; HPW or  $PW_{12}$ ,  $[H_3PW^{VI}_{12}O_{40}\cdot 6H_2O]$ ;  $H_2pyttz-I$ , 3-(pyrid-2-yl)-5-(1H-1,2,4-triazol-3-yl)-1,2,4-triazolyl;  $H_2pyttz-II$ , 3-(pyrid-4-yl)-5-(1H-1,2,4-triazol-3-yl)-1,2,4-triazolyl;  $H_3bdpm$ , 1,1'-bis(3,5-dimethyl-1H-pyrazolatemethane); IBA, isobutyraldehyde; IBAC, isobutyric acid; IBP, ibuprofen; IL, ionic liquid; imi, imidazole; iPAF-1, porous aromatic framework; LiBs, lithium-ion batteries; LDH, layered double hydroxide; LMCT, ligand to metal charge transfer; LPMS, large-pore mesoporous silica; LRSR, liquid-redox sulfur recovery; LUMO, lowest unoccupied molecular

- orbital; MB, methylene blue; MBT, 2-mercaptobenzothiazole; MCM-41, conventional molecular sieve MCM-41; MeCN, acetonitrile; MeOH, methanol; mepy, 4-methylpyridine; MO, methyl orange; MOFs, metal-organic frameworks; MOG, metal-organic gel; MPs, microplastics; MR, methyl red; M-TCS, methyl triclosan; NAD, 2-(1-naphthyl)acetamide; NBZ, nitrobenzene; NFZ, nitrofurazone; NPs, (metal) nanoparticles; ODS, oxidative desulfurization; PANI, polyaniline; PBV, patent blue V; pca, pyridine-2-carboxylic acid; PDDA, poly(diallyldimethylammonium chloride); PEI, polyetherimide; phen, 1,10-phenanthroline; PIL, protic ionic liquid; PMIn, polyionene; PMOE, (ethylene-bridged) periodic mesoporous organosilica; PMs, particulate matters; POM, polyoxometalate; POMCP, POM-based coordination polymer; POM-IL, polyoxometalate-based ionic liquid; POMos, polyoxomolybdates; POM-SILP, polyoxometalate-supported ionic liquid phase; POT, polyoxotungstate; PPI, proton pump inhibitor; PPy, polypyrrole; PS, ponceau S; PTMS, 3-aminopropyl trimethoxysilane; PVA, polyvinyl alcohol; PVDF, polyvinylidene fluoride; py, pyrene; PyPS, 3-(pyridine-1-ium-1-yl)propane-1-sulfonate; PZC, point-of-zero charge; RB, rose bengal; RB5, reactive black 5; RhB, rhodamine B; RH, rice husk; rGO, reduced graphene oxide; SAB, sodium-activated bentonite; SBA-15, aminosilylated silica; SC, supercapacitor; SCR, selective catalytic reduction; SDV, sodium decavanadate; SMT, sulfamethazine; SPD, sulfapyridine; SPME, solid-phase microextraction; SSA, 5-sulfosalicylic acid; SSZ, sulfasalazine; SWCNTs, single-walled carbon nanotubes; TB, toluidine blue; TBA, tetra-n-butylammonium ion; TBBA, tetrabromobisphenol-A; TC, tetracycline; TCS, triclosan; TCY, tetracycline; TMA, *N*-trimethoxysilylpropyl-*N,N,N*-trimethylammonium; TMR4A, resorcin[4]arene-based ligand; TOA, tetraoctylammonium; TPD-MS, temperature-programmed desorption-mass spectroscopy; VOCs, volatile organic compounds; 4,6-DMDBT, 4,6-dimethyl dibenzothiophene; [mim(CH<sub>2</sub>)<sub>3</sub>COO], 1-carboxypropyl-3-methyl imidazole; [C<sub>4</sub>mim]<sup>+</sup>, 1-butyl-3-methylimidazolium ion; β-EDA-CD, per-6-deoxy-6-ethylenediamine-β-cyclodextrin.
- Rizzo L, Malato S, Antakyali D, Beretsou VG, Đolić MB, Gernjak W, et al. Consolidated vs new advanced treatment methods for the removal of contaminants of emerging concern from urban wastewater. *Sci Total Environ.* 2019;655:986–1008. doi:10.1016/j.scitotenv.2018.11.265
  - Mustapha MA, Manan ZA, Wan Alwi SR. A New Quantitative Overall Environmental Performance Indicator for a Wastewater Treatment Plant. *J Clean Prod.* 2017;167:815–823. doi: 10.1016/j.jclepro.2017.08.169
  - Leung DYC, Drakaki E. Outdoor-Indoor Air Pollution in Urban Environment: Challenges and Opportunity. *Front Environ Sci.* 2015;2(69):1–7. doi: 10.3389/fenvs.2014.00069
  - Nathanson JA. Pollution. In: Encyclopedia Britannica [Internet]. Chicago: Encyclopædia Britannica, Inc.; [updated 2025 Sep 12; cited 2025 Sep 17]. Available from: <https://www.britannica.com/science/pollution-environment>
  - Directorate-General for Energy, European Commission. In focus: renewable energy in Europe [Internet]. Brussels: European Commission; 2020 Mar [cited 2025 Sep 17]. Available from: [https://ec.europa.eu/info/news/focus-renewable-energy-europe-2020-mar-18\\_en](https://ec.europa.eu/info/news/focus-renewable-energy-europe-2020-mar-18_en)
  - Klepac P, Locatelli I, Korošec S, Künzli N, Kukec A. Ambient air pollution and pregnancy outcomes: a comprehensive review and identification of environmental public health challenges. *Environ Res.* 2018;167:144–59. doi:10.1016/j.envres.2018.07.008
  - Briggs D. Environmental Pollution and the Global Burden of Disease. *Br Med Bull.* 2003;68(1):1–24. doi: 10.1093/bmb/ldg019
  - Parker L. What You Need to Know About the World's Water Wars. National Geographic. Mar 2020. <https://www.nationalgeographic.com/science/article/world-aquifers-water-wars>. Accessed Sep 17, 2025.
  - Gleick PH. Water In Crisis: Paths To Sustainable Water Use. *Ecol Appl.* 1998;8(3):571–579. doi: 10.1890/1051-0761(1998)008[0571:WICPTS]2.0.CO;2
  - Geissen V, Mol H, Klumpp E, Umlauf G, Nadal M, van der Ploeg M, et al. Emerging pollutants in the environment: a challenge for water resource management. *Int Soil Water Conserv Res.* 2015;3(1):57–65. doi:10.1016/j.iswcr.2015.03.002
  - United Nations Environment Programme and World Meteorological Organization. International Conference on Water and the Environment: Development Issues for the 21st Century [Internet]. Nairobi: UNEP; 1992 [cited 2025 Sep 1]. Available from: <https://wedocs.unep.org/20.500.11822/30961>
  - Zhuo R, Fan F. A Comprehensive Insight into the Application of White Rot Fungi and Their Lignocellulolytic Enzymes in the Removal of Organic Pollutants. *Sci Total Environ.* 2021;778:146132. doi: 10.1016/j.scitotenv.2021.146132
  - Alipoori S, Rouhi H, Linn E, Stumpfl H, Mokarizadeh H, Esfahani MR, et al. Polymer-based devices and remediation strategies for emerging contaminants in water. *ACS Appl Polym Mater.* 2021;3(2):549–77. doi:10.1021/acsapm.0c0117
  - Witkowski KM, Johnson NE. Organic-solvent water pollution and low birth weight in Michigan. *Social Biology.* 1992;39(1–2):45–54. doi: 10.1080/19485565.1992.9988803
  - United Nations World Water Assessment Programme. UN World Water Development Report: Water for people, water for life (WWDR1) [Internet]. Paris: UN-Water; 2003 Mar [cited 2025 Sep 1]. Available from: <https://www.unwater.org/publications/un-world-water-development-report-2003>
  - Richardson SD, Ternes TA. Water Analysis: Emerging Contaminants and Current Issues. *Anal Chem.* 2011;83(12):4614–4648. doi: 10.1021/ac200915r
  - von der Ohe PC, Dulio V, Slobodnik J, De Deckere E, Kühne R, Ebert R-U, et al. A new risk assessment approach for the prioritization of 500 classical and emerging organic microcontaminants as potential river basin specific pollutants under the European Water Framework Directive. *Sci Total Environ.* 2011;409(11):2064–77. doi:10.1016/j.scitotenv.2011.01.054
  - de Andrade JR, Oliveira MF, da Silva MGC, Vieira MGA. Adsorption of Pharmaceuticals from Water and Wastewater Using Nonconventional Low-Cost Materials: A Review. *Ind Eng Chem Res.* 2018;57(9):3103–3127. doi: 10.1021/acs.iecr.7b05137
  - Marican A, Durán-Lara EF. A Review on Pesticide Removal through Different Processes. *Environ Sci Pollut Res.* 2018;25(3):2051–2064. doi: 10.1007/s11356-017-0796-2
  - Juliano C, Magrini GA. Cosmetic Ingredients as Emerging Pollutants of Environmental and Health Concern. A Mini-Review. *Cosmetics.* 2017;4:11–29. doi: 10.3390/cosmetics4020011
  - Bilal M, Mehmood S, Iqbal HMN. The Beast of Beauty: Environmental and Health Concerns of Toxic Components in Cosmetics. *Cosmetics.* 2020;7(1):13–31. doi: 10.3390/cosmetics7010013
  - Brausch JM, Rand GM. A Review of Personal Care Products in the Aquatic Environment: Environmental Concentrations and Toxicity. *Chemosphere.* 2011;82(11):1518–1532. doi: 10.1016/j.chemosphere.2010.11.018
  - Oliveira M, Slezakova K, Delerue-Matos C, Pereira MC, Morais S. Children Environmental Exposure to Particulate Matter and Polycyclic Aromatic Hydrocarbons and Biomonitoring in School Environments: A Review on Indoor and Outdoor Exposure Levels, Major Sources and Health Impacts. *Environ Int.* 2019;124:180–204. doi: 10.1016/j.envint.2018.12.052
  - Tanseverino I, Loos R, Navarro Cuenca A, Marinov D, Lettieri S. State of the art on the contribution of water to antimicrobial resistance. EUR 29592 EN. Luxembourg:

- Publications Office of the European Union; 2018. doi:10.2760/771124
- 25 Rodriguez-Mozaz S, Vaz-Moreira I, Varela Della Giustina S, Llorca M, Barceló D, Schubert S, et al. Antibiotic residues in final effluents of European wastewater treatment plants and their impact on the aquatic environment. *Environ Int.* 2020;140:105733. doi:10.1016/j.envint.2020.105733
- 26 Wotejko E, Jabłońska-Trypuć A, Wydro U, Butarewicz A, Łozowicka B. Soil Biological Activity as an Indicator of Soil Pollution with Pesticides – A Review. *Appl Soil Ecol.* 2020;147:103356. doi: 10.1016/j.apsoil.2019.09.006
- 27 Hussain S, Siddique T, Saleem M, Arshad M, Khalid A. Impact of pesticides on soil microbial diversity, enzymes, and biochemical reactions. In: *Advances in agronomy*. Vol. 102. San Diego: Academic Press; 2009. p. 159-200. doi:10.1016/S0065-2113(09)01005-0
- 28 Köhler H-R, Triebkorn R. Wildlife Ecotoxicology of Pesticides: Can We Track Effects to the Population Level and Beyond? *Science.* 2013;341(6147):759–765. doi: 10.1126/science.1237591
- 29 Rattner BA. History of wildlife toxicology. *Ecotoxicology.* 2009;18:773–83. doi:10.1007/s10646-009-0354-x
- 30 Berny P. Pesticides and the intoxication of wild animals. *J Vet Pharmacol Ther.* 2007;30:93–100. doi: 10.1111/j.1365-2885.2007.00836.x
- 31 Carvalho FP. Pesticides, environment, and food safety. *Food Energy Secur.* 2017;6(2):48–60. doi:10.1002/fes3.108
- 32 George J, Shukla Y. Pesticides and cancer: Insights into toxicoproteomic-based findings. *J Proteomics.* 2011;74(12):2713–2722. doi: 10.1016/j.jprot.2011.09.024
- 33 Bassil KL, Vakili C, Sanborn M, Cole DC, Kaur JS, Kerr JK. Cancer health effects of pesticides. *Can Fam Physician.* 2007;53(10):1704–11. Available from: <https://www.cfp.ca/content/53/10/1704>
- 34 Kumar M, Sarma DK, Shubham S, Kumawat M, Verma V, Prakash A, Tiwari R. Environmental Endocrine-Disrupting Chemical Exposure: Role in Non-Communicable Diseases. *Public Health Front.* 2020;8:553850. doi: 10.3389/fpubh.2020.553850
- 35 Jiang F, Peng Y, Sun Q. Pesticides exposure induced obesity and its associated diseases: recent progress and challenges. *J Future Foods.* 2022;2(2):119–124. doi: 10.1016/j.jfutfo.2022.03.005
- 36 Kim YA, Park JB, Woo MS, Lee SY, Kim HY, Yoo YH. Persistent Organic Pollutant-Mediated Insulin Resistance. *Int J Environ Res Public Health.* 2019;16:448–462. doi: 10.3390/ijerph16030448
- 37 de Araujo JSA, Delgado IF, Paumgartten FJR. Glyphosate and Adverse Pregnancy Outcomes, a Systematic Review of Observational Studies. *BMC Public Health.* 2016;16:472–485. doi: 10.1186/s12889-016-3153-3
- 38 Carrasco Cabrera L, Medina Pastor P. The 2019 European Union Report on Pesticide Residues in Food. *EFSA Journal.* 2021;19(4):6491. doi: 10.2903/j.efsa.2021.6491
- 39 Arutyunov VS, Lisichkin GV. Energy Resources of the 21st Century: Problems and Forecasts. Can Renewable Energy Sources Replace Fossil Fuels? *Russ Chem Rev.* 2017;86(8):777–804. doi: 10.1070/rcr4723
- 40 Barbir F, Veziroğlu TN, Plass HJ. Environmental damage due to fossil fuels use. *Int J Hydrog Energy.* 1990;15(10):739–749. doi: 10.1016/0360-3199(90)90005-J
- 41 Mukhopadhyay K, Forssell O. An empirical investigation of air pollution from fossil fuel combustion and its impact on health in India during 1973-1974 to 1996-1997. *Ecol Econ.* 2005;55(2):235–250. doi:10.1016/j.ecolecon.2004.09.022
- 42 Loppi S, Nascimbene J. Monitoring H<sub>2</sub>S air pollution caused by the industrial exploitation of geothermal energy: The pitfall of using lichens as bioindicators. *Environ Pollut.* 2010;158(8):2635–2639. doi: 10.1016/j.envpol.2010.05.002
- 43 McK. Ellison J, Waller RE. A review of sulphur oxides and particulate matter as air pollutants with particular reference to effects on health in the United Kingdom. *Environ Res.* 1978;16(1-3):302–325. doi: 10.1016/0013-9351(78)90164-0
- 44 Wong T-Y. Smog induces oxidative stress and microbiota disruption. *J Food Drug Anal.* 2017;25(2):235–244. doi: 10.1016/j.jfda.2017.02.003
- 45 Singh A, Agrawal M. Acid rain and its ecological consequences. *J Environ Biol.* 2008;29(1):15–24. <https://pubmed.ncbi.nlm.nih.gov/18831326/>. doi: 10.4103/0254-8704.44191
- 46 Galán I, Tobias A, Banegas JR, Aránguez E. Short-term effects of air pollution on daily asthma emergency room admissions. *Eur Respir J.* 2003;22:802–808. doi: 10.1183/09031936.03.00013003
- 47 Linaker CH, Coggon D, Holgate ST, Clough J, Josephs L, Chauhan AJ, et al. Personal exposure to nitrogen dioxide and risk of airflow obstruction in asthmatic children with upper respiratory infection. *Thorax.* 2000;55(11):930–3. doi:10.1136/thorax.55.11.930
- 48 Kar Kurt O, Zhang J, Pinkerton KE. Pulmonary Health Effects of Air Pollution. *Curr Opin Pulm Med.* 2016;22(2):138–143. doi: 10.1097/MCP.0000000000000248
- 49 Miller KA, Siscovick DS, Sheppard L, Shepherd K, Sullivan JH, Anderson GL, Kaufman JD. Long-Term Exposure to Air Pollution and Incidence of Cardiovascular Events in Women. *N Engl J Med.* 2007;356:447–458. doi: 10.1056/NEJMoa054409
- 50 Schwela D. Air Pollution and Health in Urban Areas. *Rev Environ Health.* 2000;15(1-2):13–42. doi: 10.1515/REVEH.2000.15.1-2.13
- 51 Aribike DS, Usman MA, Oloruntoba MM. Adsorptive desulfurization of diesel using activated sewage sludge: kinetics, equilibrium and thermodynamics studies. *Appl Petrochem Res.* 2020;10:1–12. doi: 10.1007/s13203-019-00239-2
- 52 Song C. An overview of new approaches to deep desulfurization for ultra-clean gasoline, diesel fuel and jet fuel. *Catal Today.* 2003;86(1-4):211–263. doi: 10.1016/S0920-5861(03)00412-7
- 53 ang H, Jiang B, Sun Y, Zhang L, Huang Z, Sun Z, et al. Heterogeneous oxidative desulfurization of diesel fuel catalyzed by mesoporous polyoxometallate-based polymeric hybrid. *J Hazard Mater.* 2017;333:63–72. doi:10.1016/j.jhazmat.2017.03.017
- 54 Ma Y-Q, Liu X-P, Li J-P, Wang R, Yu M-Q. Transition Metal Salts of H4PMo11VO40 for Efficient H<sub>2</sub>S Removal in the Liquid Redox Process. *Chem Pap.* 2017;71:647–652. doi: 10.1007/s11696-016-0064-9
- 55 Zhang J, Zuo W, Tian Y, Yin L, Gong Z, Zhang J. Release of Hydrogen Sulfide during Microwave Pyrolysis of Sewage Sludge: Effect of Operating Parameters and Mechanism. *J Hazard Mater.* 2017;331:117–122. doi: 10.1016/j.jhazmat.2017.02.040
- 56 Jaakkola JJ, Vilkkä V, Marttila O, Jäppinen P, Hahtela T. The South Karelia Air Pollution Study: The effects of malodorous sulfur compounds from pulp mills on respiratory and other symptoms. *Am Rev Respir Dis.* 1990;142(6 Pt 1):1344–1350. doi:10.1164/ajrccm/142.6\_Pt\_1.1344.
- 57 Chaudhari NS, Bhirud AP, Sonawane RS, Nikam LK, Warule SS, Rane VH, et al. Ecofriendly hydrogen production from abundant hydrogen sulfide using solar light-driven hierarchical nanostructured ZnIn<sub>2</sub>S<sub>4</sub> photocatalyst. *Green Chem.* 2011;13(9):2500–2506. doi:10.1039/C1GC15515F.
- 58 Lim E, Mbowe O, Lee ASW, Davis J. Effect of Environmental Exposure to Hydrogen Sulfide on Central Nervous System and Respiratory Function: A Systematic Review of Human Studies. *Int J Occup Environ Health.* 2016;22(1):80–90. doi: 10.1080/10773525.2016.1145881
- 59 European Environment Agency. State of Europe's environment not good: threats to nature and impacts of climate change top challenges. Copenhagen: EEA; 2025. doi:10.2800/3817344

- 60 Cheng X, Bi XT. A review of recent advances in selective catalytic NO<sub>x</sub> reduction reactor technologies. *Particuology*. 2014;16:1–18. doi:10.1016/j.partic.2014.01.006
- 61 Song C. An Overview of New Approaches to Deep Desulfurization for Ultra-Clean Gasoline, Diesel Fuel and Jet Fuel. *Catal Today*. 2003;86(1–4):211–263. doi:10.1016/S0920-5861(03)00412-7
- 62 Ng SJC, Choi AES, Dugos NP, Wan M-W. Driving sustainable solutions: exploring supported-polyoxometalate catalysts for enhanced oxidative desulfurization. *Chem Eng Trans*. 2024;113:79–84. doi:10.3303/CET24113014
- 63 Herrmann S, de Matteis L, de la Fuente JM, Mitchell SG, Streb C. Removal of Multiple Contaminants from Water by Polyoxometalate Supported Ionic Liquid Phases (POM-SILPs). *Angew Chem Int Ed*. 2017;56(6):1667–1670. doi:10.1002/anie.201611072
- 64 Mamun MAA, Yuce MR. Recent Progress in Nanomaterial Enabled Chemical Sensors for Wearable Environmental Monitoring Applications. *Adv Funct Mater*. 2020;30:2005703. doi:10.1002/adfm.202005703
- 65 Hanrahan G, Patila DG, Wang J. Electrochemical sensors for environmental monitoring: design, development and applications. *J Environ Monit*. 2004;6:657–664. doi:10.1039/B403975K
- 66 Justino CILL, Duarte AC, Rocha-Santos TAP. Recent Progress in Biosensors for Environmental Monitoring: A Review. *Sensors*. 2017;17(12):2918–2943. doi:10.3390/s17122918
- 67 Tajik S, Beitollahi H, Nejad FG, Sheikhshoaei I, Nugraha AS, Jang HW, et al. Performance of metal-organic frameworks in the electrochemical sensing of environmental pollutants. *J Mater Chem A*. 2021;9:8195–8220. doi:10.1039/D0TA08344E
- 68 Rassaei L, Marken F, Sillanpää M, Amiri M, Cirtiu CM, Sillanpää M. Nanoparticles in Electrochemical Sensors for Environmental Monitoring. *Trends Analyt Chem*. 2011;30(11):1704–1715. doi:10.1016/j.trac.2011.05.009
- 69 Priyadarshini E, Pradhan N. Gold nanoparticles as efficient sensors in colorimetric detection of toxic metal ions: A review. *Sens Actuators B Chem*. 2017;238:888–902. doi:10.1016/j.snb.2016.06.081
- 70 Horn MR, Singh A, Alomari S, Goberna-Ferrón S, Benages-Vilau R, Chodankar N, et al. Polyoxometalates (POMs): from electroactive clusters to energy materials. *Energy Environ Sci*. 2021;14(4):1652–1700. doi:10.1039/D0EE03407J
- 71 Whittingham MS. Lithium Batteries: 50 Years of Advances to Address the Next 20 Years of Climate Issues. *Nano Lett*. 2020;20(12):8435–8437. doi:10.1021/acs.nanolett.0c04347
- 72 Delmas C. Sodium and Sodium-Ion Batteries: 50 Years of Research. *Adv Energy Mater*. 2018;8(17):1703137. doi:10.1002/aenm.201703137
- 73 Weber AZ, Mench MM, Meyers JP, Ross PN, Gostick JT, Liu Q. Redox Flow Batteries: A Review. *J Appl Electrochem*. 2011;41(10):1137–1164. doi:10.1007/s10800-011-0348-2
- 74 Arico AS, Bruce P, Scrosati B, Tarascon JM, van Schalkwijk W. Nanostructured materials for advanced energy conversion and storage devices. In: *Materials for sustainable energy*. London: Nature Publishing Group; 2010:148–159. doi:10.1142/9789814317665\_0022
- 75 Vannathan AA, Kella T, Shee D, Mal SS. One-Pot Synthesis of Polyoxometalate Decorated Polyindole for Energy Storage Supercapacitors. *ACS Omega*. 2021;6(17):11199–11208. doi:10.1021/acsomega.0c05967
- 76 Herrmann S, Aydemir N, Nägele F, Fantauzzi D, Jacob T, Travas-Sejdic J, et al. Enhanced capacitive energy storage in polyoxometalate-doped polypyrrole. *Adv Funct Mater*. 2017;27(25):1700881. doi:10.1002/adfm.201700881
- 77 Pope MT, Müller A. Polyoxometalate Chemistry From Topology via Self-Assembly to Applications. Dordrecht: Springer; 2001. doi:10.1007/0-306-47625-8
- 78 Streb C. New Trends in Polyoxometalate Photoredox Chemistry: From Photosensitisation to Water Oxidation Catalysis. *Dalton Trans*. 2012;41:1651–1659. doi:10.1039/C1DT11220A
- 79 Coronado E, Giménez-Saiz C, Gómez-García CJ. Recent Advances in Polyoxometalate-Containing Molecular Conductors. *Coord Chem Rev*. 2005;249(17):1776–1796. doi:10.1016/j.ccr.2005.02.017
- 80 López X, Fernández JA, Poblet JM. Redox Properties of Polyoxometalates: New Insights on the Anion Charge Effect. *Dalton Trans*. 2006;9:1162–1167. doi:10.1039/B507599H
- 81 Wang S-S, Yang G-Y. Recent Advances in Polyoxometalate-Catalyzed Reactions. *Chem Rev*. 2015;115(11):4893–4962. doi:10.1021/cr500390v
- 82 Lotfian M, Heravi MM, Mirzaei M, Heidari B. Applications of inorganic-organic hybrid architectures based on polyoxometalates in catalyzed and photocatalyzed chemical transformations. *Appl Organomet Chem*. 2019;33(4):e4808. doi:10.1002/aoc.4808
- 83 Clemente-Juan JM, Coronado E, Gaita-Ariño A. Magnetic Polyoxometalates: From Molecular Magnetism to Molecular Spintronics and Quantum Computing. *Chem Soc Rev*. 2012;41(22):7464–7478. doi:10.1039/C2CS35205B
- 84 Wang S, Sun W, Hu Q, Yan H, Zeng Y. Synthesis and Evaluation of Pyridinium Polyoxometalates as Anti-HIV-1 Agents. *Bioorg Med Chem Lett*. 2017;27(11):2357–2359. doi:10.1016/j.bmcl.2017.04.025
- 85 Bijelic A, Aureliano M, Rompel A. Polyoxometalates as Potential Next-Generation Metallo-drugs in the Combat Against Cancer. *Angew Chem Int Ed Engl*. 2019;58(10):2980–2999. doi:10.1002/anie.201803868
- 86 van Rompuy LS, Parac-Vogt TN. Interactions between Polyoxometalates and Biological Systems: From Drug Design to Artificial Enzymes. *Curr Opin Biotechnol*. 2019;58:92–99. doi:10.1016/j.copbio.2018.11.013
- 87 Bijelic A, Rompel A. The Use of Polyoxometalates in Protein Crystallography – An Attempt to Widen a Well-Known Bottleneck. *Coord Chem Rev*. 2015;299:22–38. doi:10.1016/j.ccr.2015.03.018
- 88 Bijelic A, Rompel A. Polyoxometalates: More than a Phasing Tool in Protein Crystallography. *ChemTexts*. 2018;4(10):1–28. doi:10.1007/s40828-018-0064-1
- 89 Blazevic A, Al-Sayed E, Roller A, Giester G, Rompel A. Tris-Functionalized Hybrid Anderson Polyoxometalates: Synthesis, Characterization, Hydrolytic Stability and Inversion of Protein Surface Charge. *Chem Eur J*. 2015;21(12):4762–4771. doi:10.1002/chem.201405644
- 90 Ji Y, Huang L, Hu J, Streb C, Song Y-F. Polyoxometalate-Functionalized Nanocarbon Materials for Energy Conversion, Energy Storage and Sensor Systems. *Energy Environ Sci*. 2015;8:776–789. doi:10.1039/C4EE03749A
- 91 Long D-L, Tsunashima R, Cronin L. Polyoxometalates: Building Blocks for Functional Nanoscale Systems. *Angew Chem Int Ed*. 2010;49(10):1736–1758. doi:10.1002/anie.200902483
- 92 Pope MT, Kortz U. Polyoxometalates. In: *Encyclopedia of Inorganic and Bioinorganic Chemistry*. Hoboken (NJ): John Wiley & Sons Ltd; 2012. doi:10.1002/9781119951438.eibc0185.pub2
- 93 Al-Sayed E, Rompel A. Lanthanides Singing the Blues: Their Fascinating Role in the Assembly of Gigantic Molybdenum Blue Wheels. *ACS Nanosci Au*. 2022;2(3):179–197. doi:10.1021/acsnanoscienceau.1c00036
- 94 Cherevan AS, Nandan SP, Roger I, Liu R, Streb C. Polyoxometalates on Functional Substrates: Concepts, Synergies, and Future Perspectives. *Adv Sci*. 2020;7:1903511. doi:10.1002/advs.201903511
- 95 Zeng L, Xiao L, Long Y, Shi X. Trichloroacetic acid-modulated synthesis of polyoxometalate@UiO-66 for selective adsorption of cationic dyes. *J Colloid Interface Sci*. 2018;516:274–283. doi:10.1016/j.jcis.2018.01.070
- 96 Zhu T-T, Zhang Z-M, Chen W-L, Liu Z-J, Wang E-B. Encapsulation of tungstophosphoric acid into harmless MIL-101(Fe) for effectively removing cationic dye from aqueous

- solution. *RSC Adv.* 2016;6:81622–81630. doi: 10.1039/C6RA16716K
- 97 Chai D-F, Wang M, Zhang C, Ning F, Xu W, Pang H, et al. A novel 3D POMOF based on dinuclear copper (II)-oxalate complexes and Keggin polyoxoanions with excellent photocatalytic activity. *Inorg Chem Commun.* 2017;83:16–19. doi:10.1016/j.inoche.2017.05.028
- 98 ong B-W, Su Z-H, Zhao Z-F, Zhao W-Q, Ma X-J, Xu Q, et al. A new 3D POMOF with two channels consisting of Wells–Dawson arsenotungstate and  $\{Cl_4Cu_{10}(pz)_{11}\}$  complexes: synthesis, crystal structure, and properties. *New J Chem.* 2018;42:4596–4602. doi:10.1039/C7NJ04854H
- 99 Huo M, Yang W, Zhang H, Zhang L, Liao J, Lin L, et al. A new POM–MOF hybrid microporous material with ultrahigh thermal stability and selective adsorption of organic dyes. *RSC Adv.* 2016;6:111549–111555. doi:10.1039/C6RA10422C
- 100 Mialane P, Mellot-Draznieks C, Gairola P, Duguet M, Benseghir Y, Oms O, et al. Heterogenisation of polyoxometalates and other metal-based complexes in metal–organic frameworks: from synthesis to characterisation and applications in catalysis. *Chem Soc Rev.* 2021;50:6152–6220. doi:10.1039/D0CS00323A
- 101 Samaniyan M, Mirzaei M, Khajavian R, Eshtiagh-Hosseini H, Streb C. Heterogeneous Catalysis by Polyoxometalates in Metal–Organic Frameworks. *ACS Catal.* 2019;9:10174–10191. doi: 10.1021/acscatal.9b03439
- 102 Hoseini A-A, Farhadi S, Zabardasti A. Yolk–shell microspheres assembled from Preyssler-type  $NaP_5W_{30}O_{110}^{14-}$  polyoxometalate and MIL-101(Cr) metal–organic framework: A new inorganic–organic nanohybrid for fast and selective removal of cationic organic dyes from aqueous media. *Appl Organometal Chem.* 2019;33:e4656. doi: 10.1002/aoc.4656
- 103 Jarrah A, Farhadi S. Preparation and characterization of novel polyoxometalate/CoFe<sub>2</sub>O<sub>4</sub>/metal-organic framework magnetic core-shell nanocomposites for the rapid removal of organic dyes from water. *RSC Adv.* 2020;10:39881–39893. doi: 10.1039/D0RA04603E
- 104 Liu X, Luo J, Zhu Y, Yang Y, Yang S. Removal of methylene blue from aqueous solutions by an adsorbent based on metal-organic framework and polyoxometalate. *J Alloys Compd.* 2015;648:986–993. doi: 10.1016/j.jallcom.2015.07.065
- 105 Sun J-W, Yan P-F, An G-H, Sha J-Q, Li G-M, Yang G-Y. Immobilization of Polyoxometalate in the Metal-Organic Framework rht-MOF-1: Towards a Highly Effective Heterogeneous Catalyst and Dye Scavenger. *Sci Rep.* 2016;6:25595. doi: 10.1038/srep25595
- 106 Li D, Guo Y, Hu C, Mao L, Wang E. Photocatalytic degradation of aqueous formic acid over the silica composite films based on lacunary Keggin-type polyoxometalates. *Appl Catal A Gen.* 2002;235:11–20. doi: 10.1016/S0926-860X(02)00238-7
- 107 Maldotti A, Molinari A, Varani G, Lenarda M, Storaro L, Bigi F, et al. Immobilization of  $(n-Bu_4N)_4W_{10}O_{32}$  on Mesoporous MCM-41 and Amorphous Silicas for Photocatalytic Oxidation of Cycloalkanes with Molecular Oxygen. *J Catal.* 2002;209:210–216. doi: 10.1006/jcat.2002.3618
- 108 Zhang H, Wang X, Li N, Xia J, Meng Q, Ding J, et al. Synthesis and characterization of TiO<sub>2</sub>/graphene oxide nanocomposites for photoreduction of heavy metal ions in reverse osmosis concentrate. *RSC Adv.* 2018;8(60):34241–34251. doi:10.1039/C8RA06681G
- 109 Zhang X, Li L, Shao D. Uptake of uranium from wastewater by polyoxometalate modified graphene oxide. *Sep Purif Technol.* 2022;302:122154. doi: 10.1016/j.seppur.2022.122154
- 110 He J, Sun H, Indrawirawan S, Duan X, Tade MO, Wang S. Novel polyoxometalate@g-C<sub>3</sub>N<sub>4</sub> hybrid photocatalysts for degradation of dyes and phenolics. *J Colloid Interface Sci.* 2015;456:15–21. doi: 10.1016/j.jcis.2015.06.003
- 111 Ghali M, Brahmi C, Bentifa M, Dumur F, Duval S, Simonnet-Jégat C, et al. New hybrid polyoxometalate/polymer composites for photodegradation of eosin dye. *J Polym Sci Part A Polym Chem.* 2019;57:1538–1549. doi:10.1002/pola.29416
- 112 Heravi MM, Mirzei M. Polyoxometalate-Based Hybrids and their Applications. 1st ed. Elsevier; 2023. Paperback ISBN: 9780323917315, eBook ISBN: 9780323983464
- 113 Uchida S. Frontiers and progress in cation-uptake and exchange chemistry of polyoxometalate-based compounds. *Chem Sci.* 2019;10:7670–7679. doi: 10.1039/C9SC02823D
- 114 Kandasamy B, Sudmeier T, Ayass WW, Lin Z, Feng Q, Bassil BS, et al. Selective Rb<sup>+</sup> vs. K<sup>+</sup> Guest Incorporation in Wheel-Shaped 27-Tungsto-3-Arsenate(III) Host,  $[M\langle(\beta-As^{III}W_8O_{30})(WO(H_2O))_3\rangle]^{14-}$  (M= K, Rb). *Eur J Inorg Chem.* 2019;(3–4):502–505. doi: 10.1002/ejic.201800788
- 115 Kawahara R, Uchida S, Mizuno N. Redox-Induced Reversible Uptake-Release of Cations in Porous Ionic Crystals Based on Polyoxometalate: Cooperative Migration of Electrons with Alkali Metal Ions. *Chem Mater.* 2015;27(6):2092–2099. doi: 10.1021/cm504526z
- 116 Pei X, Wang R. Desulfurization Performance of Rare Earth Mono-Substituted Heteropoly Compounds. *Aerosol Air Qual Res.* 2019;19(12):2888–2898. doi: 10.4209/aaqr.2019.10.0540
- 117 Dehghani R, Aber S, Mahdizadeh F. Polyoxometalates and Their Composites as Photocatalysts for Organic Pollutants Degradation in Aqueous Media-A Review. *CLEAN Soil Air Water.* 2018;46(12):1800413. doi: 10.1002/clen.201800413
- 118 Lindqvist I. On the Structure of the Paratungstate Ion. *Acta Crystallogr.* 1952;5:667–670. doi: 10.1107/S0365110X52001817
- 119 Saddington K, Cahn RW. The Formula of Sodium Paratungstate. *J Chem Soc.* 1950:3526–3529. doi: 10.1039/JR9500003526
- 120 Shimao E. Structure of the Mo<sub>7</sub>O<sub>24</sub><sup>6-</sup> Ion in a Crystal of Ammonium Heptamolybdate Tetrahydrate. *Nature.* 1967;214:170–171. doi: 10.1038/214170a0
- 121 Sturdivant JH. The Formula of Ammonium Paramolybdate. *J Am Chem Soc.* 1937;59(4):630–631. doi: 10.1021/ja01283a010
- 122 Fuchs J, Hartl H. Anion Structure of Tetrabutylammonium Octamolybdate  $[N(C_4H_9)_4]_4Mo_8O_{26}$ . *Angew Chem Int Ed Engl.* 1976;15:375–376. doi: 10.1002/anie.197603751
- 123 Bridgeman AJ. The Electronic Structure and Stability of the Isomers of Octamolybdate. *J Phys Chem A.* 2002;106(50):12151–12160. doi: 10.1021/jp027037l
- 124 Fuchs J, Hartl H, Schiller W, Gerlach U. Die Kristallstruktur des Tributylammoniumdekawolframats  $[(C_4H_9)_2NH]_4W_{10}O_{23}$ . *Acta Cryst B.* 1976;32:740–749. doi: 10.1107/S0567740876003907
- 125 Chemseddine A, Sanchez C, Livage J, Launay JP, Fournier M. Electrochemical and photochemical reduction of decatungstate: a reinvestigation. *Inorg Chem.* 1984;23(17):2609–2613. doi: 10.1021/ic00185a014
- 126 Evans HT Jr. The Molecular Structure of the Isopoly Complex Ion, Decavanadate ( $V_{10}O_{28}^{6-}$ ). *Inorg Chem.* 1966;5(6):967–977. doi: 10.1021/ic50040a004
- 127 Rossotti FJC, Rossotti H. Equilibrium Studies of Polyanions. *Acta Chem Scand.* 1956;10(6):957–984. [http://actachemscand.org/pdf/acta\\_vol\\_10\\_p0957-0984.pdf](http://actachemscand.org/pdf/acta_vol_10_p0957-0984.pdf)
- 128 Keggin JF. Structure of the Molecule of 12-Phosphotungstic Acid. *Nature.* 1933;131:908–909. doi: 10.1038/131908b0
- 129 Linz A. Preparation of Phosphomolybdic Acid from Phosphoric Acid and Pure Molybdic Acid. *Ind Eng Chem Anal Ed.* 1943;15(7):459. doi: 10.1021/i560119a015

- 130 Khajavian R, Jodaian V, Taghipour F, Mague JT, Mirzaei M. Roles of Organic Fragments in Redirecting Crystal/Molecular Structures of Inorganic–Organic Hybrids Based on Lacunary Keggin-Type Polyoxometalates. *Molecules*. 2021;26:5994–6020. doi: 10.3390/molecules26195994
- 131 Dawson B. The Structure of the 9(18)-Heteropoly Anion in Potassium 9(18)-Tungstophosphate,  $K_6(P_2W_{18}O_{62}) \cdot 14H_2O$ . *Acta Crystallogr*. 1953;6:113–126. doi: 10.1107/S0365110X53000466
- 132 Kherrmann F. Zur Kenntnis der komplexen anorganischen Säuren. III. Abhandlung. *Z Anorg Allg Chem*. 1892;1:423–441. doi: 10.1002/zaac.18920010139
- 133 Evans HT. The Crystal Structures Of Ammonium And Potassium Molybdatellurates. *J Am Chem Soc*. 1948;70(3):1291–1292. doi: 10.1021/ja01183a521
- 134 Meloche VW, Woodstock W. The Preparation And Study Of Two Ammonium Molybdatellurates. *J Am Chem Soc*. 1929;51(1):171–174. doi: 10.1021/ja01376a020
- 135 Alizadeh MH, Harmalkar SP, Jeannin Y, Martin-Frere J, Pope MT. A heteropolyanion with fivefold molecular symmetry that contains a nonlabile encapsulated sodium ion. The structure and chemistry of  $[NaP_5W_{30}O_{110}]^{14-}$ . *J Am Chem Soc*. 1985;107:2662–2669. doi: 10.1021/ja00295a019
- 136 Hedman B, Strandberg R. Multicomponent polyanions. 19. The molecular and crystal structure of  $Na_5HM_5P_2O_{23}(H_2O)_{11}$ , a superstructure with sodium-coordinated monohydrogenpentamolybdodiphosphate anions. *Acta Cryst B*. 1979;35:278–284. doi: 10.1107/S0567740879003356
- 137 Pettersson L. Multicomponent Polyanions. I. On Yellow and Colorless Molybdophosphates in 3 M  $Na(ClO_4)$ . A Determination of Formation Constants for Three Colourless Pentamolybdodiphosphates in the pH-range 3–9. *Acta Chem Scand*. 1971;25:1959–1974. doi: 10.3891/acta.chem.scand.25-1959
- 138 Weakley TJR, Evans HT, Showell JS, Tourné GF, Tourné CM. 18-Tungstotetracobalto(II)Diphosphate and Related Anions: A Novel Structural Class of Heteropolyanions. *J Chem Soc Chem Commun*. 1973;(4):139–140. doi: 10.1039/C39730000139
- 139 Evans HT, Tourné CM, Tourné GF, Weakley TJR. X-Ray crystallographic and tungsten-183 nuclear magnetic resonance structural studies of the  $[M_4(H_2O)_2(XW_9O_{34})_2]^{10-}$  heteropolyanions (M = CoII or Zn, X = P or As). *J Chem Soc Dalton Trans*. 1986;(12):2699–2705. doi: 10.1039/DT9860002699
- 140 Müller A, Roy S. En route from the mystery of molybdenum blue via related manipulatable building blocks to aspects of materials science. *Coord Chem Rev*. 2003;245(1–2):153–166. doi: 10.1016/S0010-8545(03)00110-3
- 141 Müller A, Peters F, Pope MT, Gatteschi D. Polyoxometalates: Very Large Clusters–Nanoscale Magnets. *Chem Rev*. 1998;98(1):239–272. doi: 10.1021/cr9603946
- 142 Jeannin YP. The Nomenclature of Polyoxometalates: How To Connect a Name and a Structure. *Chem Rev*. 1998;98(1):51–76. doi: 10.1021/cr960397i
- 143 Gumerova NI, Romel A. Speciation atlas of polyoxometalates in aqueous solutions. *Sci Adv*. 2023;9(25):eadi0814. doi:10.1126/sciadv.adi0814
- 144 Zdrnja M, Gumerova NI, Rompel A. Exploring polyoxometalate speciation: the interplay of concentration, ionic strength, and buffer composition. *Front Chem Biol*. 2024;3:1444359. doi:10.3389/fchbi.2024.1444359
- 145 Gregorovic I, Gumerova NI, Rompel A. Speciation atlas of polyoxometalates in aqueous solution (Part II): molybdenum browns. *Sci Adv*. 2025;11(44):eaea1910. doi:10.1126/sciadv.aea1910
- 146 Guo Y, Hu C, Jiang S, Guo C, Yang Y, Wang E. Heterogeneous photodegradation of aqueous hydroxy butanedioic acid by microporous polyoxometalates. *Appl Catal B Environ*. 2002;36:9–17. doi: 10.1016/S0926-3373(01)00260-0
- 147 Chen X, Souvanhthong B, Wang H, Zheng H, Wang X, Huo M. Polyoxometalate-based Ionic liquid as thermoregulated and environmentally friendly catalyst for starch oxidation. *Appl Catal B Environ*. 2013;138:161–166. doi: 10.1016/j.apcatb.2013.02.028
- 148 Rezvani MA, Aghmasheh M. Synthesis of t-B.PWFe/NiO nanocomposite as an efficient and heterogeneous green nanocatalyst for catalytic oxidative-extractive desulfurization of gasoline. *Environ Prog Sustain Energy*. 2021;40:e13616. doi: 10.1002/ep.13616
- 149 Xun S, Ti Q, Wu L, He M, Wang C, Chen L, et al. Few layer g-C<sub>3</sub>N<sub>4</sub> dispersed quaternary phosphonium ionic liquid for highly efficient catalytic oxidative desulfurization of fuel. *Energy Fuels*. 2020;34(10):12379–12387. doi:10.1021/acs.energyfuels.0c02357
- 150 Wang P, Jiang L, Zou X, Tan H, Zhang P, Li J, et al. Confining polyoxometalate clusters into porous aromatic framework materials for catalytic desulfurization of dibenzothiophene. *ACS Appl Mater Interfaces*. 2020;12(23):25910–25919. doi:10.1021/acsami.0c05392
- 151 Li J, Yang Z, Hu G, Zhao J. Heteropolyacid supported MOF fibers for oxidative desulfurization of fuel. *Chem Eng J*. 2020;388:124325. doi: 10.1016/j.cej.2020.124325
- 152 Zhao XY, Wang X, Zhao Y, Sun H, Tan H, Qiu T, et al. Polyoxometalates-doped TiO<sub>2</sub>/Ag hybrid heterojunction: removal of multiple pollutants and mechanism investigation. *Environ Sci Nano*. 2021;8:3855–3864. doi:10.1039/D1EN00827G
- 153 Chen K, She S, Zhang J, Bayaguud A, Wei Y. Label-free colorimetric detection of mercury via Hg<sup>2+</sup> ions-accelerated structural transformation of nanoscale metal-oxo clusters. *Scientific Reports*. 2015;5:16316. doi:10.1038/srep16316
- 154 Sun J-W, Yan P-F, An G-H, Sha J-Q, Li G-M, Yang G-Y. Immobilization of polyoxometalate in the metal-organic framework rht-MOF-1: towards a highly effective heterogeneous catalyst and dye scavenger. *Scientific Reports*. 2016;6:25595. doi:10.1038/srep25595
- 155 Song H, Guo M-S, Wang J-F, Liu Y-Q, Bi H-X, Du J, et al. Reduced phosphomolybdate as photoassisted electrochemical crystalline sensor for trace Cr(VI) detection. *Polyoxometalates*. 2024;3(4):9140065. doi:10.26599/POM.2024.9140065
- 156 Li S, Zheng Y, Liu G-C, Li X-H, Zhang Z, Wang X-L. New two-fold interpenetrating 3D polyoxovanadate-based metal-organic framework as bifunctional catalyst for the removal of 2-chloroethyl ethyl sulfide and phenolic compounds. *Polyoxometalates*. 2024;3(3):9140061. doi:10.26599/POM.2024.9140061
- 157 Dai Y-C, Zhang S-Y, Xiao X-X, Li M-J, Liu J-C, Chen L-J, et al. A double-tartrate-bridged deca-nuclearity europium-tungsten cluster embedded selenotungstate and its selective optical sensing of o-nitrophenol. *Polyoxometalates*. 2023;2(4):9140041. doi:10.26599/POM.2023.9140041
- 158 Xia Z, Wang L, Zhang Q, Li F, Xu L. Fast degradation of phenol over porphyrin–polyoxometalate composite photocatalysts under visible light. *Polyoxometalates*. 2022;1(1):9140001. doi:10.26599/POM.2022.9140001
- 159 Liang R, Huang R, Ying S, Wang X, Yan G, Wu L. Facile in situ growth of highly dispersed palladium on phosphotungstic-acid-encapsulated MIL-100(Fe) for the degradation of pharmaceuticals and personal care products under visible light. *Nano Res*. 2018;11:1109–1123. doi:10.1007/s12274-017-1730-0
- 160 Chen K, Bayaguud A, Li H, Chu Y, Zhang H, Jia H, et al. Improved peroxidase-mimic property: sustainable, high-efficiency interfacial catalysis with H<sub>2</sub>O<sub>2</sub> on the surface of vesicles of hexavanadate–organic hybrid surfactants. *Nano Res*. 2018;11:1313–1321. doi:10.1007/s12274-017-1746-5
- 161 Mohamed AM, Abbas WA, Khedr GE, Abass W, Allam NK. Computational and experimental elucidation of the boosted

- 1 stability and antibacterial activity of ZIF-67 upon optimized  
2 encapsulation with polyoxometalates. *Scientific Reports*.  
3 2022;12:15989. doi:10.1038/s41598-022-20392-4.
- 4 162 Ma X-Y, Bi H-X, Zhang X-J, Du J, Ma Y-Y, Han Z-G. Effect of  
5 bridging units on the detection performance of Cd(P<sub>4</sub>Mo<sub>6</sub>)<sub>2</sub>-  
6 based electrochemical sensors for trace chromium(VI) and  
7 tetracycline. *Polyoxometalates*. 2025;4(2):9140090.  
8 doi:10.26599/POM.2025.9140090
- 9 163 Hao Y, Ji T, Zhang J, Chen W. Triboelectric nanogenerator  
10 based on changing the nanomorphology of  
11 polyoxometalates for gait monitoring of teenagers. *Nano  
Res.* 2025;18(2):94907192.  
doi:10.26599/NR.2025.94907192
- 12 164 Srivastav AL, Ranjan M. Chapter 1 - Inorganic Water  
13 Pollutants. In: Inorganic Pollutants in Water. 1st ed. Elsevier;  
14 2020:1–15. doi: 10.1016/B978-0-12-818965-8.00001-9
- 15 165 Wasewar KL, Singh S, Kansal SK. Chapter 13 - Process  
16 Intensification of Treatment of Inorganic Water Pollutants.  
17 In: Inorganic Pollutants in Water. 1st ed. Elsevier;  
18 2020:245–271. doi: 10.1016/B978-0-12-818965-8.00013-5
- 19 166 D'Cruz B, Amin MO, Al-Hetlani E. Polyoxometalate-Based  
20 Materials for the Removal of Contaminants from  
21 Wastewater: A Review. *Ind Eng Chem Res.*  
22 2021;60(30):10960–10977. doi: 10.1021/acs.iecr.1c02007
- 23 167 Xu F-L, Jorgensen SE, Shimizu Y, Silow E. Editorial  
24 Persistent Organic Pollutants in Fresh Water Ecosystems. *Sci  
World J.* 2013;2013:303815. doi: 10.1155/2013/303815
- 25 168 Bolisetty S, Peydayesh M, Mezzenga R. Sustainable  
26 technologies for water purification from heavy metals:  
27 review and analysis. *Chem Soc Rev.* 2019;48:463–487. doi:  
28 10.1039/C8CS00493E
- 29 169 Hu M, Xu Y. Visible light induced degradation of  
30 chlorophenols in the presence of H<sub>2</sub>O<sub>2</sub> and iron substituted  
31 polyoxotungstate. *Chem Eng J.* 2014;246:299–305. doi:  
32 10.1016/j.cej.2014.02.072
- 33 170 Taghdiri M, Saadatjou N, Zamani N, Farrokhi R.  
34 Heterogeneous degradation of precipitated hexamine from  
35 wastewater by catalytic function of silicotungstic acid in the  
36 presence of H<sub>2</sub>O<sub>2</sub> and H<sub>2</sub>O<sub>2</sub>/Fe<sup>2+</sup>. *J Hazard Mater.*  
37 2013;246:206–212. doi: 10.1016/j.jhazmat.2012.12.029
- 38 171 Lan J, Wang Y, Huang B, Xiao Z, Wu P. Application of  
39 polyoxometalates in photocatalytic degradation of organic  
40 pollutants. *Nanoscale Adv.* 2021;3:4646–4658. doi:  
41 10.1039/D1NA00408E
- 42 172 Wang Y, Fang G, Ordonsky VV, Khodakov AY.  
43 Polyoxometalate photocatalysts: solar-driven activation of  
44 small molecules for energy conversion and greenhouse gas  
45 valorization. *Chem Commun.* 2025;61:10630–10642. doi:  
46 10.1039/D5CC01494H
- 47 173 Lu N, Wang Y, Ning S, Zhao W, Qian M, Ma Y, et al. Design  
48 of plasmonic Ag-TiO<sub>2</sub>/H<sub>3</sub>PW<sub>12</sub>O<sub>40</sub> composite film with  
49 enhanced sunlight photocatalytic activity towards o-  
50 chlorophenol degradation. *Sci Rep.* 2017;7:17298.  
51 doi:10.1038/s41598-017-17221-4
- 52 174 Tahmasebi M, Mirzei M, Frontera A. Noble metals in  
53 polyoxometalates. *Inorg Chim Acta.* 2021;523:120410. doi:  
54 10.1016/j.ica.2021.120410
- 55 175 Fashapoyeh MA, Mirzaei M, Eshtiagh-Hosseini H,  
56 Rajagopal A, Lechner M, Liu R, et al. Photochemical and  
57 electrochemical hydrogen evolution reactivity of lanthanide-  
58 functionalized polyoxotungstates. *Chem Commun.*  
59 2018;54:10427–10430. doi: 10.1039/C8CC06334F
- 60 176 Li K, Guo Y, Ma F, Li H, Chen L, Guo Y. Design of ordered  
mesoporous H<sub>3</sub>PW<sub>12</sub>O<sub>40</sub>-titania materials and their  
photocatalytic activity to dye methyl orange degradation.  
*Catal Commun.* 2010;11:839–843. doi:  
10.1016/j.catcom.2010.03.004
- 177 Liu Y, Tang C, Cheng M, Chen M, Chen S, Lei L, et al.  
Polyoxometalate@Metal-Organic Framework Composites as  
Effective Photocatalysts. *ACS Catal.* 2021;11(21):13374–13396. doi: 10.1021/acscatal.1c03866
- 178 Liang R, Hu A, Hatat-Fraile M, Zhou N. Fundamentals on  
Adsorption, Membrane Filtration, and Advanced Oxidation  
Processes for Water Treatment. In: Nanotechnology for  
Water Treatment and Purification. Cham: Springer;  
2014:1–45. doi: 10.1007/978-3-319-06578-6\_1
- 179 Yao L, Long Z, Chen Z, Cheng Q, Liao Y, Tian M. Property  
Characterization and Mechanism Analysis of  
Polyoxometalates-Functionalized PVDF Membranes by  
Electrochemical Impedance Spectroscopy. *Membranes*.  
2020;10:214. doi: 10.3390/membranes10090214
- 180 Yao L, Lua SK, Zhang L, Wang R, Dong Z. Dye removal by  
surfactant encapsulated polyoxometalates. *J Hazard Mater.*  
2014;280:428–435. doi: 10.1016/j.jhazmat.2014.08.026
- 181 Heravi MM, Mirzaei M. Reactivity and stability synergism  
directed by the electron transfer between polyoxometalates  
and metal-organic frameworks. *Catal Sci Technol.*  
2023;13(14):4162–4172. doi:10.1039/D3CY00569K
- 182 Du J, Ma Y, Li Y-G. Unraveling photocatalytic electron  
transfer mechanism in polyoxometalate-encapsulated  
metal-organic frameworks for high-efficient CO<sub>2</sub> reduction  
reaction. *Appl Catal B Environ.* 2022;318:121850. doi:  
10.1016/j.apcatb.2022.121850
- 183 Galiano F, Mancuso R, Carraro M, Bundschuh J, Hoinkis J,  
Bonchio M, et al. A polyoxometalate-based self-cleaning  
smart material with oxygenic activity for water remediation  
with membrane technology. *Appl Mater Today.*  
2021;23:101002. doi: 10.1016/j.apmt.2021.101002
- 184 Zhang M-M, Li A-K, Tang M-J, He Q-Y, Peng Y-H, Fan R-J,  
et al. Constructing polyoxometalates-based electrocatalytic  
nanofiltration membranes for nitrite removal. *J Membr Sci.*  
2024;699:122668. doi: 10.1016/j.memsci.2024.122668
- 185 Liao Z, Gao T, Zhang J, Wu Q, Shi J, Yang Z, et al.  
Polyoxometalates decoration combining with solvent  
activation for enhanced separation performance of  
nanofiltration membrane. *J Membr Sci.* 2024;706:122964.  
doi: 10.1016/j.memsci.2024.122964
- 186 Bonchio M, Carraro M, Scorrano G, Fontananova E, Drioli  
E. Heterogeneous Photooxidation of Alcohols in Water by  
Photocatalytic Membranes Incorporating Decatungstate.  
*Adv Synth Catal.* 2003;345:1119–1126. doi:  
10.1002/adsc.200303076
- 187 Fontananova E, Donato L, Drioli E, Lopez LC, Favia P,  
d'Agostino R. Heterogenization of Polyoxometalates on the  
Surface of Plasma-Modified Polymeric Membranes. *Chem  
Mater.* 2006;18:1561–1568. doi: 10.1021/cm051739g
- 188 Romanenko I, Lechner M, Wendler F, Hörenz C, Streb C,  
Schacher FH. POMbranes: polyoxometalate-functionalized  
block copolymer membranes for oxidation catalysis. *J Mater  
Chem A.* 2017;5:15789–15796. doi: 10.1039/C7TA03220J
- 189 Yao L, Zhang L-Z, Wang R, Loh CH, Dong Z-L. Fabrication  
of catalytic membrane contactors based on  
polyoxometalates and polyvinylidene fluoride intended for  
degrading phenol in wastewater under mild conditions. *Sep  
Purif Technol.* 2013;118:162–169. doi:  
10.1016/j.seppur.2013.06.029
- 190 Yao L, Zhang L, Wang R, Chou S, Dong Z. A new integrated  
approach for dye removal from wastewater by  
polyoxometalates functionalized membranes. *J Hazard  
Mater.* 2016;301:462–470. doi:  
10.1016/j.jhazmat.2015.09.027
- 191 Giannakas AE, Antonopoulou M, Daikopoulos C,  
Deligiannakis Y, Konstantinou I. Characterization and  
Catalytic Performance of B-Doped, B-N Co-Doped and B-N-F  
Tri-Doped TiO<sub>2</sub> towards Simultaneous Cr(VI) Reduction and  
Benzoic Acid Oxidation. *Appl Catal B Environ.*  
2016;184:44–54. doi: 10.1016/j.apcatb.2015.11.009
- 192 McEvoy JG, Zhang Z. Synthesis and Characterization of  
Magnetically Separable Ag/AgCl-Magnetic Activated Carbon  
Composites for Visible Light Induced Photocatalytic  
Detoxification and Disinfection. *Appl Catal B Environ.*  
2014;160:267–278. doi: 10.1016/j.apcatb.2013.07.062

- 193 Gong K, Wang W, Yan J, Han Z. Highly Reduced Molybdophosphate as a Noble-Metal-Free Catalyst for the Reduction of Chromium Using Formic Acid as a Reducing Agent. *J Mater Chem A*. 2015;3(11):6019–6027. doi: 10.1039/C4TA06830K
- 194 Gong K, Liu Y, Wang W, Fang T, Zhao C, Han Z, Zhai X. Reduced Phosphomolybdates as Molecular Catalysts for Hexavalent Chromium Reduction. *Eur J Inorg Chem*. 2015;32:5351–5356. doi: 10.1002/EJIC.201500883
- 195 Shi H-F, Yan G, Zhang Y, Tan H-Q, Zhou W-Z, Ma Y-Y, et al. Ag/Ag<sub>x</sub>H<sub>3-x</sub>PMo<sub>12</sub>O<sub>40</sub> nanowires with enhanced visible-light-driven photocatalytic performance. *ACS Appl Mater Interfaces*. 2017;9(1):422–30. doi:10.1021/acsami.6b13009
- 196 Daupor H, Wongnawa S. Urchinlike Ag/AgCl Photocatalyst: Synthesis, Characterization, and Activity. *Appl Catal A Gen*. 2014;473:59–69. doi: 10.1016/J.APCATA.2013.12.036
- 197 Wang D, Duan Y, Luo Q, Li X, Bao L. Visible Light Photocatalytic Activities of Plasmonic Ag/AgBr Particles Synthesized by a Double Jet Method. *Desalination*. 2011;270(1-3):174–180. doi: 10.1016/J.DESAL.2010.11.042
- 198 Wan J, Liu E, Fan J, Hu X, Sun L, Tang C, et al. In-situ synthesis of plasmonic Ag/Ag<sub>3</sub>PO<sub>4</sub> tetrahedron with exposed {111} facets for high visible-light photocatalytic activity and stability. *Ceram Int*. 2015;41(5):6933–40. doi:10.1016/j.ceramint.2015.01.148
- 199 Zhao W, Guo Y, Faiz Y, Yuan WT, Sun C, Wang SM, et al. Facile in-suit synthesis of Ag/AgVO<sub>3</sub> one-dimensional hybrid nanoribbons with enhanced performance of plasmonic visible-light photocatalysis. *Appl Catal B Environ*. 2015;163:288–97. doi:10.1016/j.apcatb.2014.08.015
- 200 Zhao X, Zhang Y, Zhao Y, Tan H, Zhao Z, Shi H, et al. Ag<sub>x</sub>H<sub>3-x</sub>PMo<sub>12</sub>O<sub>40</sub>/Ag nanorods/g-C<sub>3</sub>N<sub>4</sub> 1D/2D Z-scheme heterojunction for highly efficient visible-light photocatalysis. *Dalton Trans*. 2019;48(19):6484–91. doi:10.1039/C9DT00744J
- 201 Zhang H, Yang J, Liu Y-Y, Song S-Y, Liu X-L, Ma J-F. Visible Light Photodegradation of Organic Dyes, Reduction of CrVI and Catalytic Oxidative Desulfurization by a Class of Polyoxometalate-Based Inorganic-Organic Hybrid Compounds. *Dyes Pigm*. 2016;133:189–200. doi: 10.1016/j.dyepig.2016.05.051S.
- 202 Buffet-Bataillon S, Tattevin P, Bonnaure-Mallet M, Jolivet-Gougeon A. Emergence of Resistance to Antibacterial Agents: The Role of Quaternary Ammonium Compounds—a Critical Review. *Int J Antimicrob Agents*. 2012;39(5):381–389. doi: 10.1016/j.ijantimicag.2012.01.011
- 203 Shakeela K, Rao GR. Thermoreversible, Hydrophobic Ionic Liquids of Keggin-Type Polyanions and Their Application for the Removal of Metal Ions from Water. *ACS Appl Nano Mater*. 2018;1(9):4642–4651. doi: 10.1021/acsanm.8b00920
- 204 Kitson PJ, Symes MD, Dragone V, Cronin L. Combining 3D Printing and Liquid Handling to Produce User-Friendly Reactionware for Chemical Synthesis and Purification. *Chem Sci*. 2013;4(8):3099–3103. doi: 10.1039/C3SC51253C
- 205 Ji Y, Ma Y, Ma Y, Asenbauer J, Passerini S, Streb C. Water Decontamination by Polyoxometalate-Functionalized 3D-Printed Hierarchical Porous Devices. *Chem Commun*. 2018;54(24):3018–3021. doi: 10.1039/C8CC00821C
- 206 Mitchell SG, Streb C, Miras HN, Boyd T, Long D-L, Cronin L. Face-Directed Self-Assembly of an Electronically Active Archimedean Polyoxometalate Architecture. *Nat Chem*. 2010;2:308–312. doi: 10.1038/nchem.581
- 207 Wang S, Geng X, Zhao Z, Zhang M, Song Y, Sun K, et al. Ammoniated-driven green synthesis of charged polyoxometalate supported ionic liquids for exceptional heavy metal remediation in actual industrial wastewater. *Water Res*. 2025;272:122939. doi:10.1016/j.watres.2024.122939
- 208 Zou F, Yu R, Li R, Li W. Microwave-assisted Synthesis of HKUST-1 and Functionalized HKUST-1-@ H<sub>3</sub>PW<sub>12</sub>O<sub>40</sub>: Selective Adsorption of Heavy Metal Ions in Water Analyzed with Synchrotron Radiation. *ChemPhysChem*. 2013;14(12):2825–2832. doi: 10.1002/cphc.201300215
- 209 Zhang H, Xue J, Hu N, Sun J, Ding D, Wang Y, et al. Selective removal of U(VI) from low concentration wastewater by functionalized HKUST-1@H<sub>3</sub>PW<sub>12</sub>O<sub>40</sub>. *J Radioanal Nucl Chem*. 2016;308:865–75. doi:10.1007/s10967-015-4603-6
- 210 Frost RL, Čejka J, Dickfos MJ. Raman Spectroscopic Study of the Uranyl Minerals Vanmeersscheite U(OH)<sub>4</sub>[(UO<sub>2</sub>)<sub>3</sub>(PO<sub>4</sub>)<sub>2</sub>(OH)<sub>2</sub>·4H<sub>2</sub>O and Arsenouranylite Ca(UO<sub>2</sub>)<sub>2</sub>[(UO<sub>2</sub>)<sub>3</sub>(AsO<sub>4</sub>)<sub>2</sub>(OH)<sub>2</sub>·(OH)<sub>2</sub>·6H<sub>2</sub>O. *Spectrochim Acta A Mol Biomol Spectrosc*. 2009;71(5):1799–1803. doi: 10.1016/j.saa.2008.06.041
- 211 Shao D, Li Y, Wang X, Hu S, Wen J, Xiong J, et al. Phosphate-functionalized polyethylene with high adsorption of uranium(VI). *ACS Omega*. 2017;2(7):3267–75. doi:10.1021/acsomega.7b00375
- 212 Han X, Wang Y, Cao X, Dai Y, Liu Y, Dong Z, et al. Adsorptive performance of ship-type nano-cage polyoxometalates for U(VI) in aqueous solution. *Appl Surf Sci*. 2019;484:1035–40. doi:10.1016/j.apsusc.2019.04.121
- 213 Seino S, Kawahara R, Ogasawara Y, Mizuno N, Uchida S. Reduction-Induced Highly Selective Uptake of Cesium Ions by an Ionic Crystal Based on Silicododecamolybdate. *Angew Chem Int Ed*. 2016;55(12):4055–4059. doi: 10.1002/ange.201511633
- 214 Hitose S, Uchida S. Rapid Uptake/Release of Cs<sup>+</sup> in Isostructural Redox-Active Porous Ionic Crystals with Large-Molecular-Size and Easily Reducible Dawson-Type Polyoxometalates as Building Blocks. *Inorg Chem*. 2018;57(9):4833–4836. doi: 10.1021/acs.inorgchem.8b00801
- 215 Liu X, Gong W, Luo J, Zou C, Yang Y, Yang S. Selective adsorption of cationic dyes from aqueous solution by polyoxometalate-based metal-organic framework composite. *Appl Surf Sci*. 2016;362:517–524. doi: 10.1016/j.apsusc.2015.11.151
- 216 Sabarinathan C, Karuppasamy P, Vijayakumar C, Arumuganathan T. Development of methylene blue removal methodology by adsorption using molecular polyoxometalate: Kinetics, Thermodynamics and Mechanistic Study. *Microchem J*. 2019;146:315–326. doi: 10.1016/j.microc.2019.01.015
- 217 Bai L, Pan X, Guo R, Linghu X, Shu Y, Wu Y, et al. Sunlight-driven photocatalytic degradation of organic dyes in wastewater by chemically fabricated ZnO/Cs<sub>4</sub>SiW<sub>12</sub>O<sub>40</sub> nanoheterojunction. *Appl Surf Sci*. 2022;599:153912. doi:10.1016/j.apsusc.2022.153912
- 218 Wang R, Liu Y, Zuo P, Zhang Z, Lei N, Liu Y. Phthalocyanine-sensitized evolution of hydrogen and degradation of organic pollutants using polyoxometalate photocatalysts. *Environ Sci Pollut Res*. 2020;27:18831–18842. doi: 10.1007/s11356-020-08425-9
- 219 Yang Z, Gao S, Li H, Cao R. Synthesis and visible light photocatalytic properties of polyoxometalate-thionine composite films immobilized on porous TiO<sub>2</sub> microspheres. *J Colloid Interface Sci*. 2012;375(1):172–179. doi: 10.1016/j.jcis.2012.02.043
- 220 Qi L, Gong Y, Fang M, Jia Z, Cheng N, Yu L. Surface-Active Ionic-Liquid-Encapsulated Polyoxometalate Nanospheres: Construction, Self-Assembly, Adsorption Behavior, and Application for Dye Removal. *ACS Appl Nano Mater*. 2020;3(1):375–383. doi: 10.1021/acsanm.9b02012
- 221 Bi B, Xu L, Xu B, Liu X. Heteropoly blue-intercalated layered double hydroxides for cationic dye removal from aqueous media. *Appl Clay Sci*. 2011;54:242–247. doi: 10.1016/j.clay.2011.09.003
- 222 Lesbani A, Taher T, Rahayu Palapa N, Mohadi R, Rachmat A, Mardiyanto R. Preparation and utilization of Keggin-type polyoxometalate intercalated Ni-Fe layered double hydroxides for enhanced adsorptive removal of cationic dye. *SN Appl Sci*. 2020;2:470. doi: 10.1007/s42452-020-2300-8

- 223 Lei P, Chen C, Yang J, Ma W, Zhao J, Zang L. Degradation of Dye Pollutants by Immobilized Polyoxometalate with H<sub>2</sub>O<sub>2</sub> under Visible-Light Irradiation. *Environ Sci Technol*. 2005;39(21):8466–8474. doi: 10.1021/es050321g
- 224 Lee C, Keenan CR, Sedlak DL. Polyoxometalate-Enhanced Oxidation of Organic Compounds by Nanoparticulate Zero-Valent Iron and Ferrous Ion in the Presence of Oxygen. *Environ Sci Technol*. 2008;42(13):4921–4926. doi: 10.1021/es800317j
- 225 Fei B-L, Zhong J-K, Deng N-P, Wang J-H, Liu Q-B, Li Y-G, et al. A novel 3D heteropoly blue type photo-Fenton-like catalyst and its ability to remove dye pollution. *Chemosphere*. 2018;197:241–50. doi:10.1016/j.chemosphere.2018.01.053
- 226 Grabsi M, Zabab N, Khellaf N, Ismail F. Synthesis of an environmental nano-polyoxometalate ( $\alpha_2P_2W_{17}CoO_{61}$ )<sup>8-</sup> as catalyst for dyes degradation: A comparative study oxidation of indigoid and azo dyes. *Environ Nanotechnol Monit Manag*. 2019;12:100269. doi: 10.1016/j.enmm.2019.100269
- 227 Li L, Sun J-W, Sha J-Q, Li G-M, Yan P-F, Wang C, Yu L. Structure Refinement and Photocatalytic Properties of Porous POMCPs by Selecting the Isomeric PYTTZ. *Dalton Trans*. 2015;44(4):1948–1954. doi: 10.1039/C4DT02960G
- 228 Shokri A, Fard MS. A critical review in Fenton-like approach for the removal of pollutants in the aqueous environment. *Environmental Challenges*. 2022;7:100534. doi: 10.1016/j.envc.2022.100534
- 229 An X, Tang Q, Lan H, Liu H, Qu J. Polyoxometalates/TiO<sub>2</sub> Fenton-like photocatalysts with rearranged oxygen vacancies for enhanced synergetic degradation. *Appl Catal B Environ*. 2019;244:407–413. doi: 10.1016/j.apcatb.2018.11.063
- 230 Orooji Y, Tanhaei B, Ayati A, Tabrizi SH, Alizadeh M, Bamoharram FF, et al. Heterogeneous UV-switchable Au nanoparticles decorated tungstophosphoric acid/TiO<sub>2</sub> for efficient photocatalytic degradation proces. *Chemosphere*. 2021;281:130795. doi:10.1016/j.chemosphere.2021.130795
- 231 Zhang L, Chen H, Zhao X, Zhai Q, Yin D, Sun Y, et al. The Marriage of Ferrocene and Silicotungstate: An Ingenious Heterogeneous Fenton-like Synergistic Photocatalyst. *Appl Catal B Environ*. 2016;193:47–57. doi: 10.1016/j.apcatb.2016.04.019
- 232 Wang Q, Liu E, Zhang C, Huang S, Cong Y, Zhang Y. Synthesis of Cs<sub>3</sub>PMo<sub>12</sub>O<sub>40</sub>/Bi<sub>2</sub>O<sub>3</sub> Composite with Highly Enhanced Photocatalytic Activity under Visible-Light Irradiation. *J Colloid Interface Sci*. 2018;516:304–311. doi: 10.1016/j.jcis.2018.01.065
- 233 Samal K, Mahapatra S, Ali MH. Pharmaceutical wastewater as Emerging Contaminants (EC): Treatment technologies, impact on environment and human health. *Energy Nexus*. 2022;6:100076. doi: 10.1016/j.nexus.2022.100076
- 234 Mishra RK, Mentha SS, Mirsa Y, Dwivedi N. Emerging pollutants of severe environmental concern in water and wastewater: A comprehensive review on current developments and future research. *Water-Energy Nexus*. 2023;6:74–95. doi: 10.1016/j.wen.2023.08.002
- 235 Wang S, Wang X, Shi X-Y, Meng C-X, Sun C-L, Wu Z-S. A three-dimensional polyoxometalate/graphene aerogel as a highly efficient and recyclable absorbent for oil/water separation. *New Carbon Mater*. 2021;36(1):189–197. doi: 10.1016/S1872-5805(21)60013-6
- 236 Wang S, Wang X, Shi X-Y, Meng C-X, Sun C-L, Wu Z-S, et al. Emerging contaminants: A One Health perspective. *Innovation*. 2024;4:100612. doi: 10.1016/j.xinn.2024.100612
- 237 Rubio-Armendáriz C, Alejandro-Vega S, Paz-Montelongo S, Gutiérrez-Fernández AJ, Carrascosa-Iruzubieta CJ, Hardisson-de la Torre A. Microplastics as Emerging Food Contaminants: A Challenge for Food Safety. *Int J Environ Res Public Health*. 2022;19(3):1174. doi: 10.3390/ijerph19031174
- 238 Sousa M, Machado I, Simões LC, Simões M. Biocides as drivers of antibiotic resistance: A critical review of environmental implications and public health risks. *Environ Sci Ecotechnol*. 2025;25:100557. doi: 10.1016/j.es.2025.100557
- 239 Caloni S, Durazzano T, Franci G, Marsili L. Sunscreens' UV Filters Risk for Coastal Marine Environment Biodiversity: A Review. *Diversity*. 2021;13:374. doi: 10.3390/d13080374
- 240 European Commission, Joint Research Centre, Gomez Cortes L, Marinov D, Sanseverino I, Navarro Cuenca A, et al. Selection of substances for the 4th Watch List under the Water Framework Directive. EUR 31148 EN. Luxembourg: Publications Office of the European Union; 2022. ISBN 978-92-76-55020-4. doi:10.2760/01939
- 241 European Chemicals Bureau, Institute for Health and Consumer Protection (Joint Research Centre). Technical Guidance Document on Risk Assessment in Support of Commission Directive 93/67/EEC on Risk Assessment for New Notified Substances, Commission Regulation (EC) No 1488/94 on Risk Assessment for Existing Substances, Directive 98/8/EC of the European Parliament and of the Council Concerning the Placing of Biocidal Products on the Market. Part III. Luxembourg: European Commission – Joint Research Centre; 2008. <https://op.europa.eu/en/publication-detail/-/publication/212940b8-3e55-43f8-8448-ba258d0374bb>
- 242 Boix C, Ibáñez M, Zamora T, Sancho JV, Niessen WMA, Hernández F. Identification of New Omeprazole Metabolites in Wastewaters and Surface Waters. *Sci Total Environ*. 2014;468:706–714. doi: 10.1016/j.scitotenv.2013.08.095
- 243 Wielens Becker R, Ibáñez M, Cuervo Lumbaque E, Wilde ML, Flores da Rosa T, Hernández F, et al. Investigation of pharmaceuticals and their metabolites in Brazilian hospital wastewater by LC-QTOF MS screening combined with a preliminary exposure and in silico risk assessment. *Sci Total Environ*. 2020;699:134218. doi:10.1016/j.scitotenv.2019.134218
- 244 Qiu X, Wang R. Polyoxometalate-Based Photocatalytic New Materials for the Treatment of Water Pollutants: Mechanism, Advances, and Challenges. *Catalysts*. 2025;15:613. doi: 10.3390/catal15070613
- 245 Murmu G, Panigrahi TH, Saha S. Recent advances in the development of polyoxometalates and their composites for the degradation of toxic chemical dyes. *Prog Solid State Chem*. 2024;76:100489. doi: 10.1016/j.progsolidstchem.2024.100489
- 246 Oliveira M, Antunes W, Mota S, Madureira-Carvalho A, Dinis-Oliveira RJ, Dias da Silva D. An Overview of the Recent Advances in Antimicrobial Resistance. *Microorganisms*. 2024;12:1920. doi: 10.3390/microorganisms12091920
- 247 Derakhshanrad S, Mirzaei M, Streb C, Amiri A, Ritchie C. Polyoxometalate-Based Frameworks as Adsorbents for Drug of Abuse Extraction from Hair Samples. *Inorg Chem*. 2021;60(3):1472–1479. doi: 10.1021/acs.inorgchem.0c02769
- 248 Yola ML, Atar N, Eren T, Karimi-Maleh H, Wang S. Sensitive and selective determination of aqueous triclosan based on gold nanoparticles on polyoxometalate/reduced graphene oxide nanohybrid. *RSC Adv*. 2015;5:65953–65962. doi: 10.1039/C5RA07443F
- 249 Cai J, Zhu G-T, He X-M, Zhang Z, Wang R-Q, Feng Y-Q. Polyoxometalate incorporated polymer monolith microextraction for highly selective extraction of antidepressants in undiluted urine. *Talanta*. 2017;170:252–259. doi: 10.1016/j.talanta.2017.04.020
- 250 He R, Xue K, Wang J, Yan Y, Peng Y, Yang T, et al. Nitrogen-Deficient g-C<sub>3</sub>N<sub>x</sub>/POMs Porous Nanosheets with P-N Heterojunctions Capable of the Efficient Photocatalytic Degradation of Ciprofloxacin. *Chemosphere*. 2020;259:127465. doi: 10.1016/j.chemosphere.2020.127465

- 251 Shi H, Zhao T, Wang J, Wang Y, Chen Z, Liu B, et al. Fabrication of g-C<sub>3</sub>N<sub>4</sub>/PW<sub>12</sub>/TiO<sub>2</sub> Composite with Significantly Enhanced Photocatalytic Performance under Visible Light. *J Alloys Compd.* 2021;860:157924. doi: 10.1016/j.jallcom.2020.157924
- 252 Cheng P, Wang Y, Sarakha M, Mailhot G. Enhancement of the Photocatalytic Activity of Decatungstate, W<sub>10</sub>O<sub>32</sub><sup>4-</sup>, for the Oxidation of Sulfasalazine/Sulfapyridine in the Presence of Hydrogen Peroxide. *J Photochem Photobiol.* 2021;404:112890. doi: 10.1016/j.jphotochem.2020.112890
- 253 Volin MV, Campbell PL, Connors MA, Woodruff DC, Koch AE. The Effect of Sulfasalazine on Rheumatoid Arthritic Synovial Tissue Chemokine Production. *Exp Mol Pathol.* 2002;73(2):84–92. doi: 10.1006/exmp.2002.2460
- 254 Wang JL, Xu LE. Advanced Oxidation Processes for Wastewater Treatment: Formation of Hydroxyl Radical and Application. *Crit Rev Environ Sci Technol.* 2012;42(3):251–325. doi: 10.1080/10643389.2010.507698
- 255 Khan S, Sohail M, Han C, Khan JA, Khan HM, Dionysiou DD. Degradation of Highly Chlorinated Pesticide, Lindane, in Water Using UV/Persulfate: Kinetics and Mechanism, Toxicity Evaluation, and Synergism by H<sub>2</sub>O<sub>2</sub>. *J Hazard Mater.* 2021;402:123558. doi: 10.1016/j.jhazmat.2020.123558
- 256 Wang J, Chen Y, Cheng N, Feng L, Gu B-H, Liu Y. Multivalent Supramolecular Self-Assembly between β-Cyclodextrin Derivatives and Polyoxometalate for Photodegradation of Dyes and Antibiotics. *ACS Appl Bio Mater.* 2019;2(12):5898–5904. doi: 10.1021/acssabm.9b00845
- 257 Li G, Zhang K, Li C, Gao R, Cheng Y, Hou L, et al. Solvent-free method to encapsulate polyoxometalate into metal-organic frameworks as efficient and recyclable photocatalyst for harmful sulfamethazine degrading in water. *Appl Catal B Environ.* 2019;245:753–9. doi:10.1016/j.apcatb.2019.01.012
- 258 da Silva ES, Sarakha M, Burrows HD, Wong-Wah-Chung P. Decatungstate Anion as an Efficient Photocatalytic Species for the Transformation of the Pesticide 2-(1-Naphthyl) Acetamide in Aqueous Solution. *J Photochem Photobiol A Chem.* 2017;334:61–73. doi: 10.1016/j.jphotochem.2016.10.036
- 259 Allaoui A, Malouki MA, Wong-Wah-Chung P. Homogeneous Photodegradation Study of 2-Mercaptobenzothiazole Photocatalysed by Sodium Decatungstate Salts: Kinetics and Mechanistic Pathways. *J Photochem Photobiol A Chem.* 2010;212(2–3):153–160. doi: 10.1016/j.jphotochem.2010.04.010
- 260 Antonaraki S, Triantis TM, Papaconstantinou E, Hiskia A. Photocatalytic Degradation of Lindane by Polyoxometalates: Intermediates and Mechanistic Aspects. *Catal Today.* 2010;151(1–2):119–124. doi: 10.1016/j.cattod.2010.02.017
- 261 Martinetto Y, Pégot B, Roch-Marchal C, Cottyn-Boitte B, Floquet S. Designing Functional Polyoxometalate-Based Ionic Liquid Crystals and Ionic Liquids. *Eur J Inorg Chem.* 2020;(3):228–247. doi: 10.1002/ejic.201900990
- 262 Majdafshar M, Piryaei M, Abolghasemi MM, Rafiee E. Polyoxometalate-Based Ionic Liquid Coating for Solid Phase Microextraction of Triazole Pesticides in Water Samples. *Sep Sci Technol.* 2019;54(10):1553–1559. doi: 10.1080/01496395.2019.1572625
- 263 Misra A, Zambrzycki C, Kloker G, Kotyrba A, Anjass MH, Franco Castillo I, et al. Water purification and microplastics removal using magnetic polyoxometalate-supported ionic liquid phases (MagPOM-SILPs). *Angew Chem Int Ed Engl.* 2020;59(4):1601–5. doi:10.1002/anie.201912111
- 264 The Royal Society. Microplastics in Freshwater and Soil. London: The Royal Society; 2019. ISBN: 978-1-78252-434-2. <https://royalsociety.org/-/media/policy/projects/microplastics/microplastics-evidence-synthesis-report.pdf>. Accessed September 1, 2025.
- 265 Ong BC, Lim HK, Tay CY, Lim T-T, Dong Z. Polyoxometalates for bifunctional applications: Catalytic dye degradation and anticancer activity. *Chemosphere.* 2022;286:131869. doi: 10.1016/j.chemosphere.2021.131869
- 266 Bijelic A, Aureliano M, Rompel A. The antibacterial activity of polyoxometalates: structures, antibiotic effects and future perspectives. *Chem Commun.* 2018;54:1153–1169. doi: 10.1039/C7CC07549A
- 267 Aureliano M, Gumerova NI, Sciortino G, Garribba E, Rompel A, Crans DC. Polyoxovanadates with emerging biomedical activities. *Coord Chem Rev.* 2021;447:214143. doi: 10.1016/j.ccr.2021.214143
- 268 Moghadasi M, Abbasi M, Mousavi M, Mirzaei M. Polyoxometalate-based materials in therapeutic and biomedical applications: current status and perspective. *Dalton Trans.* 2025;54:6333–6345. doi: 10.1039/D4DT03428G
- 269 Zhang H, Li M, Liu Z, Zhang X, Du C. Two Keggin-type polyoxometalates used as adsorbents with high efficiency and selectivity toward antibiotics and heavy metals. *J Mol Struct.* 2022;1267:133604. doi: 10.1016/j.molstruc.2022.133604
- 270 Pazhooh P, Khoshnavazi R, Bahrami L, Naseri E. Synthesis and Photocatalytic Activity Assessing of the TiO<sub>2</sub> Nanocomposites Modified by Some Lanthanide Ions and Tin-Derivative Sandwich-Type Polyoxometalates. *J Iran Chem Soc.* 2018;15(8):1775–1783. doi: 10.1007/s13738-018-1375-2
- 271 Wang K, He Y, Zhao Y, Ma P, Wang JA. Propionate-Functionalized Polyoxovanadate K<sub>2</sub>[V<sub>10</sub>O<sub>16</sub>(OH)<sub>6</sub>(CH<sub>3</sub>CH<sub>2</sub>CO<sub>2</sub>)<sub>6</sub>]-20H<sub>2</sub>O: As Catalyst for Degradation of Methylene Blue. *J Mol Struct.* 2019;1195:184–188. doi: 10.1016/j.molstruc.2019.05.130
- 272 Missina JM, Leme LBP, Postal K, Santana FS, Hughes DL, de Sá EL, et al. Accessing Decavanadate Chemistry with Tris(Hydroxymethyl)Aminomethane, and Evaluation of Methylene Blue Bleaching. *Polyhedron.* 2020;180:114414. doi: 10.1016/j.poly.2020.114414
- 273 Yang F, Zhu L, Xu Z, Han Y, Lin X, Shi J, et al. Multi-active photocatalysts of biochar-doped g-C<sub>3</sub>N<sub>4</sub> incorporated with polyoxometalates for the high-efficient degradation of sulfamethoxazole. *Environ Pollut.* 2024;361:124715. doi:10.1016/j.envpol.2024.124715
- 274 Song Y, Bo T, Ma J-C, Ma J-F. Highly efficient photoelectrocatalytic degradation for ciprofloxacin with a new polyoxometalate-based metal-organic hybrid/BiVO<sub>4</sub> photoanode. *Green Energy Environ.* 2025;10(7):1531–1542. doi: 10.1016/j.gee.2025.01.007
- 275 Mohammadian N, Firozjaee TT, Abdi J, Moghadasi M, Mirzaei M. PW<sub>12</sub>/Fe<sub>3</sub>O<sub>4</sub>/biochar nanocomposite as an efficient adsorbent for metronidazole removal from aqueous solution: Synthesis and optimization. *Surf Interfaces.* 2024;52:104946. doi: 10.1016/j.surfin.2024.104946
- 276 Nourouli H, Farhadi S, Malakooti R, Maleki M, Mahmoudi F. Construction of lacunary α-K<sub>8</sub>SiW<sub>11</sub>O<sub>39</sub> polyoxometalate/MIL-101(Cr) MOF/CoFe<sub>2</sub>O<sub>4</sub> magnetic nanocomposites for adsorptive removal of toxic azo dyes and antibiotics from wastewater. *CrystEngComm.* 2025;27:1185–1205. doi: 10.1039/D5CE00013K
- 277 Li J, Yu Z, Zhang J, Liu C, Zhang Q, Shi H, et al. Rapid, massive, and green synthesis of polyoxometalate-based metal-organic frameworks to fabricate POMOF/PAN nanofiber membranes for selective filtration of cationic dyes. *Molecules.* 2024;29:1493. doi:10.3390/molecules29071493
- 278 Kholdeeva OA, Timofeeva MN, Maksimov GM, Maksimovskaya RI, Neiwert WA, Hill CL. Aerobic Oxidation of Formaldehyde Mediated by a Ce-Containing Polyoxometalate under Mild Conditions. *Inorg Chem.* 2005;44(3):666–672. doi: 10.1021/ic049109o
- 279 Te M, Fairbridge C, Ring Z. Oxidation Reactivities of Dibenzothiophenes in Polyoxometalate/H<sub>2</sub>O<sub>2</sub> and Formic Acid/H<sub>2</sub>O<sub>2</sub> Systems. *Appl Catal A Gen.* 2001;219(1–2):267–280. doi: 10.1016/S0926-860X(01)00699-8

- 280 Liu Y, Zhang J, Sheng C, Zhang Y, Zhao L. Simultaneous Removal of NO and SO<sub>2</sub> from Coal-Fired Flue Gas by UV/H<sub>2</sub>O<sub>2</sub> Advanced Oxidation Process. *Chem Eng J*. 2010;162(3):1006–1011. doi: 10.1016/j.cej.2010.07.009
- 281 Gamelas JAF, Evtugina MG, Portugal I, Evtuguin DV. New Polyoxometalate-Functionalized Cellulosic Fibre/Silica Hybrids for Environmental Applications. *RSC Adv*. 2012;2(3):831–839. doi: 10.1039/C1RA00371B
- 282 Kholdeeva OA, Vanina MP, Timofeeva MN, Maksimovskaya RI, Trubitsina TA, Melgunov MS, et al. Co-containing polyoxometalate-based heterogeneous catalysts for the selective aerobic oxidation of aldehydes under ambient conditions. *J Catal*. 2004;226(2):363–71. doi:10.1016/j.jcat.2004.05.032
- 283 Eseva E, Akopyan A, Schepina A, Anisimov A, Maximov A. Deep Aerobic Oxidative Desulfurization of Model Fuel by Anderson-Type Polyoxometalate Catalysts. *Catal Commun*. 2021;149:106256. doi: 10.1016/j.catcom.2020.106256
- 284 Chi M, Zhu Z, Sun L, Su T, Liao W, Deng C, et al. Construction of biomimetic catalysis system coupling polyoxometalates with deep eutectic solvents for selective aerobic oxidation desulfurization. *Appl Catal B Environ*. 2019;259:118089. doi:10.1016/j.apcatb.2019.118089
- 285 Khan FI, Ghoshal AK. Removal of Volatile Organic Compounds from Polluted Air. *J Loss Prev Process Ind*. 2000;13(6):527–545. doi: 10.1016/S0950-4230(00)00007-3
- 286 Meng J, Wang X, Yang X, Hu A, Guo Y, Yang Y. Enhanced Gas-Phase Photocatalytic Removal of Aromatics over Direct Z-Scheme-Dictated H<sub>3</sub>PW<sub>12</sub>O<sub>40</sub>/g-C<sub>3</sub>N<sub>4</sub> Film-Coated Optical Fibers. *Appl Catal B Environ*. 2019;251:168–180. doi: 10.1016/j.apcatb.2019.03.063
- 287 Ullah I. Industrial-scale oxidative desulfurization: comprehensive process design and economic study for maritime oil production. *Appl Eng*. 2025;9(2):64–87. doi:10.11648/j.ae.20250902.12
- 288 Kanu A, Kuye A, Idikwu J. Comparative study on technologies for crude oil desulfurization: Hydrodesulfurization vs oxidative desulfurization. *Int J Innov Sci Res Technol*. 2025;4(6):1–15. doi:10.5281/zenodo.8108205
- 289 He J, Guan L, Zhou Y, Shao P, Yao Y, Lu S, et al. One-pot preparation of mesoporous K<sub>x</sub>PMO<sub>12</sub>O<sub>40</sub> (x = 1, 2, 3, 4) materials for oxidative desulfurization: electrochemically-active surface area (ECSA) determines their activity. *React Chem Eng*. 2020;5(9):1776–82. doi:10.1039/D0RE00213E
- 290 Ye G, Hu L, Gu Y, Lancelot C, Rives A, Lamonièr C, et al. Synthesis of polyoxometalate encapsulated in UiO-66(Zr) with hierarchical porosity and double active sites for oxidation desulfurization of fuel oil at room temperature. *J Mater Chem A*. 2020;8(37):19396–404. doi:10.1039/D0TA04337K
- 291 Gao Y, Gao R, Zhang G, Zheng Y, Zhao J. Oxidative Desulfurization of Model Fuel in the Presence of Molecular Oxygen over Polyoxometalate Based Catalysts Supported on Carbon Nanotubes. *Fuel*. 2018;224:261–270. doi: 10.1016/j.fuel.2018.03.034
- 292 Austigard ÅD, Svendsen K, Haldal KK. Hydrogen Sulphide Exposure in Waste Water Treatment. *J Occup Med Toxicol*. 2018;13:10–20. doi: 10.1186/s12995-018-0191-z
- 293 Badilla GL, Valdez B, Schorr M. Air Quality - New Perspective. London: IntechOpen; 2012. ISBN: 978-953-51-0674-6. doi: 10.5772/2561
- 294 Habeeb OA, Kanthasamy R, Ali GAM, Sethupathi S, Yunus RBM. Hydrogen Sulfide Emission Sources, Regulations, and Removal Techniques: A Review. *Rev Chem Eng*. 2018;34(6):837–854. doi: 10.1515/revce-2017-0004
- 295 Yang C, Wang Y, Fan H, de Falco G, Yang S, Shangguan J, et al. Bifunctional ZnO-MgO/activated carbon adsorbents boost H<sub>2</sub>S room temperature adsorption and catalytic oxidation. *Appl Catal B Environ*. 2020;266:118674. doi:10.1016/j.apcatb.2020.118674
- 296 Adib F, Bagreev A, Bandosz TJ. Analysis of the relationship between H<sub>2</sub>S removal capacity and surface properties of unimpregnated activated carbons. *Environ Sci Technol*. 2000;34(4):686–692. doi:10.1021/es990341g
- 297 Huang K, Feng X, Zhang X-M, Wu Y-T, Hu X-B. The ionic liquid-mediated Claus reaction: a highly efficient capture and conversion of hydrogen sulfide. *Green Chem*. 2016;18(7):1859–1863. doi:10.1039/C5GC03016A
- 298 Holz S, Köster P, Thielert H, Guetta Z, Repke J-U. Investigation of the degradation of chelate complexes in liquid redox desulfurization processes. *Chem Eng Technol*. 2020;43(3):476–483. doi:10.1002/ceat.201900420
- 299 Ma Y, Liu X, Wang R. Efficient removal of H<sub>2</sub>S at high temperature using the ionic liquid solutions of [C<sub>4</sub>mim]<sub>3</sub>PMO<sub>12</sub>O<sub>40</sub>—an organic polyoxometalate. *J Hazard Mater*. 2017;331:109–116. doi:10.1016/j.jhazmat.2017.02.036
- 300 Song J, Luo Z, Britt DK, Furukawa H, Yaghi OM, Hardcastle KI, et al. A multiunit catalyst with synergistic stability and reactivity: a polyoxometalate-metal organic framework for aerobic decontamination. *J Am Chem Soc*. 2011;133(42):16839–46. doi:10.1021/ja203695h
- 301 Muzio LJ, Quartucy GC. Implementing NO<sub>x</sub> control: research to application. *Prog Energy Combust Sci*. 1997;23(3):233–266. doi:10.1016/S0360-1285(97)00002-6
- 302 Skalska K, Miller JS, Ledakowicz S. Trends in NO<sub>x</sub> abatement: a review. *Sci Total Environ*. 2010;408(19):3976–3989. doi:10.1016/j.scitotenv.2010.06.001
- 303 Woodrow P. Nitric oxide: some nursing implications. *Intensive Crit Care Nurs*. 1997;13(2):87–92. doi:10.1016/S0964-3397(97)80186-3
- 304 Scherrer U, Vollenweider L, Delabays A, Savcic M, Eichenberger U, Kleger GR, et al. Inhaled nitric oxide for high-altitude pulmonary edema. *N Engl J Med*. 1996;334(10):624–629. doi:10.1056/NEJM199603073341003
- 305 Chaloulakou A, Mavroidis I, Gavriil I. Compliance with the annual NO<sub>2</sub> air quality standard in Athens. Required NO<sub>x</sub> levels and expected health implications. *Atmos Environ*. 2008;42(3):454–465. doi:10.1016/j.atmosenv.2007.09.067
- 306 Gómez-García MA, Pitchon V, Kiennemann A. Pollution by nitrogen oxides: an approach to NO<sub>x</sub> abatement by using sorbing catalytic materials. *Environ Int*. 2005;31(3):445–467. doi:10.1016/j.envint.2004.09.006
- 307 van Loon GW, Duffy SJ. Environmental chemistry: a global perspective. 2nd ed. Oxford: Oxford University Press; 2005. p.421–424. ISBN:0199274991
- 308 Qu Y, An J, He Y, Zheng J. An overview of emissions of SO<sub>2</sub> and NO<sub>x</sub> and the long-range transport of oxidized sulfur and nitrogen pollutants in East Asia. *J Environ Sci*. 2016;44:13–25. doi:10.1016/j.jes.2015.08.028
- 309 Lin F, Wang Z, Zhang Z, He Y, Zhu Y, Shao J, et al. Flue gas treatment with ozone oxidation: an overview on NO<sub>x</sub>, organic pollutants, and mercury. *Chem Eng J*. 2020;382:123030. doi:10.1016/j.cej.2019.123030
- 310 Fan Z, Shi J-W, Gao C, Gao G, Wang B, Wang Y, He C, Niu C. Gd-modified MnO<sub>x</sub> for the selective catalytic reduction of NO by NH<sub>3</sub>: the promoting effect of Gd on the catalytic performance and sulfur resistance. *Chem Eng J*. 2018;348:820–830. doi:10.1016/j.cej.2018.05.038
- 311 Hao R, Zhang Y, Wang Z, Li Y, Yuan B, Mao X, Zhao Y. An advanced wet method for simultaneous removal of SO<sub>2</sub> and NO from coal-fired flue gas by utilizing a complex absorbent. *Chem Eng J*. 2017;307:562–571. doi: 10.1016/j.cej.2016.08.103
- 312 Zhao Y, Han Y, Zhao Z. Removal of NO from flue gas by a heterogeneous Fenton-like process. *Chem Eng Technol*. 2018;41(11):2203–2211. doi: 10.1002/ceat.201700717
- 313 Liu Y, Zhang J, Pan J, Tang A. Investigation on the removal of NO from SO<sub>2</sub>-containing simulated flue gas by an

- ultraviolet/Fenton-like reaction. *Energy Fuels*. 2012;26(9):5430–5436. doi: 10.1021/ef3008568
- 314 Wang R, Zhang X, Ren Z. Germanium-based polyoxometalates for the adsorption-decomposition of NO<sub>x</sub>. *J Hazard Mater*. 2021;402:123494. doi: 10.1016/j.jhazmat.2020.123494
- 315 Montero-Montoya R, López-Vargas R, Arellano-Aguilar O. Volatile organic compounds in air: sources, distribution, exposure and associated illnesses in children. *Ann Glob Health*. 2018;84(2):225–238. doi: 10.29024/aogh.910
- 316 Weon S, Choi E, Kim H, Kim JY, Park H-J, Kim S, et al. Active 001 facet exposed TiO<sub>2</sub> nanotubes photocatalyst filter for volatile organic compounds removal: from material development to commercial indoor air cleaner application. *Environ Sci Technol*. 2018;52(16):9330–40. doi:10.1021/acs.est.8b02282
- 317 Mølhave L. Volatile organic compounds, indoor air quality and health. *Indoor Air*. 1991;1:357–376. doi: 10.1111/j.1600-0668.1991.00001.x
- 318 Harper M. Sorbent trapping of volatile organic compounds from air. *J Chromatogr A*. 2000;885(1–2):129–151. doi: 10.1016/S0021-9673(00)00363-0
- 319 Raillard C, Héquet V, Le Cloirec P, Legrand J. Comparison of different TiO<sub>2</sub> photocatalysts for the gas phase oxidation of volatile organic compounds. *Water Sci Technol*. 2004;50(4):241–250. doi: 10.2166/wst.2004.0274
- 320 Raillard C, Héquet V, Le Cloirec P, Legrand J. Photocatalytic oxidation of volatile organic compounds present in airborne environment adjacent to sewage treatment plants. *Water Sci Technol*. 2004;49(1):111–114. doi: 10.2166/wst.2004.0032
- 321 Dong P, Xi X, Hou G. Typical non-TiO<sub>2</sub>-based visible-light photocatalysts. In: *Semiconductor Photocatalysis*. London: IntechOpen; 2016. doi: 10.5772/62889
- 322 Ma F-J, Liu S-X, Liang D-D, Ren G-J, Wei F, Chen Y-G, Su Z-M. Adsorption of volatile organic compounds in porous metal-organic frameworks functionalized by polyoxometalates. *J Solid State Chem*. 2011;184(11):3034–3039. doi: 10.1016/j.jssc.2011.09.002
- 323 Salthammer T, Mentese S, Marutzky R. Formaldehyde in the indoor environment. *Chem Rev*. 2010;110(4):2536–2572. doi: 10.1021/cr800399g
- 324 Salthammer T. Formaldehyde in the ambient atmosphere: from an indoor pollutant to an outdoor pollutant? *Angew Chem Int Ed Engl*. 2013;52(12):3320–3327. doi: 10.1002/anie.201205984
- 325 Kehrer JP. The Haber–Weiss reaction and mechanisms of toxicity. *Toxicology*. 2000;149(1):43–50. doi: 10.1016/S0300-483X(00)00231-6
- 326 Gamelas JAF, Oliveira F, Evtugina MG, Portugal I, Evtuguin DV. Catalytic oxidation of formaldehyde by ruthenium multisubstituted tungstosilicic polyoxometalate supported on cellulose/silica hybrid. *Appl Catal A Gen*. 2016;509:8–16. doi: 10.1016/j.apcata.2015.10.003
- 327 Huang Y, Wang J, Ma S, Wang R, Wang Y. Enhanced adsorption-oxidation performance of PMo<sub>12</sub> immobilized onto porous MCM-41 derived from rice husk for H<sub>2</sub>S at room temperature. *Fuel*. 2023;333:126448. doi: 10.1016/j.fuel.2022.126448
- 328 Wang R, Zhang L, Wang X. Tuning the redox activity of polyoxometalate by central atom for high-efficient desulfurization. *J Hazard Mater*. 2022;440:129710. doi:10.1016/j.jhazmat.2022.129710
- 329 Li J, Wang R. Polyoxometalate/ionic liquid desulfurization system for hydrogen sulfide removal from high-temperature gas stream. *Molecules*. 2022;27:6723. doi:10.3390/molecules27196723
- 330 Li J, Wang R, Dou S. Electrolytic cell-assisted polyoxometalate based redox mediator for H<sub>2</sub>S conversion to elemental sulphur and hydrogen. *Chem Eng J*. 2021;404:127090. doi:10.1016/j.cej.2020.127090
- 331 Rafiee E, Mirnezami F. Keggin-structured polyoxometalate-based ionic liquid salts: thermoregulated catalysts for rapid oxidation of sulfur-based compounds using H<sub>2</sub>O<sub>2</sub> and extractive oxidation desulfurization of sulfur-containing model oil. *J Mol Liq*. 2014;199:156–161. doi:10.1016/j.molliq.2014.08.036
- 332 Wang R. Performance of new liquid redox desulfurization system of heteropoly compound in comparison with that of iron chelate. *Korean J Chem Eng*. 2003;20:659–663. doi:10.1007/BF02706904
- 333 Wang R. Investigation on a new liquid redox method for H<sub>2</sub>S removal and sulfur recovery with heteropoly compound. *Sep Purif Technol*. 2003;31(1):111–121. doi:10.1016/S1383-5866(02)00153-3
- 334 Wang B, Wang R. Highly-efficient H<sub>2</sub>S capture by deep eutectic solvents based on ionic liquid hybridized polyoxometalate: insights into conformational transitions and structure-activity relationships. *J Hazard Mater*. 2025;495:139037. doi:10.1016/j.jhazmat.2025.139037
- 335 Wang B, Wang R. Medium and high temperature H<sub>2</sub>S removal via phosphazene polyoxometalate ionic liquids: performance evaluation and mechanism exploration. *Sep Purif Technol*. 2025;357(Part B):130196. doi:10.1016/j.seppur.2024.130196
- 336 Huang Y, Zuo Q, Yin M, Wang J, Gao B, Song J, et al. Cyclodextrin-assisted high selectivity of imprinted adsorbents loaded on polyoxometalate@UiO-66 for H<sub>2</sub>S removal at ambient temperature. *Sep Purif Technol*. 2025;356(Part B):129932. doi:10.1016/j.seppur.2024.129932
- 337 Liu F, Deng Y, Niu L, Wang S, Wang B, Li M, et al. Study on desulfurization and regeneration performance of nanofluid system based on heteropoly compound/ionic liquid solutions. *Ind Eng Chem Res*. 2024;63(27):12155–12165. doi:10.1021/acs.iecr.4c01242
- 338 Zhao Y, Qin X, Zhao X, Wang X, Tan H, Sun H, et al. Polyoxometalates-doped Bi<sub>2</sub>O<sub>3-x</sub>/Bi photocatalyst for highly efficient visible-light photodegradation of tetrabromobisphenol A and removal of NO. *Chin J Catal*. 2022;43(3):771–781. doi:10.1016/S1872-2067(21)63843-3
- 339 Zhang X, Wang R, Zhu H, Chen Y. Performance of NO<sub>x</sub> capture with Dawson polyoxometalate H<sub>6</sub>P<sub>2</sub>W<sub>18</sub>O<sub>62</sub>·28H<sub>2</sub>O. *Chem Eng J*. 2020;400:125880. doi:10.1016/j.cej.2020.125880
- 340 Weng X, Dai X, Zeng Q, Liu Y, Wu Z. DRIFT studies on promotion mechanism of H<sub>3</sub>PW<sub>12</sub>O<sub>40</sub> in selective catalytic reduction of NO with NH<sub>3</sub>. *J Colloid Interface Sci*. 2016;461:9–14. doi:10.1016/j.jcis.2015.09.004
- 341 Ma F-J, Liu S-X, Ren G-J, Liang D-D, Sha S. A hybrid compound based on porous metal-organic frameworks and polyoxometalates: NO adsorption and decomposition. *Inorg Chem Commun*. 2012;22:174–177. doi:10.1016/j.inoche.2012.05.055
- 342 Gómez-García MA, Pitchon V, Kiennemann A. Multifunctional catalysts for de-NO<sub>x</sub> processes: the case of H<sub>3</sub>PW<sub>12</sub>O<sub>40</sub>·6H<sub>2</sub>O-metal supported on mixed oxides. *Appl Catal B Environ*. 2007;70(1–4):151–159. doi:10.1016/j.apcatb.2005.12.029
- 343 Hodjati S, Petit C, Pitchon V, Kiennemann A. Removal of NO<sub>x</sub> from a lean exhaust gas by absorption on heteropolyacids: reversible sorption of nitrogen oxides in H<sub>3</sub>PW<sub>12</sub>O<sub>40</sub>·6H<sub>2</sub>O. *J Catal*. 2001;197(2):324–334. doi:10.1006/jcat.2000.3108
- 344 Bélanger R, Moffat JB. Sorption and reduction of NO<sub>2</sub> on microporous ammonium 12-tungstophosphate. *Langmuir*. 1996;12(9):2230–2238. doi:10.1021/la950952w
- 345 Lu S, Guo X, Xu X, Han Z, Chen M, Lin B, et al. POM-promoted synergistic catalysis of NO and chlorobenzene over amorphous MnCeO<sub>x</sub> catalysts: activation of lattice oxygen, role of acid site, catalytic mechanism. *J Hazard Mater*. 2025;495:138873. doi:10.1016/j.jhazmat.2025.138873

- 346 Ma M, Zhang R, Shen Y, Zhou X, Zhai Y, Han Y, et al. Mesoporous Ce–Ti catalysts modified by phosphotungstic acid and chitosan for the synergistic catalysis of CVOCs and NO<sub>x</sub>. *Catalysts*. 2025;15:119. doi:10.3390/catal15020119
- 347 Guo W, Luo Z, Lv H, Hill CL. Aerobic oxidation of formaldehyde catalyzed by polyvanadotungstates. *ACS Catal*. 2014;4(4):1154–1161. doi:10.1021/cs5000763
- 348 Zhou Y, Yue B, Bao R-L, Liu S-X, He H-Y. Catalytic aerobic oxidation of acetaldehyde over Keggin-type molybdovanadophosphoric acid/SBA-15 under ambient condition. *Chin J Chem*. 2006;24(8):1001–1005. doi:10.1002/cjoc.200690187
- 349 Ammam M. Polyoxometalates: formation, structures, principal properties, main deposition methods and application in sensing. *J Mater Chem A*. 2013;1(21):6291–6312. doi:10.1039/C3TA01663C
- 350 Khodadadi Dizaji A, Mortaheb HR, Mokhtarani B. Preparation of supported catalyst by adsorption of polyoxometalate on graphene oxide/reduced graphene oxide. *Mater Chem Phys*. 2017;199:424–434. doi:10.1016/j.matchemphys.2017.07.016
- 351 Putzbach W, Ronkainen N. Immobilization techniques in the fabrication of nanomaterial-based electrochemical biosensors: a review. *Sensors*. 2013;13(4):4811–4840. doi:10.3390/s130404811
- 352 Johnson KW. Reproducible electrodeposition of biomolecules for the fabrication of miniature electroenzymatic biosensors. *Sens Actuators B Chem*. 1991;5(1–4):85–89. doi:10.1016/0925-4005(91)80225-9
- 353 Yang M, Kim DS, Yoon JH, Hong SB, Jeong SW, Yoo DE, et al. Nanopillar films with polyoxometalate-doped polyaniline for electrochemical detection of hydrogen peroxide. *Analyst*. 2016;141(4):1319–1324. doi:10.1039/C5AN02134K
- 354 Pourbeyram S, Moosavifar M, Hasanazadeh V. Electrochemical characterization of the encapsulated polyoxometalates (POMs) into the zeolite. *J Electroanal Chem*. 2014;714–715:19–24. doi:10.1016/j.jelechem.2013.12.014
- 355 Zasadzinski JA, Viswanathan R, Madsen L, Garnæs J, Schwartz DK. Langmuir–Blodgett films. *Science*. 1994;263(5154):1726–1733. doi:10.1126/science.8134836
- 356 Ito T, Yashiro H, Yamase T. Regular two-dimensional molecular array of photoluminescent Anderson-type polyoxometalate constructed by Langmuir–Blodgett technique. *Langmuir*. 2006;22(6):2806–2810. doi:10.1021/la052972w
- 357 Chen W, McCarthy TJ. Layer-by-layer deposition: a tool for polymer surface modification. *Macromolecules*. 1997;30(1):78–86. doi:10.1021/ma961096d
- 358 Ma H, Peng J, Han Z, Feng Y, Wang E. Preparation and characterization of luminescent nanocomposite film containing polyoxometalate. *Thin Solid Films*. 2004;446(2):161–166. doi:10.1016/j.tsf.2003.09.040
- 359 Ammam M, Easton EB. Novel organic–inorganic hybrid material based on tris(2,2'-bipyridyl)dichlororuthenium(II) hexahydrate and Dawson-type tungstophosphate K<sub>7</sub>[H<sub>4</sub>PW<sub>18</sub>O<sub>62</sub>]·18H<sub>2</sub>O as a bifunctional hydrogen peroxide electrocatalyst for biosensors. *Sens Actuators B Chem*. 2012;161(1):520–527. doi:10.1016/j.snb.2011.10.070
- 360 Ammam M, Fransær J. Ionic liquid–heteropolyacid: Synthesis, characterization, and supercapacitor study of films deposited by electrophoresis. *J Electrochem Soc*. 2011;158(1):A14–A21. doi:10.1149/1.3507254
- 361 Zhang L, Li C, Li F, Li S, Ma H, Gu F. A sensing platform based on Cu-MOF encapsulated Dawson-type polyoxometalate crystal material for electrochemical detection of xanthine. *Microchim Acta*. 2023;190:24. doi:10.1007/s00604-022-05601-1
- 362 Shetty SS, Moosa B, Zhang L, Alshankiti B, Baslyman W, Mani V, et al. Polyoxometalate–cyclodextrin supramolecular entities for real-time in situ monitoring of dopamine released from neuroblastoma cells. *Biosens Bioelectron*. 2023;229:115240. doi:10.1016/j.bios.2023.115240.
- 363 Tian R, Zhang B, Zhao M, Ma Q, Qi Y. Polyoxometalates as promising enzyme mimics for the sensitive detection of hydrogen peroxide by fluorometric method. *Talanta*. 2018;188:332–338. doi:10.1016/j.talanta.2018.05.085
- 364 Verissimo MIS, Evtuguin DV, Gomes MTSR. Polyoxometalate functionalized sensors: a review. *Front Chem*. 2022;10:840657. doi:10.3389/fchem.2022.840657
- 365 Ammam M, Easton EB. Selective determination of ascorbic acid with a novel hybrid material based 1-butyl-3-methylimidazolium tetrafluoroborate ionic liquid and the Dawson type ion [P<sub>2</sub>Mo<sub>18</sub>O<sub>62</sub>]<sup>6-</sup> immobilized on glassy carbon. *Electrochim Acta*. 2011;56(7):2847–2855. doi:10.1016/j.electacta.2010.12.072
- 366 Wang R, Jia D, Cao Y. Facile synthesis and enhanced electrocatalytic activities of organic–inorganic hybrid ionic liquid polyoxometalate nanomaterials by solid-state chemical reaction. *Electrochim Acta*. 2012;72:101–107. doi:10.1016/j.electacta.2012.04.011
- 367 Liu S, Tang Z, Wang Z, Peng Z, Wang E, Dong S. Oriented polyoxometalate–polycation multilayers on a carbon substrate. *J Mater Chem*. 2000;10(12):2727–2733. doi:10.1039/B004142O
- 368 Salimi A, Korani A, Hallaj R, Khoshnavazi R, Hadadzadeh H. Immobilization of [Cu(bpy)<sub>2</sub>]Br<sub>2</sub> complex onto a glassy carbon electrode modified with α-SiMo<sup>12</sup>O<sub>40</sub><sup>4-</sup> and single walled carbon nanotubes: application to nanometric detection of hydrogen peroxide and bromate. *Anal Chim Acta*. 2009;635(1):63–70. doi:10.1016/j.aca.2009.01.007
- 369 Wang B, Cheng L, Dong S. Construction of a heteropolyanion-modified electrode by a two-step sol–gel method and its electrocatalytic applications. *J Electroanal Chem*. 2001;516(1–2):17–22. doi:10.1016/S0022-0728(01)00677-5
- 370 Thangamuthu R, Pan Y-C, Chen S-M. Iodate sensing electrodes based on phosphotungstate-doped-glutaraldehyde-cross-linked poly-L-lysine coatings. *Electroanalysis*. 2010;22(16):1812–1816. doi:10.1002/elan.201000024
- 371 Ma H, Zhang Z, Pang H, Li S, Chen Y, Zhang W. Fabrication and electrochemical sensing property of a composite film based on a polyoxometalate and palladium nanoparticles. *Electrochim Acta*. 2012;69:379–383. doi:10.1016/j.electacta.2012.03.017
- 372 Zhu H, Tang W, Ma Y, Wang Y, Tan H, Li Y. Preyssler-type polyoxometalate-based crystalline materials for the electrochemical detection of H<sub>2</sub>O<sub>2</sub>. *CrystEngComm*. 2021;23(10):2071–2080. doi:10.1039/D1CE00059D
- 373 Hu YY, Han RX, Mei L, Liu JL, Sun JC, Yang K, Zhao JW. Design principles of MOF-related materials for highly stable metal anodes in secondary metal-based batteries. *Mater Today Energy*. 2021;19:100608. doi:10.1016/j.mtener.2020.100608
- 374 Wang C, Ying J, Mou H-C, Tian A-X, Wang X-I. Multi-functional photoelectric sensors based on a series of isopolymolybdate-based compounds for detecting different ions. *Inorg Chem Front*. 2020;7(20):3882–3894. doi:10.1039/D0QI00505C
- 375 Tian A, Yang M, Ni H, Sun N, Yang Y, Fu Y, Ying J. Use of symmetrical and pendant pyrazole derivatives for the construction of two polyoxometalate-based complexes as electrochemical sensors. *Transit Met Chem*. 2018;43:621–633. doi:10.1007/s11243-018-0250-4
- 376 Yang M, Rong S, Wang X, Ma H, Pang H, Tan L, et al. Preparation and application of Keggin polyoxometalate-based 3D coordination polymer materials as supercapacitors and amperometric sensors. *ChemNanoMat*. 2021;7(3):299–306. doi:10.1002/cnma.202000654
- 377 Xin X, Hu N, Ma Y, Wang Y, Hou L, Zhang H, et al. Polyoxometalate-based crystalline materials as a highly sensitive electrochemical sensor for detecting trace Cr(VI).

- Dalton Trans.* 2020;49:4570–4577. doi:10.1039/D0DT00446D
- 378 Krutovertsev SA, Ivanova OM, Sorokin SI. Sensing properties of polyaniline films doped with Dawson heteropoly compounds. *J Anal Chem.* 2001;56:1057–1060. doi:10.1023/A:1012569127685
- 379 Khan MI, Aydemir K, Siddiqui MRH, Alwarthan AA, Marshall CL. Oxidative dehydrogenation properties of novel nanostructured polyoxovanadate based materials. *Catal Lett.* 2011;141:538–543. doi:10.1007/s10562-011-0547-9
- 380 Tess ME, Cox JA. Humidity-independent solid-state amperometric sensor for carbon monoxide based on an electrolyte prepared by sol–gel chemistry. *Anal Chem.* 1998;70(1):187–190. doi:10.1021/ac9708396
- 381 Ammam M, Easton EB. Advanced NOx gas sensing based on novel hybrid organic–inorganic semiconducting nanomaterial formed between pyrrole and Dawson type polyoxoanion  $[P_2Mo_{18}O_{62}]^{6-}$ . *J Mater Chem.* 2011;21(22):7886–7891. doi:10.1039/C1JM11244A
- 382 Wang T, Sun Z, Wang Y, Liu R, Sun M, Xu L. Enhanced photoelectric gas sensing performance of SnO<sub>2</sub> flower-like nanorods modified with polyoxometalate for detection of volatile organic compound at room temperature. *Sens Actuators B Chem.* 2017;246:769–775. doi:10.1016/j.snb.2017.02.108
- 383 Zhang Q, Wang T, Sun Z, Xi L, Xu L. Performance improvement of photoelectrochemical NO<sub>2</sub> gas sensing at room temperature by BiVO<sub>4</sub>–polyoxometalate nanocomposite photoanode. *Sens Actuators B Chem.* 2018;272:289–295. doi:10.1016/j.snb.2018.05.169
- 384 Shi H, Li N, Sun Z, Wang T, Xu L. Interface modification of titanium dioxide nanoparticles by titanium-substituted polyoxometalate doping for improvement of photoconductivity and gas sensing applications. *J Phys Chem Solids.* 2018;120:57–63. doi:10.1016/j.jpss.2018.04.014
- 385 Tian J, Chen X, Wang T, Pei W, Li F, Li D, et al. Modification of indium oxide nanofibers by polyoxometalate electron acceptor doping for enhancement of gas sensing at room temperature. *Sens Actuators B Chem.* 2021;344:130227. doi:10.1016/j.snb.2021.130227
- 386 Wang Y, Fu X, Wang T, Li F, Li D, Yang Y, et al. Polyoxometalate electron acceptor incorporated improved properties of Cu<sub>2</sub>ZnSnS<sub>4</sub>-based room temperature NO<sub>2</sub> gas sensor. *Sens Actuators B Chem.* 2021;348:130683. doi:10.1016/j.snb.2021.130683
- 387 Sun X, Lan Q, Geng J, Yu M, Li Y, Li X, et al. Polyoxometalate as electron acceptor in dye/TiO<sub>2</sub> films to accelerate room-temperature NO<sub>2</sub> gas sensing. *Sens Actuators B Chem.* 2023;374:132795. doi:10.1016/j.snb.2022.132795
- 388 Kida T, Kawasaki K, Lemura K, Teshima K, Nagano M. Gas sensing properties of a stabilized zirconia-based sensor with a porous MoO<sub>3</sub> electrode prepared from a molybdenum polyoxometalate–alkylamine hybrid film. *Sens Actuators B Chem.* 2006;119(2):562–9. doi:10.1016/j.snb.2006.01.025
- 389 Wei H, Zhang J, Shi N, Liu Y, Zhang B, Zhang J, et al. A recyclable polyoxometalate-based supramolecular chemosensor for efficient detection of carbon dioxide. *Chem Sci.* 2015;6:7201–5. doi:10.1039/C5SC02020D
- 390 Guo Y, Gong Y, Qi L, Gao Y, Yu L. A polyoxometalate-based supramolecular chemosensor for rapid detection of hydrogen sulfide with dual signals. *J Colloid Interface Sci.* 2017;485:280–7. doi:10.1016/j.jcis.2016.09.047
- 391 Bezdek MJ, Luo S-XL, Liu RY, He Q, Swager TM. Trace hydrogen sulfide sensing inspired by polyoxometalate-mediated aerobic oxidation. *ACS Cent Sci.* 2021;7(9):1572–80. doi:10.1021/acscentsci.1c00746
- 392 Liu S, Volkmer D, Kurth DG. Smart polyoxometalate-based nitrogen monoxide sensors. *Anal Chem.* 2004;76(15):4579–82. doi:10.1021/ac0495283
- 393 Cai L-X, Chen L, Sun X-Q, Geng J, Liu C-C, Wang Y, et al. Ultra-sensitive triethylamine gas sensors based on polyoxometalate-assisted synthesis of ZnWO<sub>4</sub>/ZnO heterostructured nanofibers. *Sens Actuators B Chem.* 2022;370:132422. doi:10.1016/j.snb.2022.132422
- 394 Tian J, Jiang B, Shao H, Wang Y, Wang T, Li F, et al. A new strategy to one-step construct polyoxometalate/semiconductor one-dimensional tandem heterojunctions toward optimized conductometric sensing performances of ethanol gas. *Sens Actuators B Chem.* 2023;374:132797. doi:10.1016/j.snb.2022.132797
- 395 Chen L, Cai L-X, Geng J, Liu C-C, Wang Y, Guo Z. Polyoxometalate-assisted in situ growth of ZnMoO<sub>4</sub> on ZnO nanofibers for the selective detection of ppb-level acetone. *Sens Actuators B Chem.* 2022;369:132354. doi:10.1016/j.snb.2022.132354
- 396 Ren Y, Xie W, Li Y, Ma J, Li J, Liu Y, et al. Noble metal nanoparticles decorated metal oxide semiconducting nanowire arrays interwoven into 3D mesoporous superstructures for low-temperature gas sensing. *ACS Cent Sci.* 2021;7(11):1885–97. doi:10.1021/acscentsci.1c00912
- 397 Zhang X-Z, Zhu W-J, Yang Z-X, Feng Y, Fan L-L, Gao G-G, et al. Ultrasensitive photochromic and Raman dual response to ethylenediamine gas through polyoxometalate–viologen crystalline hybrid. *J Mater Chem C.* 2022;10(41):15451–7. doi:10.1039/D2TC03053E
- 398 Wang C, Ying J, Zhang X, Zhang B, Tian A, Zhang Y. POM-based compounds as capacitor materials and their photoelectric-sensing properties toward inorganic ions. *J Coord Chem.* 2021;74(14):2315–26. doi:10.1080/00958972.2021.1952998
- 399 Tian A-X, Yang M-L, Sun N, Fu Y-B, Ying J. A series of pH-dependent POM-based compounds as photocatalysts and electrochemical sensors. *Polyhedron.* 2018;155:337–50. doi:10.1016/j.poly.2018.08.065
- 400 Zhang X, Zhang Y, Ying J, Zhang B, Wang C, Tian A. A series of POM-based compounds constructed by piperazine and morpholine derivatives: characterization, selective photocatalytic and electrochemical/fluorescence sensing properties. *J Solid State Chem.* 2021;295:121888. doi:10.1016/j.jssc.2020.121888
- 401 Wang C, Zhou M, Ma Y, Tan H, Wang Y, Li Y. Hybridized polyoxometalate-based metal–organic framework with ketjenblack for the nonenzymatic detection of H<sub>2</sub>O<sub>2</sub>. *Asian J Chem.* 2018;13(16):2054–9. doi:10.1002/asia.201800758
- 402 Wang X, Li L, Wang X, Zhang Y. Various amide-derived ligands induced five octamolybdate-based metal–organic complexes: synthesis, structure, electrochemical sensing and photocatalytic properties. *CrystEngComm.* 2021;23(30):5176–83. doi:10.1039/D1CE00266J
- 403 Liang C, Wang X, Yu D, Guo W, Zhang F, Qu F. In-situ immobilization of a polyoxometalate metal–organic framework (NENU-3) on functionalized reduced graphene oxide for hydrazine sensing. *Chin J Chem.* 2021;39(10):2889–97. doi:10.1002/cjoc.202100314
- 404 Liu Q-Q, Wang X-L, Lin H-Y, Chang Z-H, Zhang Y-C, Tian Y, et al. Two new polyoxometalate-based metal–organic complexes for the detection of trace Cr(VI) and their capacitor performance. *Dalton Trans.* 2021;50(27):9450–6. doi:10.1039/D1DT01247A
- 405 Zhang Y, Zhang Y, Li L, Chen J, Li P, Huang W. One-step in situ growth of high-density POMOFs films on carbon cloth for the electrochemical detection of bromate. *J Electroanal Chem.* 2020;861:113939. doi:10.1016/j.jelechem.2020.113939
- 406 Largeot C, Portet C, Chmiola J, Taberna P-L, Gogotsi Y, Simon P. Relation between the ion size and pore size for an electric double-layer capacitor. *J Am Chem Soc.* 2008;130(9):2730–1. doi:10.1021/ja7106178
- 407 Cuentas-Gallegos AK, Lira-Cantú M, Casañ-Pastor N, Gómez-Romero P. Nanocomposite hybrid molecular materials for application in solid-state electrochemical supercapacitors. *Adv Funct Mater.* 2005;15(7):1125–33. doi:10.1002/adfm.200400326

- 408 Vaillant J, Lira-Cantu M, Cuentas-Gallegos K, Casañ-Pastor N, Gómez-Romero P. Chemical synthesis of hybrid materials based on PANi and PEDOT with polyoxometalates for electrochemical supercapacitors. *Prog Solid State Chem.* 2006;34(2):147–59. doi:10.1016/j.progsolidstchem.2005.11.015
- 409 Pope MT, Müller A. Polyoxometalate chemistry: an old field with new dimensions in several disciplines. *Angew Chem Int Ed Engl.* 1991;30(1):34–48. doi:10.1002/anie.199100341
- 410 Pope MT. Heteropoly and isopoly oxometalates. New York: Springer-Verlag; 1983. (Inorganic Chemistry Concepts).
- 411 Pope MT, Müller A, editors. Polyoxometalates: from platonic solids to anti-retroviral activity. Dordrecht: Springer; 1994. doi:10.1007/978-94-011-0920-8
- 412 Guo Y-G, Hu J-S, Wan L-J. Nanostructured materials for electrochemical energy conversion and storage devices. *Adv Mater.* 2008;20(15):2878–87. doi:10.1002/adma.200800627
- 413 Sonoyama N, Suganuma Y, Kume T, Quan Z. Lithium intercalation reaction into the Keggin type polyoxomolybdates. *J Power Sources.* 2011;196(16):6822–7. doi:10.1016/j.jpowsour.2010.09.107
- 414 Chen J-J, Symes MD, Fan S-C, Zheng M-S, Miras HN, Dong Q-F, et al. High-performance polyoxometalate-based cathode materials for rechargeable lithium-ion batteries. *Adv Mater.* 2015;27(31):4649–54. doi:10.1002/adma.201501088
- 415 Ni E, Uematsu S, Quan Z, Sonoyama N. Improved electrochemical property of nanoparticle polyoxovanadate  $K_7NiV_{13}O_{38}$  as cathode material for lithium battery. *J Nanopart Res.* 2013;15(6):1732. doi:10.1007/s11051-013-1732-0
- 416 Ma D, Liang L, Chen W, Liu H, Song Y-F. Covalently tethered polyoxometalate–pyrene hybrids for noncovalent sidewall functionalization of single-walled carbon nanotubes as high-performance anode material. *Adv Funct Mater.* 2013;23(48):6100–5. doi:10.1002/adfm.201301624
- 417 Wang S, Li H, Li S, Liu F, Wu D, Feng X, et al. Electrochemical-reduction-assisted assembly of a polyoxometalate/graphene nanocomposite and its enhanced lithium-storage performance. *Chem Eur J.* 2013;19(33):10895–902. doi:10.1002/chem.201300319
- 418 Xu C, Yang X, Hu C, Zhang J, Yang L, Yin S. One pot synthesis of polyoxometalates@polyaniline/MXene/CNTs quaternary composites with a 3D structure as efficient electrode materials. *Compos Commun.* 2024;34:101814. doi:10.1016/j.coco.2024.101814
- 419 Mahajan M, Sigla G, Ogale S. Polypyrrole-encapsulates polyoxomolybdate decorated MXene as a functional 2D/3D nanohybrid for a robust and high performance Li-ion battery. *ACS Appl Energy Mater.* 2021;4(5):4541–50. doi:10.1021/acsaem.1c00175
- 420 Liu Y, Zhou X, Qiu T, Yao R, Yu F, Song T, et al. Co-assembly of polyoxometalates and porphyrins as anode for high-performance lithium-ion batteries. *Adv Mater.* 2024;36(35):2407705. doi:10.1002/adma.202407705
- 421 Li Q, Xu M, Wang T, Wang H, Sun J, Sha J. Nanohybridization of  $CoS_2/MoS_2$  heterostructure with polyoxometalate on functionalized reduced graphene oxide for high-performance LIBs. *Chem Eur J.* 2022;28(20):e202200207. doi:10.1002/chem.202200207
- 422 Li M-T, Zhou X-H, Liang Q-M, Chen J, Sun J-W, Yu Y, et al. POMs-based metal-organic frameworks with interpenetrating structures and their carbon nanotube-coated materials for lithium-ion anode applications. *J Solid State Chem.* 2024;337:124787. doi:10.1016/j.jssc.2024.124787
- 423 Sun S, Cui L, Yu K, Wang M, Lv J, Ge S, et al. 3D porous metal–organic skeleton based on polyoxometalate nanoclusters as an anode in a lithium-ion battery. *ACS Appl Nano Mater.* 2024;7(1):1310–8. doi:10.1021/acsnm.3c05315
- 424 Liu J-H, Yu M-Y, Pei W-Y, Wang T, Ma J-F. Self-assembly of polyoxometalate-resorcinarene-based inorganic-organic complexes: metal ion effects on the electrochemical performance of lithium ion batteries. *Chem Eur J.* 2021;27(39):10123–33. doi:10.1002/chem.202100780
- 425 Ullah I, Aldhafeeri TR, Haider A, Wu X, Ullah Z, Chang S, et al. Layered arrangement of polyoxometalate on a metal–organic framework as a high-capacity anode material for sodium-ion batteries. *ACS Appl Energy Mater.* 2025;8(3):1743–51. doi:10.1021/acsaem.4c02904
- 426 Liu J, Chen Z, Chen S, Zhang B, Wang J, Wang H, et al. "Electron/ion sponge"-like V-based polyoxometalate: toward high-performance cathode for rechargeable sodium ion batteries. *ACS Nano.* 2017;11(7):6911–20. doi:10.1021/acsnano.7b02062
- 427 Hartung S, Bucher N, Chen H-Y, Al-Oweini R, Sreejith S, Borah P, et al. Vanadium-based polyoxometalate as new material for sodium-ion battery anodes. *J Power Sources.* 2015;288:270–7. doi:10.1016/j.jpowsour.2015.04.009
- 428 Cao D, Sha Q, Wang J, Li J, Ren J, Shen T, et al. Advanced anode materials for sodium-ion batteries: confining polyoxometalates in flexible metal–organic frameworks by the "breathing effect". *ACS Appl Mater Interfaces.* 2022;14(19):22186–96. doi:10.1021/acsaami.2c04077
- 429 Zhang LL, Zhao XS. Carbon-based materials as supercapacitor electrodes. *Chem Soc Rev.* 2009;38(9):2520–31. doi:10.1039/B813846J
- 430 Suppes GM, Deore BA, Freund MS. Porous conducting polymer/heteropolyoxometalate hybrid material for electrochemical supercapacitor applications. *Langmuir.* 2008;24(3):1064–9. doi:10.1021/la702837j
- 431 Vannathan AA, Maity S, Kella T, Shee D, Das PP, Mal SS. In situ vanadophosphomolybdate impregnated into conducting polypyrrole for supercapacitor. *Electrochim Acta.* 2020;364:137286. doi:10.1016/j.electacta.2020.137286
- 432 Cuentas-Gallegos AK, Martínez-Rosales R, Baibarac M, Gómez-Romero P, Rincón ME. Electrochemical supercapacitors based on novel hybrid materials made of carbon nanotubes and polyoxometalates. *Electrochem Commun.* 2007;9(8):2088–92. doi:10.1016/j.elecom.2007.06.003
- 433 Skunik M, Chojak M, Rutkowska IA, Kulesza PJ. Improved capacitance characteristics during electrochemical charging of carbon nanotubes modified with polyoxometallate monolayers. *Electrochim Acta.* 2008;53(11):3862–9. doi:10.1016/j.electacta.2007.11.049
- 434 Ruiz V, Suárez-Guevara J, Gomez-Romero P. Hybrid electrodes based on polyoxometalate–carbon materials for electrochemical supercapacitors. *Electrochem Commun.* 2012;24:35–8. doi:10.1016/j.elecom.2012.08.003
- 435 Suárez-Guevara J, Ruiz V, Gomez-Romero P. Hybrid energy storage: high voltage aqueous supercapacitors based on activated carbon–phosphotungstate hybrid materials. *J Mater Chem A.* 2014;2(4):1014–21. doi:10.1039/C3TA14455K
- 436 Mu A, Li J, Chen W, Sang X, Su Z, Wang E. The composite material based on Dawson-type polyoxometalate and activated carbon as the supercapacitor electrode. *Inorg Chem Commun.* 2015;55:149–52. doi:10.1016/j.inoche.2015.03.032
- 437 Genovese M, Lian K. Polyoxometalate modified pine cone biochar carbon for supercapacitor electrodes. *J Mater Chem A.* 2017;5(8):3939–47. doi:10.1039/C6TA10382K
- 438 Maity S, Vannathan AA, Kella T, Shee D, Das PP, Mal SS. Electrochemical performance of activated carbon-supported vanadomolybdates electrodes for energy conversion. *Ceram Int.* 2021;47(19):27132–41. doi:10.1016/j.ceramint.2021.06.128
- 439 Dubal DP, Nagar B, Suarez-Guevara J, Tonti D, Enciso E, Palomino P, et al. Ultrahigh energy density supercapacitors through a double hybrid strategy. *Mater Today Energy.* 2017;5:58–65. doi:10.1016/j.mtener.2017.05.001

- 440 Suárez-Guevara J, Ruiz V, Gómez-Romero P. Stable graphene–polyoxometalate nanomaterials for application in hybrid supercapacitors. *Phys Chem Chem Phys*. 2014;16(38):20411–4. doi:10.1039/C4CP03321C
- 441 Qin J, Zhou F, Xiao H, Ren R, Wu Z-S. Mesoporous polypyrrole-based graphene nanosheets anchoring redox polyoxometalate for all-solid-state micro-supercapacitors with enhanced volumetric capacitance. *Sci China Mater*. 2018;61(2):233–42. doi:10.1007/s40843-017-9132-8
- 442 Maity S, Das PP, Mal SS. Decavanadate-graphene oxide nanocomposite as an electrode material for electrochemical capacitor. *Mater Technol*. 2022;37:1129–39. doi:10.1080/10667857.2021.1924439
- 443 Maity S, Vannathan AA, Kumar K, Das PP, Mal SS. Enhanced power density of graphene oxide–phosphotetradecavanadate nanohybrid for supercapacitor electrode. *J Mater Eng Perform*. 2021;30:1371–7. doi:10.1007/s11665-020-05349-w
- 444 Kumari S, Maity S, Vannathan AA, Shee D, Das PP, Mal SS. Improved electrochemical performance of graphene oxide supported vanadomanganate (IV) nanohybrid electrode material for supercapacitors. *Ceram Int*. 2020;46:3028–35. doi:10.1016/j.ceramint.2019.10.002
- 445 Maity S, Vannathan AA, Chandewar PR, Shee D, Das PP, Mal SS. Vanadomanganate as a synergistic component in high-performance symmetric supercapacitor. *J Alloys Compd*. 2022;899:163239. doi:10.1016/j.jallcom.2021.163239
- 446 Maity S, JE M, Biradar BR, Chandewar PR, Shee D, Das PP, et al. Polyoxomolybdate–polypyrrole–graphene oxide nanohybrid electrode for high-power symmetric supercapacitors. *Energy Fuels*. 2021;35(22):18824–32. doi:10.1021/acs.energyfuels.1c03300
- 447 Zhang B-Y, Wu X-S, Wang N-H, Wang X-L, Han X-Q, Su Z-M. Polyoxometalates-based metal-organic frameworks with conjugated acid-base pairs for proton supercapacitors. *Chem Eng J*. 2024;500:157502. doi:10.1016/j.cej.2024.157502
- 448 Cui L, Wang M, Yu K, Lv J, Zheng X, Zhou B. The phosphomolybdate hybrids based on nanoscale heteropoly blue and metal-organic chain for supercapacitor and dual-functional electrochemical biosensor. *J Energy Storage*. 2023;60:106592. doi:10.1016/j.est.2022.106592
- 449 Li T, He P, Dong Y-N, Chen W, Wang T, Gong J, et al. Polyoxometalate-based metal-organic framework/polypyrrole composites toward enhanced supercapacitor performance. *Eur J Inorg Chem*. 2021;2021(21):2063–9. doi:10.1002/ejic.202100202
- 450 Pakulski D, Gorczyński A, Brykczyńska D, Montes-García V, Czepa W, et al. New Anderson-based polyoxometalate covalent organic frameworks as electrodes for energy storage boosted through keto-enol tautomerization. *Angew Chem Int Ed Engl*. 2023;62(32):e202305239. doi:10.1002/anie.202305239
- 451 Zhang L, Jiang H, Wang C, Yu K, Lv J, Wang C, et al. Improved supercapacitors and water splitting performances of Anderson-type manganese(III)-polyoxomolybdate through assembly with Zn-MOF in a host–guest structure. *J Colloid Interface Sci*. 2024;654:1393–404. doi:10.1016/j.jcis.2023.10.136
- 452 Chen H-Y, Wee G, Al-Oweini R, Friedl J, Tan KS, Wang Y, et al. Polyoxovanadate as an advanced electrode material for supercapacitors. *ChemPhysChem*. 2014;15(10):2162–9. doi:10.1002/cphc.201400091
- 453 Hu C, Zhao E, Nitta N, Magasinski A, Bardichevsky G, Yushin G. Aqueous solutions of acidic ionic liquids for enhanced stability of polyoxometalate-carbon supercapacitor electrodes. *J Power Sources*. 2016;326:569–74. doi:10.1016/j.jpowsour.2016.04.036
- 454 Dubal DP, Chodankar NR, Vinu A, Kim D-H, Gomez-Romero P. Asymmetric supercapacitors based on reduced graphene oxide with different polyoxometalates as positive and negative electrodes. *ChemSusChem*. 2017;10(13):2742–50. doi:10.1002/cssc.201700792
- 455 Maity S, Neethu B, Kella T, Shee D, Das PP, Mal SS. Activated carbon-supported vanado-nickelate (IV) based hybrid materials for energy application. *J Energy Storage*. 2021;40:102727. doi:10.1016/j.est.2021.102727

View Article Online  
DOI: 10.1039/D5EN00964B

### Data availability

Data sharing does not apply to this article as no datasets were generated or analyzed during the current study.

1  
2  
3  
4  
5  
6  
7  
8  
9  
10  
11  
12  
13  
14  
15  
16  
17  
18  
19  
20  
21  
22  
23  
24  
25  
26  
27  
28  
29  
30  
31  
32  
33  
34  
35  
36  
37  
38  
39  
40  
41  
42  
43  
44  
45  
46  
47  
48  
49  
50  
51  
52  
53  
54  
55  
56  
57  
58  
59  
60

Open Access Article. Published on 02 February 2026. Downloaded on 24/02/2026 22:48:59.  
This article is licensed under a Creative Commons Attribution 3.0 Unported Licence.

